2009-01-01

Magnitude Of Right-Lateral Offset On The Southern Death Valley Fault Zone From Miocene Volcanic Assemblages

Sabrina Michelle Canalda
University of Texas at El Paso, smcanalda@miners.utep.edu

MAGNITUDE OF RIGHT-LATERAL OFFSET
ON THE SOUTHERN DEATH VALLEY
FAULT ZONE FROM MIOCENE
VOLCANIC ASSEMBLAGES

SABRINA MICHELLE CANALDA

Department of Geological Sciences

APPROVED:

_____
Terry L. Pavlis, Ph.D., Chair

_____
Richard P. Langford, Ph.D.

_____
Josiah Heyman, Ph.D.

_____
Patricia D. Witherspoon, Ph.D.
Dean of the Graduate School

This thesis is dedicated to my family and friends who have provided constant support and encouragement during my graduate studies in geology at the University of Texas at El Paso. Without these special people, I would have had a difficult time completing my research and school work.

MAGNITUDE OF RIGHT-LATERAL OFFSET ON THE SOUTHERN DEATH VALLEY FAULT ZONE FROM MIOCENE VOLCANIC ASSEMBLAGES

By

SABRINA MICHELLE CANALDA, BS

THESIS

Presented to the Faculty of the Graduate School of

The University of Texas at El Paso

In Partial Fulfillment

of the Requirements

for the Degree of

Master of Science

Department of Geological Sciences

THE UNIVERSITY OF TEXAS EL PASO

May 2009

ACKNOWLEDGEMENTS

I am very grateful for all the knowledge and friendship I gained while studying under Dr. Pavlis (a.k.a. Daddy Terry). I have the most respect and admiration for him. Dr. Pavlis and Dr. Serpa introduced me to the most beautiful place to do research, Death Valley. I am honored to have had their great company and shared knowledge, while I completed my studies. I also like to acknowledge Dr. Velasco, Dr. Langford, and Tina Carrick for all their support and advice throughout my academic career, which assisted me in achieving my goals. Special thanks goes to Dr. Lemone, Dr. Cornell, Dr. Hurtado, Dr. Ellis, Dr. Andronicos, Dr. Anthony, and Dr. Goodell. These professors have given me a lot of geologic knowledge, and prepared me for a future in geology. Without all these people mentioned above I would not be where I am today.

Mingua Ren gave me constant assistance on my thesis and without him I wouldn't have completed it. Vanessa Espejel also helped out with my geochemical data and was a good friend to me during my time at U.T.E.P. Many thanks to Pam Hart, Sandra Lewig, Carlos Montana, and Joel Gilbert, without the great staff and faculty in the department I would have had a difficult time. They are Pam Hart, Sandra Lewig, Carlos Montana, and Joel Gilbert. There are several other colleagues of mine, that without them I wouldn't have had such a positive college experience. They are Keith Cardon, Alvaro Fernandez, Erik Day, Hugo Rodriguez, Sarah Cervera, Anthony Munika, Chris Benker, Katrina Pekar, Dan Miggins, Oscar Romero, Cecilia del Prado, John Olguin, Roberto Torres, Frank Guerrero, Lennox Thompson, and Ezer Patlan.

Lastly, but not least I like to acknowledge my family for their constant love and encouragement, during my college days. My son Noah has motivated me to achieve my academic goals and further my education. I love all of my family deeply and know they are the reason for my success.

ABSTRACT

In this study correlation of Miocene volcanic and sedimentary rocks in southern Death Valley is used to constrain the total amount of slip on the southern Death Valley fault. The tertiary volcanic section near Ibex Pass is correlated to rocks ~35 km to the northwest, in the Wingate Wash region (Luckow et al., 2005). Geochronology by Luckow et al. (2005) in Wingate Wash and the Owlshead Mountains has the region divided into two basic periods: an early interval (~14-13.4Ma), and a later phase (~13-12.5Ma). One date from the volcanic sequence in Ibex Pass has been reported (Calzia, 2000) suggesting that rocks of this section is a time equivalent to the Wingate Wash section. However, Topping (1993) suggested this section contains the ~10 Ma Rhodes tuff, and is therefore is at least partially distinctly younger than the Wingate Wash section. Geochemical analyses and geologic mapping of lithologic units in Ibex Pass was performed to determine the structure and magmatic history of the area. Results from the correlation of physical stratigraphy and elemental chemistry on volcanics in southern Death Valley, suggests a geologic association between Wingate Wash and Ibex Pass. Data provided on the Pre-Shoshone volcanics containing the Rhodes Tuff was determined to have no stratigraphic or geochemical connection to the Ibex Pass volcanics. The data on the rock units in Ibex Pass clarifies the age discrepancy given for this region as well. The research conducted provides a better understanding on the displacement that has occurred in the southern Death Valley right-lateral strike slip system. The correlation of volcanic and sedimentary rocks along the southern Death Valley fault zone demonstrates there is at least ~25km of slip and as much as ~35km of slip that has occurred along the fault zone in the last 12Ma. A reconstruction model created for this study displays the suggested amounts of offset.

TABLE OF CONTENTS

Page

ACKNOWLEDGEMENTS.....iv

ABSTRACT.....v

TABLE OF CONTENTS.....vi

LIST OF FIGURES.....viii

1. INTRODUCTION.....1

2.REGIONAL GEOLOGY.....5

2.1 Southern Death Valley Fault Zone.....8

3. LOCAL GEOLOGY.....10

3.1 Igneous Rocks of the Death Valley Region.....11

3.1.1 Central Death Valley Volcanic Field.....11

3.1.2 Wingate Wash.....13

3.1.3 Sperry Hills.....14

4. METHODS.....20

4.1 Outcrop Methods.....20

4.2 Petrographic Methods.....22

4.3 Electron microprobe Methods.....22

4.4 Whole Rock Chemistry.....24

5. RESULTS.....26

5.1 Ibex Pass Stratigraphy 26

5.2 Ibex Pass Structure.....30

5.3 Microprobe Analyses……...……...42

5.4 Whole Rock Analyses……...…….……53

5.4.1 TAS Classification..…...……...……...……...……53

5.4.2 Harker/Variation Diagrams...……53

5.4.3 Spider Diagram..……...……56

5.4.4 Rare Earth Element Diagram……...…….56

6. DISCUSSION..…...……...……68

6.1 Comparing Geochemistry…….....……...68

6.2 Comparing Physical Stratigraphy…….……..……..70

7. CONCLUSIONS...……...……86

REFERENCES..…..……88

APPENDIX A. Thin sections..……..……93

APPENDIX B. Microprobe data……121

APPENDIX C. INAA Normalization Factors...……138

APPENDIX D. ICPMS Analyses for units in Ibex Pass...……139

APPENDIX E. XRF analyses for units in Ibex Pass.....……140

CURRICULUM VITA...……...……143

LIST OF FIGURES

Figure 1: The southern Death Valley Fault (Luckow, 2005)…….…….…….3

Figure 2: Location Map (World Wind)…….…….……..4

Figure 3: Geologic Provinces…….……..……....6

Figure 4: Cenozoic volcanism locations….……..……7

Figure 5: Stratigraphic column of Tertiary volcanics for the Furnace Creek Formation…….……..16

Figure 6: Stratigraphic column of east-central volcanics…….…….……17

Figure 7: Wingate Wash/Owlshead Mountains Geologic Map…….…….……...18

Figure 8: Wingate Wash stratigraphic column…….…….……18

Figure 9: Stratigraphic column of Sperry Hills volcanics…….…….……...19

Figure 10: Location Map of where geologic mapping was produced…….…..…….21

Figure 11a) Photograph of tuff unit in Wingate Wash…….…….……23

Figure 11b) Photograph of tuff unit in Ibex Pass.…….…….……23

Figure 12a) Location map of sample locations for whole rock analyses in Ibex Pass..……32

Figure 12b) Ibex Pass Geologic Map…….……..……..33

Figure 13: Ibex Pass Cross Section……. …….……34

Figure 14: Ibex Pass Stratigraphic column…...….…….……..34

Figure 15a) Photograph of Ibex Pass volcanic field…….…….……35

Figure 15b) Photograph of dacite unit (D) in Ibex Pass …….……..35

Figure 15c) Photograph of intrusive trachyte in the volcanic section ……..36

Figure 15d) Photograph of pyroclastic assemblage (TA) in Ibex Pass …….……36

Figure 15e) Photograph of purple flow with clasts of andesite in Ibex Pass …….……...37

Figure 15f) Photograph of purple-gray flow with clasts of basalt in Ibex Pass ……..…...37

Figure 15g) Photograph of trachyte (T) unit in Ibex Pass ……38

Figure 15h) Photograph of tan to white tuff unit in Ibex Pass …….…….38

Figure 15i) Photograph of megabreccia with clast of granite in Ibex Pass ……..39

Figure 15 j) Photograph of rhyolite dike(R1) in Ibex Pass …….…….39

Figure 15k) Photograph of vitric rhyolite (R2) in Ibex Pass …….……..40

Figure 15l) Photograph of rhyolitic intrusion (R3) in Ibex Pass ……..40

Figure 15m) Photograph of slickenslides on fault surface in Ibex Pass …….……..41

Figure 15n) Photograph of distint normal fault in Ibex Pass …….……...41

Figure 16a) DV60/Ibex Pass Feldspar Ternary Diagram …….……45

Figure 16b) DV74/Ibex Pass Feldspar Ternary Diagram …….……45

Figure 16c) DV79/Ibex Pass Feldspar Ternary Diagram ……46

Figure 16d) DV93/Ibex Pass Feldspar Ternary Diagram …….……46

Figure 16e) DV2000B/Wingate Wash Feldspar Ternary Diagram …….……47

Figure 16f) DV2000A/Wingate Wash Feldspar Ternary Diagram …….……..47

Figure 16g) Ibex Pass and Wingate Wash Feldspars Ternary Diagram …….……..48

Figure 17a) DV60/Ibex Pass Pyroxene Ternary Diagram …….……...49

Figure 17b) DV74/Ibex Pass Pyroxene Ternary Diagram …….……...49

Figure 17c) DV79/Ibex Pass Pyroxene Ternary Diagram …….……...50

Figure 17d) DV93/Ibex Pass Pyroxene Ternary Diagram …….……...50

Figure 17e) DV2000B/Wingate Wash Pyroxene Ternary Diagram …….……51

Figure 17f) DV2000A/Wingate Wash Pyroxene Ternary Diagram …….……51

Figure 17g) Ibex Pass and Wingate Wash Pyroxenes Ternary Diagram…….……..52

Figure 18: TAS Diagram for Ibex Pass……..……55

Figure 19: Alkaline vs. subalkaline diagram for Ibex Pass…….……..57

Figure 20: High, medium, and low-K fields for Ibex Pass…….……...58

Figure 21: Major elements for units in Ibex Pass vs. silica…….……..59

Figure 22: Minor and minor elements for units in Ibex Pass vs. silica……..……60

Figure 23: Trace elements for units in Ibex Pass in Ibex Pass vs. silica……..……..61

Figure 24: Trace elements for units in Ibex Pass in Ibex Pass vs. silica……..……..62

Figure 25a) Spider Diagram for Trachyandesite units in Ibex Pass…….……63

Figure 25b) Spider Diagram for Trachyte units in Ibex Pass…….……...64

Figure 25c) Spider Diagram for Rhyolite/Dacite units in Ibex Pass…….65

Figure 25d) Spider Diagrams for all volcanic units in Ibex Pass…….…….66

Figure 26: Rare Earth Element Diagram for volcanic units in Ibex Pass…….…….67

Figure 27: TAS Diagram for volcanic units in Southern Death Valley…….……72

Figure 28: Alkaline vs. subalkaline diagram for volcanic units in Southern Death Valley…….73

Figure 29: High, medium, and low-K fields for volcanic units in Southern Death Valley…….74

Figure 30: Major elements for volcanic units in Southern Death Valley vs. silica…….....…..75

Figure 31: Major and minor elements for volcanic units in Southern Death Valley…….76

Figure 32: Trace elements for volcanic units in Southern Death Valley vs. silica…….…...77

Figure 33: Trace elements for volcanic units in Southern Death Valley vs. silica…….…...78

Figure 34a) Geochemical plot of MgO vs. K_2O for volcanic units in Southern Death Valley…….79

Figure 34b) Geochemical plot of Mg# vs. TiO_2 for volcanic units in Southern Death Valley……...……..…79

Figure 35a) Spider Diagram for trachyandesite units in Southern Death Valley and Big Bend volcanics…….……...80

Figure 35b) Spider Diagram for trachyte units in Southern Death Valley, Big Bend, Pantellaria, and Suswa volcanics…….....81

Figure 35c) Spider Diagram for rhyolite/dacite units in Southern Death Valley and Big Bend volcanics…….....82

Figure 36a) REE Diagram for trachyandesite units in Southern Death Valley and Big Bend volcanics…….....83

Figure 36b) REE Diagram for trachyte units in Southern Death Valley, Big Bend, Pantellaria, and Suswa volcanics……..84

Figure 36c) REE Diagram for rhyolite/dacite units in Southern Death Valley and Big Bend volcanics…….....85

Figure 37) Reconstruction model of the Southern Death Valley Fault System……..…87

1. INTRODUCTION

The Death Valley region (Figure 1) is formed due to extension and strike slip movement created along a complex system of faults (Stewart, 1983). The southern Death Valley fault system (Figure 2) is a northwest-trending, right-lateral, strike-slip system of faults (Butler, 1989). Most of the slip on the southern Death Valley fault took place before one million years ago, and after that time has been characterized by oblique slip with a lateral movement of a few hundred meters along the eastern part of the fault system (Butler,1988). There are several other parallel fault systems in the region that display a similar strike-slip component. The southern end of the southern Death Valley fault zones intersects the left lateral Garlock fault. What takes place at the intersection between the two strike-slip zones has been significantly debated. In addition for several decades there has been a debate concerning the amount of slip on the southern Death Valley fault system.

The conflict on displacement of the southern Death Valley fault arose when Stewart (1967) proposed there was ~80 km of offset on the fault system and Wright and Troxel (1967) thought the displacement was ~8 km. Research done by (Hamilton and Myers, 1966, Plescia and Henyey, 1982, Butler et al., 1988) all have developed their own conclusions on the amount of offset. All estimations have been determined from different piercing points. Matching of a "point source" with a point deposit" offers a good constraint on direction and magnitude of tectonic transport of the deposit from its source locale (Topping, 1993).

Recent work conducted (e.g. Luckow et al.,2005 and Guest et al., 2003) to the southwest of Death Valley in Wingate Wash recognized a distinctive volcanic assemblage and associated overlying sedimentary deposit. This lithologic package is a potential recognizable piercing point marker to correlate with rocks across the Death Valley fault system. In this study, I investigate

this hypothesis by examining potential correlative volcanic assemblages in the Ibex Pass region, located in southern Death Valley. The correlation between lithologic units in the Wingate Wash region and the Ibex Pass area suggest 25-35 km of right-lateral slip.

To evaluate this correlation I begin with a description of the local geology of the Ibex Pass from five weeks of geologic mapping. This mapping reveals a distinct similarity of volcanic units in Ibex Pass with the lower part of the Wingate Wash section. Geochemical data were obtained from a suite of samples from Ibex Pass to compare with geochemical studies of the Wingate Wash section by Yawn (1995) and Luckow et al. (2005). Geochemical data from a volcanic sequence containing the Rhodes tuff are then compared with Ibex Pass to further assist in acquiring an answer to the proposed geologic problem.

In determining if the rock units from Wingate Wash and Ibex Pass are correlative I use physical stratigraphy and geochemical characteristics using major, minor, and trace elemental chemistry. Total alkali vs. silica diagrams, Harker diagrams, variation diagrams, spider diagrams, and rare earth element diagrams all are examined to distinguish if lithologic units are geochemically similar to one another. Microprobe analyses performed on tuffaceous units from Ibex Pass and Wingate Wash are also used to evaluate correlation between tuff units.

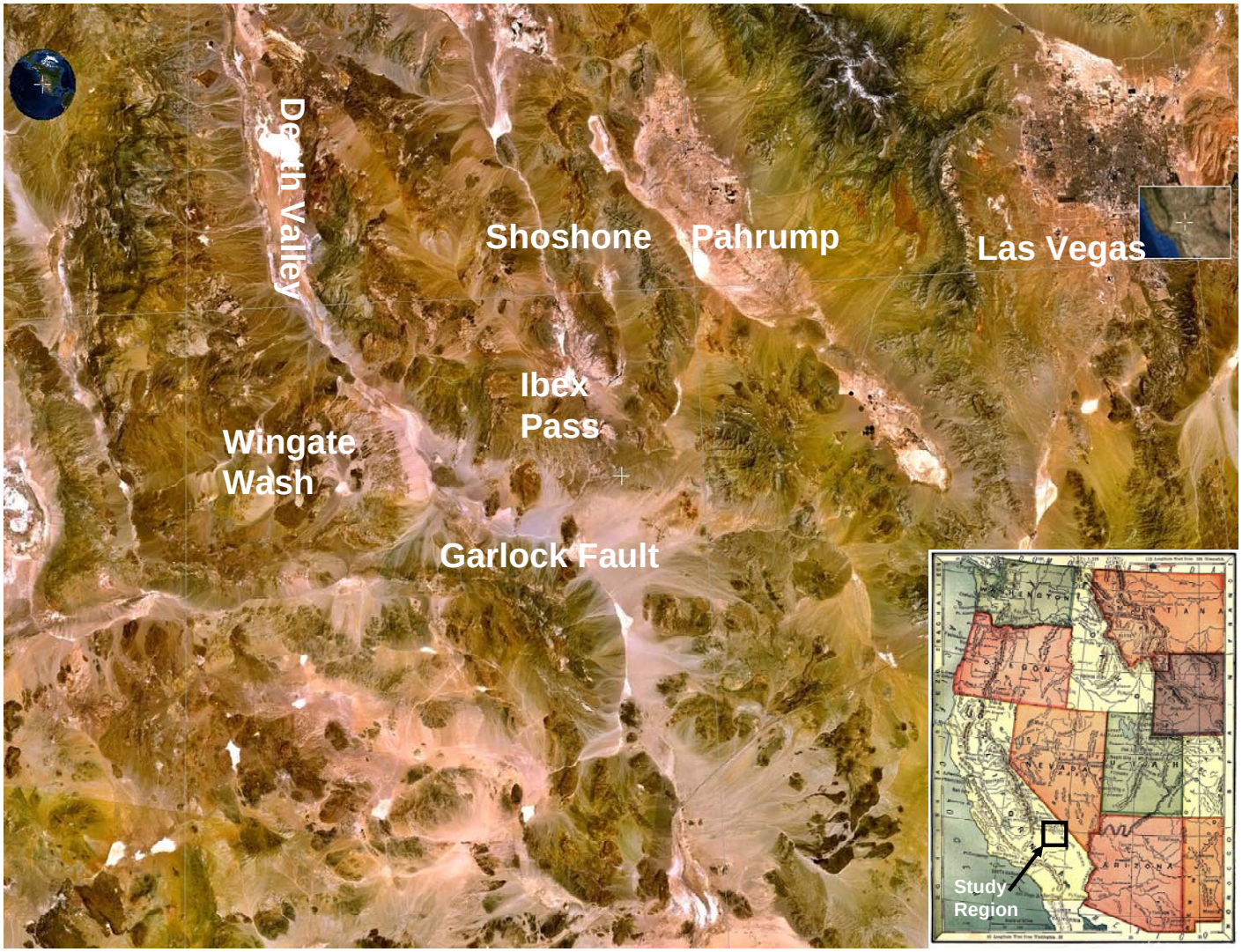

Figure 1. NASA World Wind Satellite Composite image of the Death Valley region.

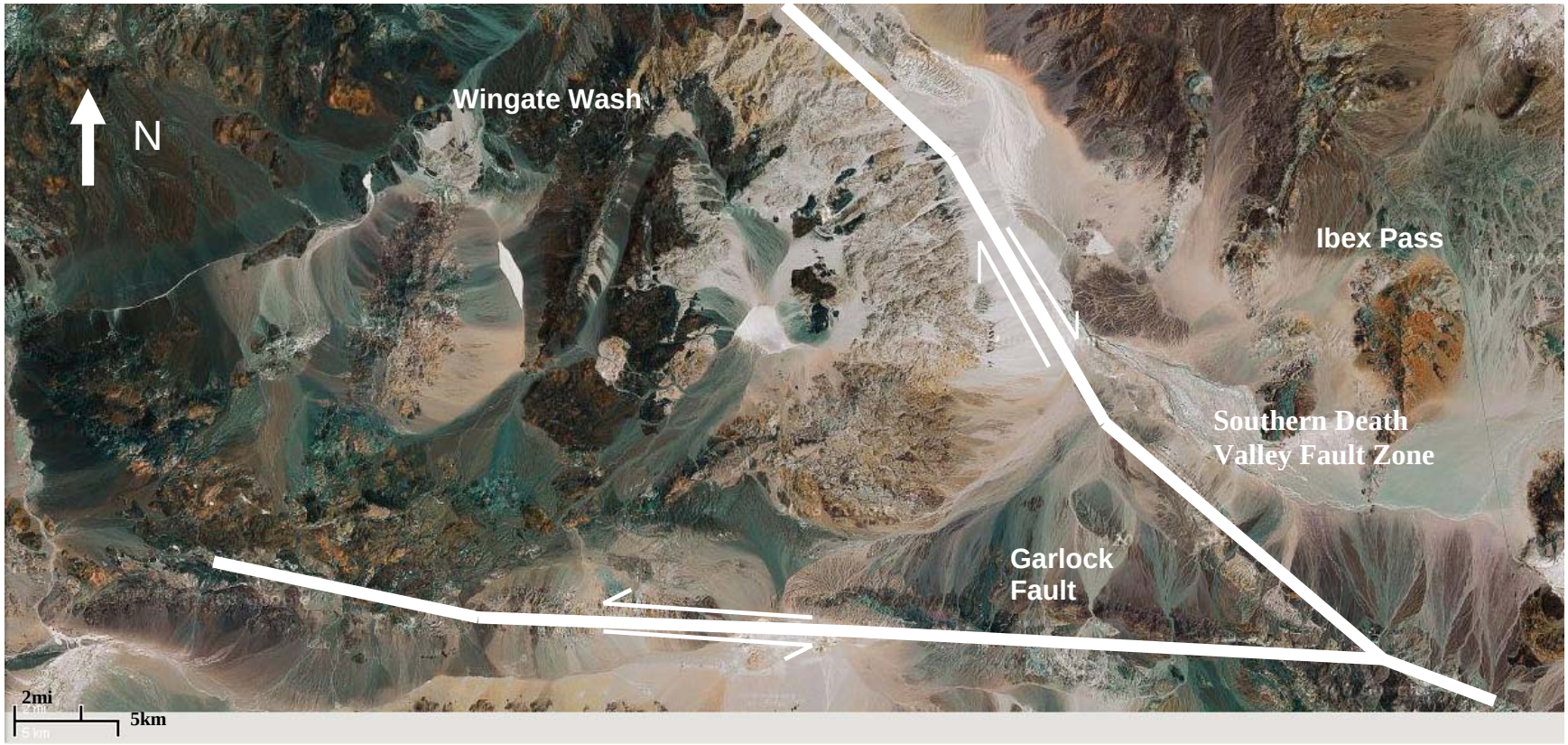

Figure 2. Satellite image from Google Map of southern Death Valley showing major faults and the location of the Ibex Pass study area relative to the Wingate Wash area.

2. REGIONAL GEOLOGY

The Mojave Desert region of southern California is bounded by the Basin and Range and the Sierra Nevada provinces (Figure 3). The Mojave Desert holds information on different developmental phases of the Cordilleran orogen which include (1) Rifting occurring in the Neoproterozoic and Paleozoic passive-margin development; (2) Mesozoic arc magmatism and deformation due to subduction; (3) mid-Tertiary volcanism and simultaneously extension; and (4) transpression and dextral shear that is caused by the Pacific-North American plate boundary (Glazner et al., 2002a).

Southwestern North America was a convergent margin from Mesozoic to Paleogene, but this margin became an extensional regiment from 28 Ma to 14Ma migrating from the southwest to northwest (McQuarrie and Wernicke, 2005). As extension proceeded the upper part of the earth's crust ruptured and the Sierra Nevada block moved westward away from the west side of the Colorado Plateau (Miller and Wright, 2004). Extension and volcanism are believed to have begun as a result of the northwest foundering of the Farallon Plate, but dextral shear became increasingly important as the San Andreas system evolved along the margin. (e.g. McQuarrie and Wernicke, 2005).

The Oligocene-Miocene boundary at ca. 24-22 Ma had a return of magmatism to the Mojave block, where volcanic rocks were erupted along an east-trending belt that went from the westernmost Mojave desert region inland to the Whipple Mountains and beyond (Glazner et al. 2002b). Volcanic rocks predominantly 20-14 Ma are found north of Barstow, along with scattered outcrops of late Miocene and younger basalts. These rocks are mainly calc-alkalic and range in composition from basalt to rhyolite. (Glazner et al., 2002b). Late Cenozoic magmatism

has been linked to the last phase of Basin and Range extension (Yawn, 1995). (Figure 4) shows the volcanism that occurred in the western United States ~12.6 Ma.

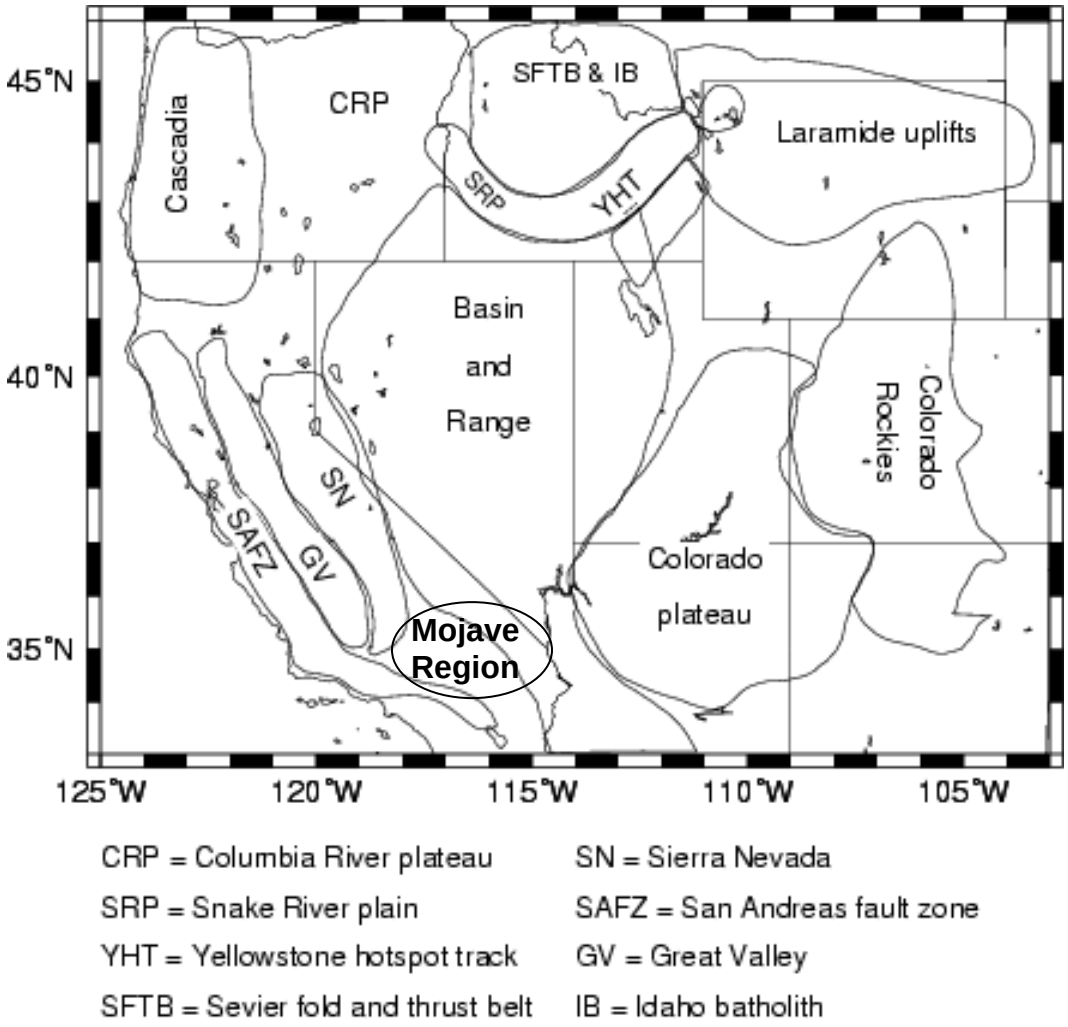

Figure 3. Physiographic provinces of the western U.S.
Modifed from http://www.geology.wisc.edu/courses/g112/mtns_westernUS.html.

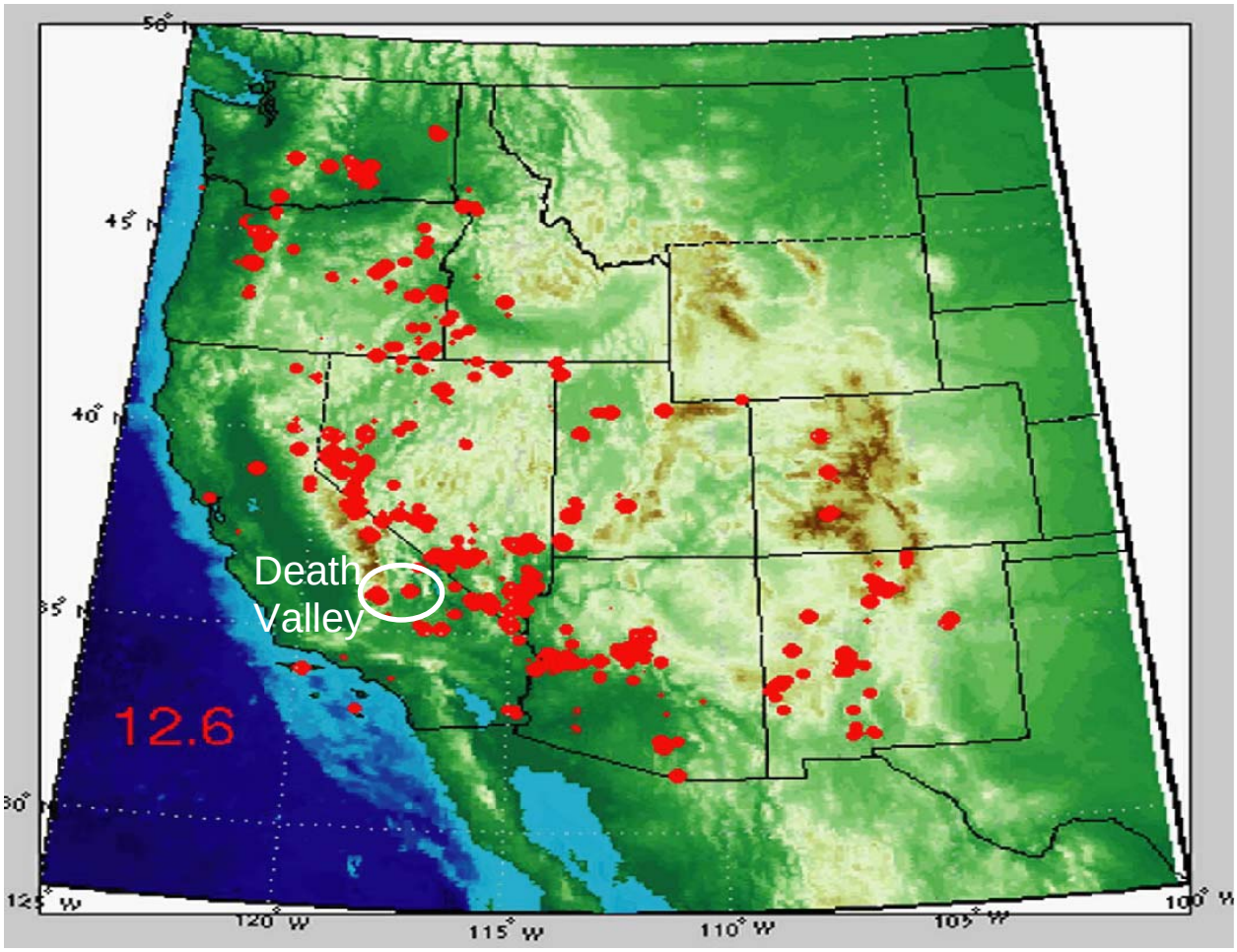

Figure 4. Cenozoic volcanism locations in the western United States. Modified from navdat.geongrid.org.

2.1 Southern Death Valley Fault Zone

There has been right-lateral strike-slip movement, with a minimum displacement in kilometers, that has occurred along the southern and northern Death Valley fault zones (Wright and Troxel, 1970). It has been suggested that the slip sense along the southern Death Valley fault zone is related to the translation of the Owlshead Mountain block relative to the Black Mountain block and the northwest translation of the Panamint block, which together contributes to the right lateral offset of the Furnace Creek fault zone (Serpa et al., 1988).

The confusion on the displacement of the Southern Death Valley Fault is due to interpretations in the past that the southern Death Valley fault zone and the northern Death Valley-Furnace Creek fault zone were connected, and that the offsets should be similar (Stewart, 1983). Stewart (1983) proposed that the two fault zones are related but not connected, and that 80 km of transport based on offset of sedimentary trends along the Furnace Creek fault zone can be extended to the southern Death Valley fault. An opposing view with only 8 km of displacement was suggested by (Wright and Troxel, 1967) based on continuity of Precambrian stratigraphic trends across the southern Death Valley region. The same isopach data was recontoured to give an estimated 50 km of right-lateral movement (Hamilton and Myers, 1966). By matching offset on alluvial fan gravel with its source area, 35 km of offset has been estimated, and that amount of displacement is consistent with the geometry of a pull-apart basin model for central Death Valley (Butler, 1988).

More recently, studies have emphasized the role of transrotation in the Eastern California Shear Zone to resolve the slip problem (Dokka and Travis, 1990; Serpa and Pavlis, 1996; Snow and Wernicke, 2000; Guest et al. 2003). The Eastern California Shear Zone is a system of mostly right-lateral, strike-slip faults and normal faults that accommodates ~20-25% of the total

relative motion between the Pacific and North American plates (Frankel et al., 2007).. When trying to determine the amount of offset on the Eastern California Shear Zone, the ~35 of right-slip on the Southern Death Valley fault zone has been shown to represent the main part of the total dextral offset on the Eastern California Shear Zone (Gan et al., 2003). A three dimensional model of the southern Death Valley fault system suggests the basin began as a pull- apart basin between the Garlock and Furnace Creek faults, and developed into a system that is characterized by distributed transtension and transrotation that is in association with the eastern California shear zone (Serpa and Pavlis, 1996; Guest et al., 2003). Estimates of crustal extension in the southern Death Valley region range from 30-50% (Wright and Troxel, 1973) to >100% (Wernicke, 1988). Lower amounts of extension would account for the ~35 km of offset, and if extension occurred at a range of >100 the offset amount would not be feasible. Models of the reconstruction of the Death Valley region can therefore provide useful information in confirming or denying ~35km of displacement on the southern Death Valley fault zone.

3. LOCAL GEOLOGY

Death Valley is a structural depression that lies to the east of the Panamint Range and to the west of the Black and Funeral Mountains, and is located in the southwestern part of the Basin and Range province (Hill and Troxel, 1966). The Plio-Pleistocene central Death Valley region, a pull-apart basin, has formed because of oblique extension between the en echelon southern Death Valley and northern Death Valley-Furnace Creek strike-slip fault zone (Burchfiel and Stewart, 1966, Wright et al., 1974, Stewart, 1983; de Voogd et al., 1986). The west-dipping normal fault system in the western slope of the Black Mountains distributes motion between the two dextral strike-slip faults (Burchfiel and Stewart, 1966). The active Death Valley fault system consists of three parts: the dextral Northern Death Valley fault zone (NDVFZ), the oblique extensional Black Mountains fault zone (BMF), and the dextral Southern Death Valley fault zone (SDVFZ) (Machette et al., 2001; Miller and Wright, 2004). The combined length of the Death Valley and Death Valley-Furnace Creek fault zones has been estimated to be ~320 miles (Wright and Troxel, 1967).

A first-order feature of Cenozoic extension is west-dipping normal faults that bound east tilted fault blocks (Serpa et al., 1988) The main accepted theory of the evolution of the central Death Valley basin during the last 2 to 6 Myr is the Burchfiel and Stewart (1966) 'pull-apart' model. There are various other models that demonstrate the amount of extension that Death Valley has undergone in late Cenozoic time, which varies from 30-50% extension to well over 100%. (Serpa and Pavlis, 1996).

The Garlock fault is a northeast-to-east-trending, major strike slip fault with a left-lateral displacement of at least 48 to 64 km (Davis and Burchfiel, 1973; Brady, 1986). It has been suggested that there was a proto-Garlock fault with movement in the Paleocene time (Nilsen and

Clark, 1975). The initiation of motion of the Garlock more likely is recognized to occur between 10 to 7 Ma, due to magnetostratigraphic determination on sedimentary and volcanic units offset by the fault (Monastero et al., 1997). The intersection between the Garlock fault and southern Death Valley fault has caused the eastern end of the Garlock fault to turn southward and become a thrust fault dipping westward under the Avawatz Mountains (Brady, 1986). The active interaction between the Garlock and southern Death Valley fault zone has created the Quaternary stratigraphy and structure of the Avawatz Mountains. The southern Death Valley fault system is believed to extend at least 20 km south of the Avawatz Mountains (Brady, 1986). Reconstructions for the Cenozoic structural history show that the rotation of the northeastern Mojave block could account for the amount of offset on the Garlock fault (Guest et al., 2003). A tectonic understanding of the Garlock fault assists in trying to unravel the past history and displacement of the southern Death Valley fault zone.

3.1 Igneous Rocks of the Death Valley Region

3.1.1Central Death Valley Volcanic Field

According to the stratigraphic column in Wright et al. (1991) the Central Death Valley volcanic field, which is associated with the Furnace Creek fault zone has been grouped into three distinct sedimentary formations (Figure 5) that include; 1.) The Artists Drive Formation, comprised of a lower sedimentary member which includes two tuff units, varying in age from ~13.7-12.7 Ma, and a middle and upper member that include basalt; 2.) the middle Furnace Creek Formation which includes a basalt flow of ~6Ma, and younger layered lacustrine strata comprised of intertonguing conglomerate, mudstone, sandstone, and tuff; 3.) the upper Funeral Formation comprised of conglomerate topped with a ~ 4.03 Ma basalt. The Ibex Pass volcanics are thought to be similar in age to the Artists Drive Formation, but are lithologically very

different. The ~13.7±4 Ma tuff near the base of the formation is believed to be a minimum age for the initiation of extension and movement of the fault zones (Wright et al., 1991).

There are a group of extension related 11-0.7 Ma volcanic rocks that were erupted in a volcanic field in Southern Death Valley (Figure 6). They are from oldest to youngest the 1)pre Shoshone volcanic rocks, 2)Shoshone volcanics, 3)Greenwater volcanics, 4)Funeral Formation lavas, and 5) valley basalts. The pre-Shoshone volcanics are comprised of three sequences which include the 1)Sheephead Andesite and Rhodes Tuff 2)altered volcanic rocks, and 3)flows of andesite and dacite. (Wright et al., 1991). The Rhodes Tuff, an orange-weathering tuffaceous rock, overlain by Shoshone airfall tuff has been identified in the Ibex Hills as well (Wright et al., 1991). This same rock unit has been age determined to be 9.5±0.3 Ma (Topping, 1993), and is thought to be lithologically similar to the tuff deposits in Ibex Pass. This proposed correlation has important implications for this study, and is therefore, evaluated further below. The Rhodes tuff has been described as a densely-welded, lithic-rich, rhyolite ash-flow tuff composed of biotite phenocrysts, plagioclase, and quartz in a glassy to cryptocrystalline devitrified ground mass (Wright et al., 1991). The younger Sheephead Andesite is divided into three units by Wright and Troxel (1984). The lower unit is an andesite composed of laharic breccia, flow breccia, and lava flows. The upper sequence is a thin laharic breccia topped with a massive andesitic flow. The Sheephead andesite is enriched in rare earth elements (REE), LIL, and HFSE compared to younger andesites that contain the same amount of SiO2 (Wright et al., 19991). The Shoshone volcanics are grouped as intermediate to silic rocks that were erupted during ~8.5-7.5. Basal tuffs, tuffaceous sediments and mixed rhyolite vitrophyre and pumiceous tuffs are all in this section. (Wright et al., 1991).

3.1.2 Wingate Wash

Wingate Wash (Figure 7) is a topographic low between the Panamint and Owlshead Mountains *(*Luckow, et al., 2005*).* Wingate Wash contains a middle Miocene alkaline volcanic package that varies in composition from basaltic to rhyolitic, the majority classified as trachyte, trachybasalt, trachyandesite, and trachydacite. In the Wingate Wash section there are volcanic rocks that lie directly on weathered granite with channelized layers of a conglomerate overlain by volcanic rocks along the nonconformity. On top of the unconformity is: (1) a basal unit composed of basaltic and andesitic flows with a few interbedded pyroclastic units; (2) a middle, predominately pyroclastic unit with interbedded trachyandesitic flows that begin with a white tuff layer; and (3) a top unit that is mostly basalt flows, and basaltic pyroclastics. The same white lithic tuff is identified throughout the northeastern Owlshead Mountains (Figure 8). The volcanic unit in the Owlshead Mountains is comprised of a lower section of flows interbedded with pyroclastic units, a white tuff, more flow units, and an overlying section of volcanic flows. (Luckow et al., 2005). There is a large exhumed 2-3 km wide volcanic center that is in the eastern half of the southern Panamint Mountains, which is believed to be a source for many of the volcanic assemblages in Wingate Wash. The entire volcanic package within ~2km of the intrusive center is predominantly coarse grained pyroclastic rocks, interlayered with a couple of flows, and locally interlayered with large quantities of rhyodacite. (Luckow et al., 2005).

Luckow et al (2005) has the Wingate Wash and the Owlshead Mountains region divided into at least three volcanic episodes. Based on 40Ar/39Ar ages there is the oldest southern Panamints (pre-13.65 Ma) and lower Wingate Wash section at 13.94-13.56 Ma. This is followed by the Eastern Owlshead at 13.4-13.26 Ma, and ends with the north-central Owlshead and upper Wingate Wash section at 12.79-12.56 Ma. Geochemical data from the Eastern Owlshead and

lower Wingate Wash section will be compared with the Ibex region due to similar geochemistry and stratigraphic relationships. The volcanic rocks in the Eastern Owlshead Mountains have elevated silica and total alkalis. They range in composition from mostly rhyolites to trachytes and trachyandesite, and one foidite. In Wingate Wash and the Eastern Owlshead Mountains there are high levels of potassium and samples have the same trend on the K2O vs. MgO plot. (Luckow et al., 2005).

3.1.3 Sperry Hills

The Sperry Hills basin is a thick section of Miocene sedimentary rocks (Figure 9) that is 20 km west of the Kingston Range and 30 km southeast of the Amargosa Chaos basin section (Topping 1993). The Ibex Pass region is the western part of this basin and thus provides important background.

There is a volcanic package in the Sperry Hills basin that is similar in age and lithology that may be in correlation with the Ibex Pass volcanics. The stratigraphic column in Friedmann (1999) describes three distinct members in the volcanic assemblage. Member 1 contains a volcanic breccia ranging in age from 13.1± .2 to 13.0± .2 that is interbedded with carbonate breccia and coarse clastics. Member 2 begins with a 12.0± .2 similar volcanic breccia, found above an unconformity of ~1Ma. Overlying the volcanic breccia is randomly distributed coarse clastics and carbonate breccia. After 11.8 ± .2 there is a gravity slide block that spans in age up to 11.4± .3. Member 3 sits on top of an unconformity of ~1Ma and three packages of coarse clastics, carbonate breccia, and volcanic breccia. (Friedmann, S.J., 1999).

The upper part of Member 1 and lower section Member 2 are of the same time sequence of the Ibex Pass volcanics, and Ibex Pass also contains a volcaniclastic facies in its assemblage. However, stratigraphically there is a discordance due to the fact that the volcaniclastic facies in

the Sperry Hills in overlain by a carbonate breccia. There is a carbonate breccia that has been identified in Ibex Pass region, but depositionally it overlies the mega breccia with clasts of granite. Thus, the stratigraphic position of the megabreccias implies the volcanic rocks of the Sperry Hills are younger than the Ibex Pass section.

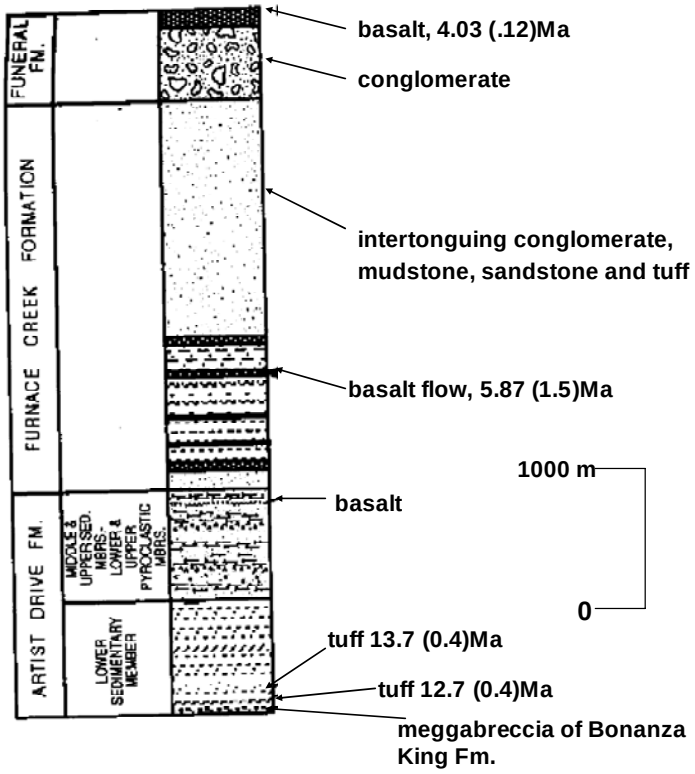

Figure 5. Stratigraphic column of Tertiary volcanics for the Furnace Creek Formation. Modified from Wright et al. (1991).

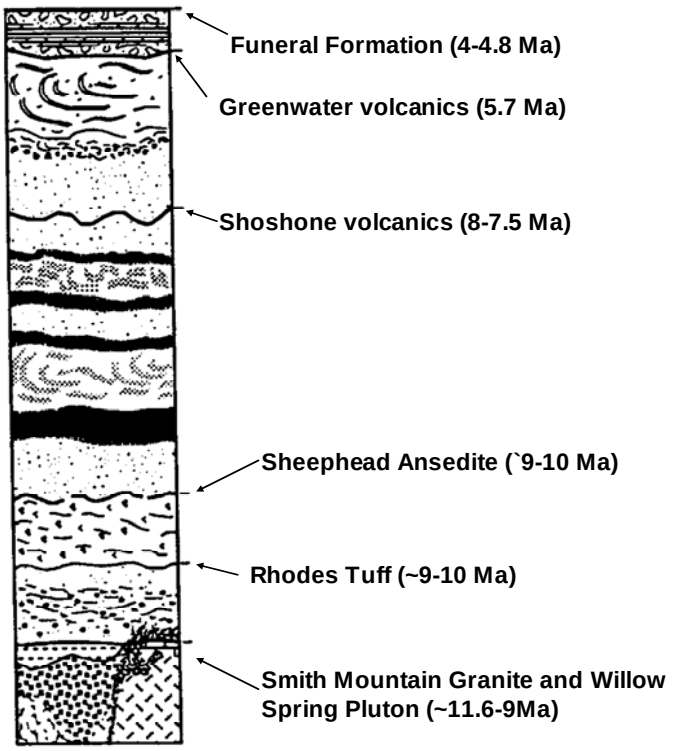

Figure 6. Stratigraphic column of east-central volcanics. Modified from Wright et al. (1991).

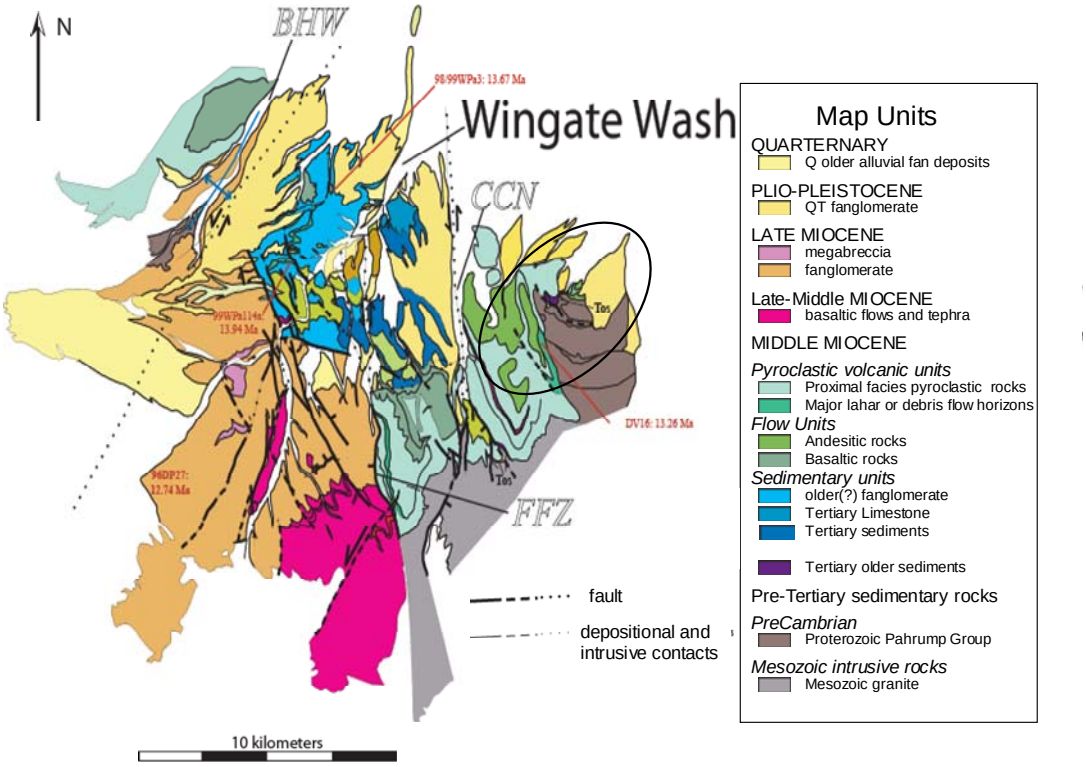

Figure 7. Geologic Map of Wingate Wash/Owlshead Mountains. Luckow et al. (2005). BHW: Burro Highway Wash, CCN: Confusion Canyon, FFZ: Filtonny Fault Zone.

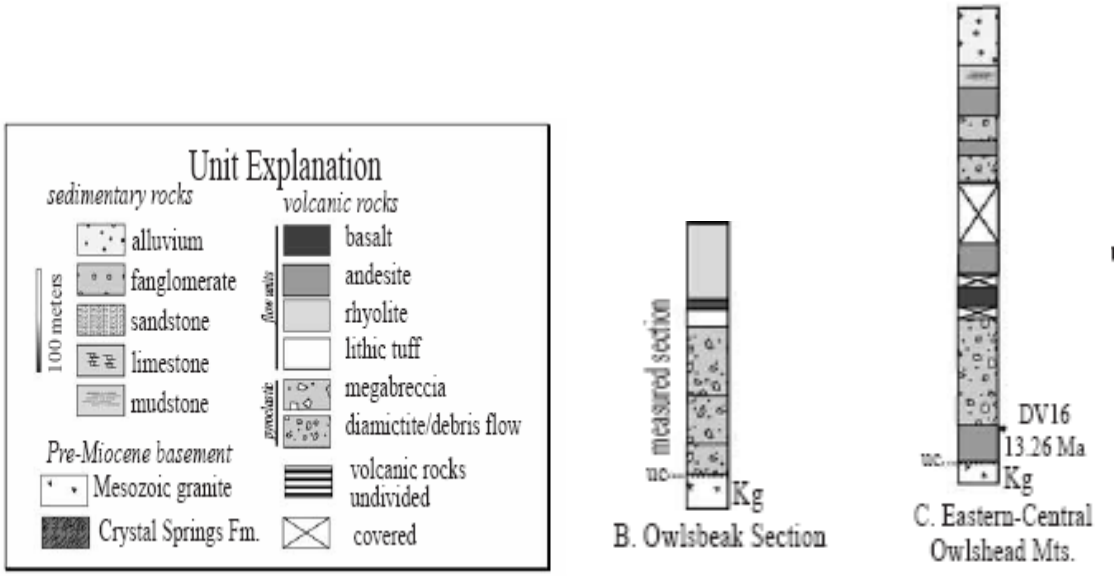

Figure 8. Stratigraphic sections of the Wingate and Owlshead Mountains. Luckow et al., 2005, p.187)

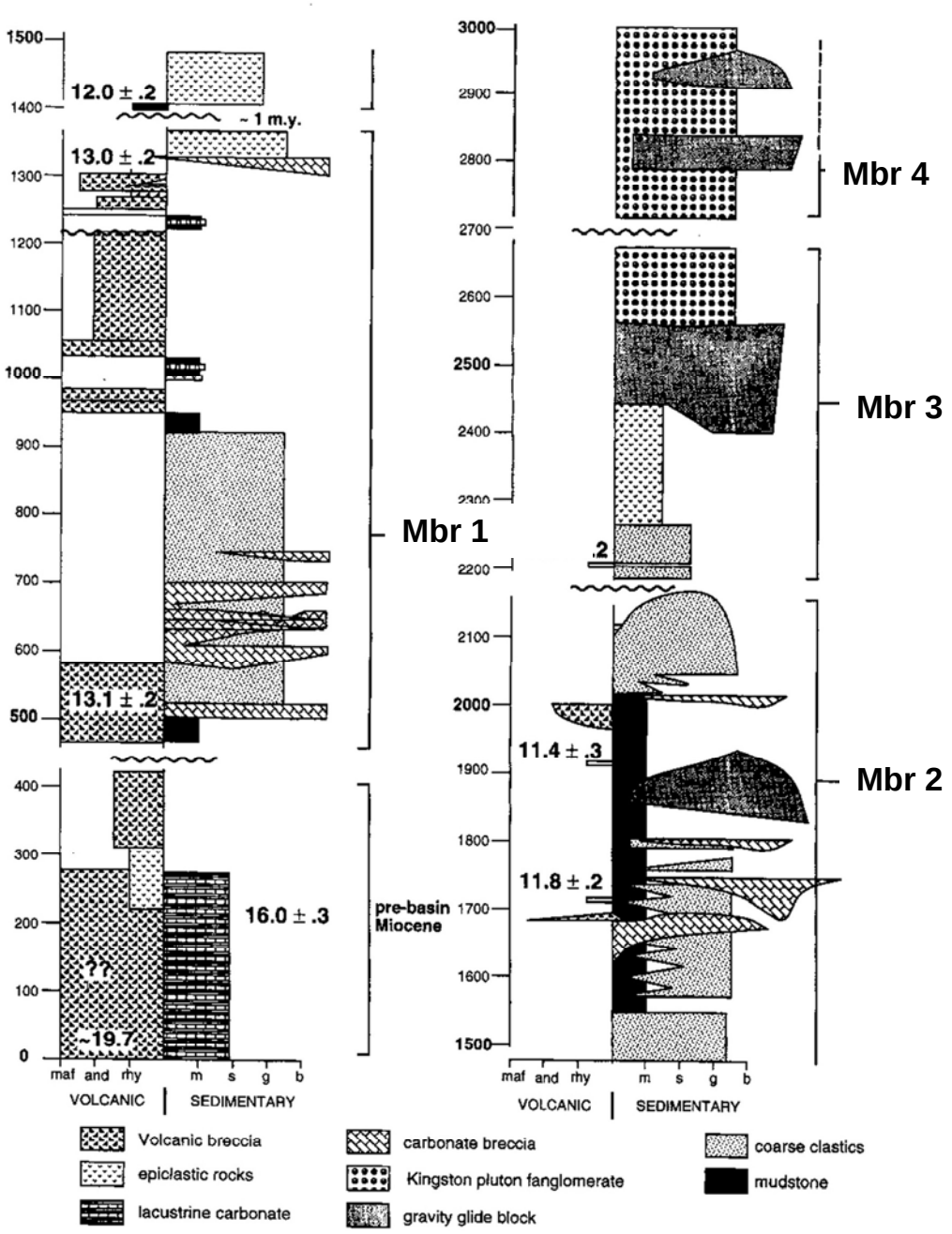

Figure 9. Stratigraphic column of units in the Sperry Hills. Modified from Friedmann (1999)

4. METHODS

4.1 Outcrop Methods

The Ibex Pass region was mapped during two three week winter seasons from 2006-2008. The region of interest has rock assemblages mapped using standard United States Geological Survey topographic maps, aided by interpretation of georeferenced Google Earth images. Data obtained in the field was acquired by direct input to a geographic information system (GIS) program ArcPad. Field data were then imported to ArcGIS 9.2 for final map preparation. A majority of mapping was completed to the north of Spring Road (Figure 10) area A and a small section to the south of Spring Road (Figure 10) area B. During December 2007 the rock units on the east side of Highway 127 (Figure 10) area C, were also mapped to examine to possible correlations to the volcanic assemblages mapped in the previous field season. Several rock samples were taken from all areas in the Ibex Pass region to aid in identifying all volcanic assemblages. Field observations were made in December 2007 in Wingate Wash to see if lithic packages were visibly similar to volcanics in Ibex Pass.

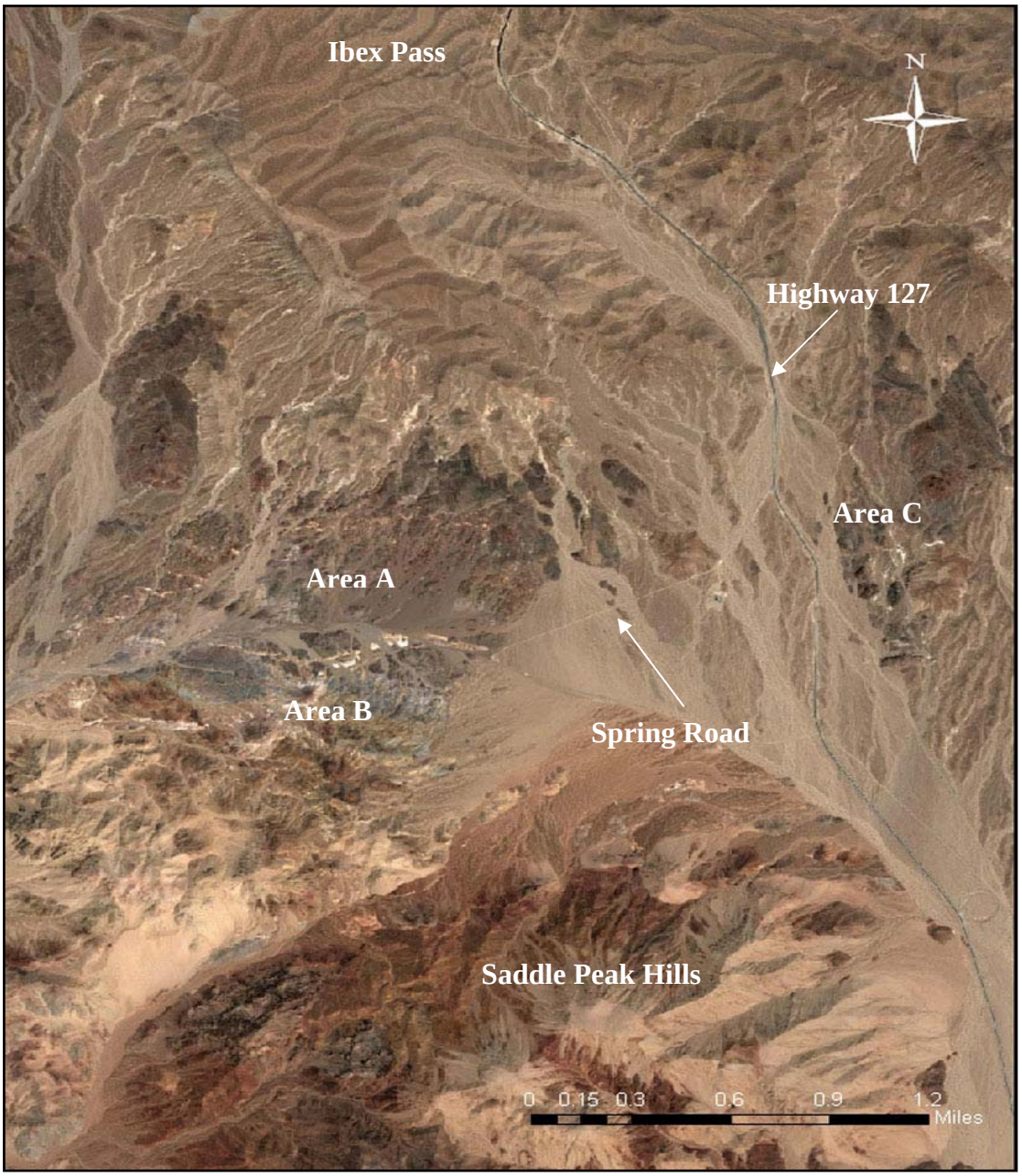

Figure 10. Location Map for geologic mapping in this study. Area A is location of where most geologic mapping was conducted. Area B is an area south of Spring Road where a small section was mapped. Area C is located to the east of Highway 127 and a small volcanic assemblage similar to units to the west of Highway 127 was mapped. Map modified from Google Earth.

4.2 Petrographic Methods

Twenty-eight thin sections were produced and then examined using a Leica DM 2500P microscope. Photographs of each thin section in cross polar light and in plane light are shown in (Appendix A). Heavy alteration of lithologic units in Ibex Pass has made several of them indistinguishable from one another in field. Therefore by making mineral identifications, defining textures, and determining approximate mineral modes, field identification of volcanic units can be clarified. Rock types were generally identified after petrological examinations are made. Knowledge of the volcanic packages allows for great support in producing a geological map of the study region and an understanding of the structural history.

4.3 Electron Microprobe Methods

Microprobe analyses were performed on six different tuffaceous units from southern Death Valley, at the University of Texas at El Paso. Tuffs are generally rich in feldspars and silica minerals, with only small amounts of other minerals (Vaniman, 2006). The mineral composition of tuffs, make it a good quality rock unit, to make geochemical correlations with. Volcanic tuffs in the Ibex Region and the Wingate Wash volcanic pile were sampled, to make comparisons. (Figures 11a and 11b) show the tuffs from the two comparable regions. By comparing chemical elements in the tuffs, I was able to see if the tuffs were genetically similar and give a history of their tectonic setting.

Figure 11a. Tuff bed in Wingate Wash.

Figure 11b. Volcanic Tuff in Ibex Pass.

Feldspars and clinopyroxene composition are plotted on ternary diagrams to compare mineral enrichments between tuff units. Feldspars are grouped by their molecular proportions of three end-members, albite, anorthite, and orthoclase (McBirney, 2007). Pyroxenes because they have several different compositional and structure forms are defined by their molecular proportions in the pyroxene quadrilateral (McBirney, 2007). The pyroxenes are classified based on their abundance of magnesium, calcium, or iron. Depending on their chemistry they can be classified as diopside, hedenbergite, augite, pigeonite, clinoenstatite, and clinoferrosilite. Comparisons of the chemical composition of the feldspars and pyroxenes of the two regions of signature volcanic assemblages can be conducted to assist in determining if the packages are chemically similar.

4.4 Whole Rock Chemistry

Nine rock samples from the Ibex Pass region were selected for X-ray fluorescence (XRF) and Inductively Coupled Plasma Mass Spectrometry (ICP-MS) analyses. (Figure 12a) show the localities for the sample collected for whole rock analyses. XRF is a method of elemental analysis that provides good accuracy for major elements and has in the region of 1 ppm detection limits (Reed, 2005). ICP-MS provides data on all elemental constituents of the whole rock sampled. Examinations on samples were conducted at Washington State University GeoAnalytical Laboratory during the summer of 2008. Several volcanic units in the correlateable offset point, Wingate Wash region, have geochemical analyses completed on them. Geochemical data from Yawn, 1995 and Luckow, 2005 is compared with the Ibex Pass region. In contrast, geochemical data is available on the pre-Shoshone volcanics and Shoshone volcanics from Thompson, unpublished data and will be compared with as well. The pre-Shoshone volcanics contain the Rhodes tuff which is believed to be a lithologic unit in Ibex Pass.

Chemical comparisons between units in Wingate Wash and Ibex Pass are carried out to verify similar geochemical abundances and between the pre-Shoshone volcanics and Ibex Pass units to see if they are correlative.

5. RESULTS

5.1 Ibex Pass Stratigraphy

Volcanic flows and rhyodacite plugs in the Saddle Peak and Sperry Hills, comprise the Ibex Pass volcanic field (Troxel and Calzia, 1994). Calzia and Romo (2000) describe the volcanic assemblages as volcanic flows consisting of olivine basalt, porphyritic andesite, and rhyodacite flows overlain by a porphyritic tuff, with landslide deposits of a mega breccia with clasts of granite at the top of the section. Topping (1993) correlates the tuff unit with an area just to the north of Ibex Pass which he correlated to the Rhodes tuff. An andesitic tuff breccia in the Ibex Pass field had producd a K-Ar whole rock and biotite ages of 12.5±0.04 Ma and 12.3±0.04 Ma respectively (Calzia and Romo, 2000). This age determination is compatible with a similar volcanic phase in Wingate Wash, however there is no stratigrahic context of where the sample was collected in relation to the Ibex Pass section under current study.

Very similar to Wingate Wash is a lack of continuity between identifiable units. The lack of continuity is common when there are many different flows with limited original lateral extent. These flows possibly get derived from different levels of magma chamber which can vary chemically after being erupted. (Yawn , 1995). Faulting and emplacement of a highly-altered, fine grained intrusive rock into the Ibex Pass volcanic assemblage also handicapped measurement of a complete section within the mapped area. Nonetheless, the general section is relatively clear and summarized in (Figure 12b).

The volcanic package is lying on pre-Tertiary basement at scattered localities from the northern Sperry Hills to the Saddle Peak Hills. The base of the volcanic section is poorly exposed in the mapped area because the weathering of the volcanic rocks above the basal contact typically shed extensive talus across the contact, typically burying the physical contact. At one

locality the contact appears to contain a thin gravel soil horizon below a rhyolitic unit, with both resting on steeply dipping Johnnie Formation. This contact relationship indicates the contact is an angular unconformity rather than an intrusive contact. In addition, the basic map pattern of the contact is suggestive of a gently north-dipping depositional contact. The contact is locally also complicated by emplacement of fine-grained intrusive rocks which are hard to distinguish from the volcanic assemblage, and by faulting, leaving some doubt on the nature of the lower contact of the pile.

Assuming the southern limit of the volcanic rocks is the basal unconformity, the general section in Ibex Pass area is shown in (Figure 13 and Figure 14), and comprises several general lithologic units. (Figure 15a) shows the location of the volcanic field in Ibex Pass where units were sampled. The oldest unit in the volcanic section is a ~100 m thick rhyolitic to dacite unit (D) that is resting on Precambrian quartzite of the Johnnie Formation. This unit is probably a mixture of volcanic rhyolite and associated shallow intrusives. The unit is a light purplish gray with an abundance of feldspars and amphiboles with a maroonish weathering. In thin section minerals identified are feldspars and amphiboles. The pyroxenes have been largely weathered to an altered iron oxide. Sample DV 34 (Figure 15b) which is classified geochemically as a dacite is from this volcanic sequence. Hydrothermal alteration of this package is very apparent and appears to be related to an intrusive plug that is situated along the boundary of this unit and overlying package.

The lower and middle package is intruded by plutonic rock of trachyandesite to trachyte (T1) composition (Figure 15c). Sample DV27 and DV 48 are representatives of this unit. This rock unit is poorly exposed due to extensive hydrothermal alteration that allows easy weathering of the rock. The trachyte is composed mainly of feldpars and the trachyandesite is intermediate

in composition from an andesite to a trachyte (Le Maitre, 1989). This intrusion has small east to west trending rhyolitic dykes distributed throughout it. This unit is ~100 m thick, light brown to gray in color, and has a visible red alteration. Feldspars and weathered amphiboles can easily be seen in hand specimen. A thin section sample DV57 produced from this location verified that the unit is a trachyandesite. Large amounts of feldspar and amphiboles are seen under the microscope with minor amounts of clinopyroxene

The middle package is a pyroclastic flow assemblage which comprises the bulk of the volcanic pile in Ibex Pass. This assemblage is lithologically diverse ranging from trachyandesite to rhyolite, but is dominated by more mafic end members of approximately andesitic to trachyandesite composition. This assemblage is dominated by pyroclastics ranging from volcanic breccias to volcanic conglomerates (Figure 15d). In part of the area a purple-orange andesitic flow unit lies in the section and contains clasts of andesite (Figure 15e). In other sections of this middle package the flow units are purple grey in color with apparent basalt clasts. This section is over 100 meters thick and appears to vary in composition from trachyte to trachyandesite. DV65 and DV73 are trachyandesite (TA) units from the section (Figure 15f). Sample DV90 (Figure 15g) is identified as a trachyte (T2) and is taken from the repeated section to the east of Highway 127.

Overlying this unit is a tan to white tuff that ranges in thickness from 1m to more than 10m (Figure 15h). In some localities this tuff is very lithic rich, but is commonly dominated by white ash and lava pumice fragments. In the east side of Highway 127 the tuff is over 10m in thickness but lithologically is very similar to units to the north of Spring road. In outcrop, this tuff is indistinguishable in appearance from the tuff unit in the Owlshead Mountains, but it is this tuff that has also been correlated to the Rhodes tuff (Topping, 1993). The tuff typically lies close

to the top of the local volcanic section, but in several localities other volcanic and sedimentary rocks were observed to overlie the tuff. This relationship may be due to an unconformity between lithologies.

The pyroclastic assemblage and the tuff are unconformably overlain by a megabreccia sheet (Figure 15i) that is at least 200 m thick. This breccia deposit is a nearly monolithic package comprised predominantly of granite clasts that contain distinctive rapikivi textures. The deposit also contains small amounts of quartzite and dolostone, however, that are probably derived from NeoProterozoic sedimentary rocks. It has been suggested (Topping, 1993 and Holm, 1995) that the granite is a landslide deposit derived from the granite of Kingston Peak in the Kingston Range 20 km east of the Sperry Hills. In addition, just north of the mapped area, large carbonate megabreccias sheets depostionally overlie the mega breccia with clasts of granite. These carbonate megabreccia sheets are similar to those observed to the east and the south in the Sperry Hills/Shadow Mountain basin system, suggesting possible correlation.

The unit that appears to be the youngest igneous rock is a white felsic rhyolitc intrusive dyke (R1). There is no evidence of a contact with this unit and mega breccia with clasts of granite which handicaps identifying relative age of this unit within the stratigraphic sequence. Based on field observations alone this unit was classified as a tuff unit until further investigations confirmed it was a rhyolitic intrusive unit. Sample DV67 is from the intrusional dike to the south of Spring Road (Figure 15j). The unit dips to the north and is extremely glassy. Small amounts of amphibole, biotite, and sanidine can be seen in the very fine grained unit. Due to the intrusion of this dyke it has produded a thin black vitrosphere where it is contact with the surrounding igneous rocks. This unit (R2) is largely vitric in the field and is represented by sample DV68 (Figure 15k). Whole rock analyses classified this unit as a rhyolite. In thin

section the minerals identified are phenocrysts of sanidine, with smaller amounts of biotite and amphibole. The unit has a very glassy matrix with small amounts of oxides present. Similar intrusions (R3) occur north of Spring Road as well throughout the volcanic package. Sample DV56 is from this intrusional dyke in the mapped area (Figure 15l). Visually, the three rhyolitc units are different from one another. (R3) is light purple in color with large phenocrysts of clustered feldspars. Scattered throughout the rock you can see visible mineral grains of amphibole.

5.2 Ibex Pass Struture

The Ibex Pass volcanic field is a region developed with movement along the dextral southern Death Valley fault system and early southwest extension. The Ibex Pass volcanic field sits at the westernmost edge of the Sperry Hills basin. This basin is associated with the topography of the basin and range extended terrain (Blakely et al., 1999). This basin is assumed to be filled with sedimentary and volcanic deposits that are in geochemical association with units in Wingate Wash.

Within the Ibex Pass volcanic field there is a system of northeast striking faults that show sinistral shifts. Throughout the volcanic section oblique slickenslides are evident on fault surfaces (Figure 15m). There is no distinct pattern on measurements of trend and plunge An arrangement of apparent normal faults, duplicate the section repetitively. The continuous units displayed throughout the section from east to west are a young volcanic pyroclastic unit, overlain by a white tuff, and all topped by the monolithologic breccia (Figure 15n). The displacement of volcanic units along the normal fault zones can be seen in the cross-section (Figure 13). The white tuff found in the middle of Area A to the north of spring road consistently dips steeply to the east and strikes at ~10 °. The tuff at the northwestern part of Area A dips to the southeast and the tuff in Area C dips to the northeast. Small faults can be seen within the tuff unit. The

majority of pyroclastic units dip to the east. All other rock units generally dip to the east. The structure of Ibex Pass is consistent with the displacement that has occurred along the southern Death Valley Fault Zone.

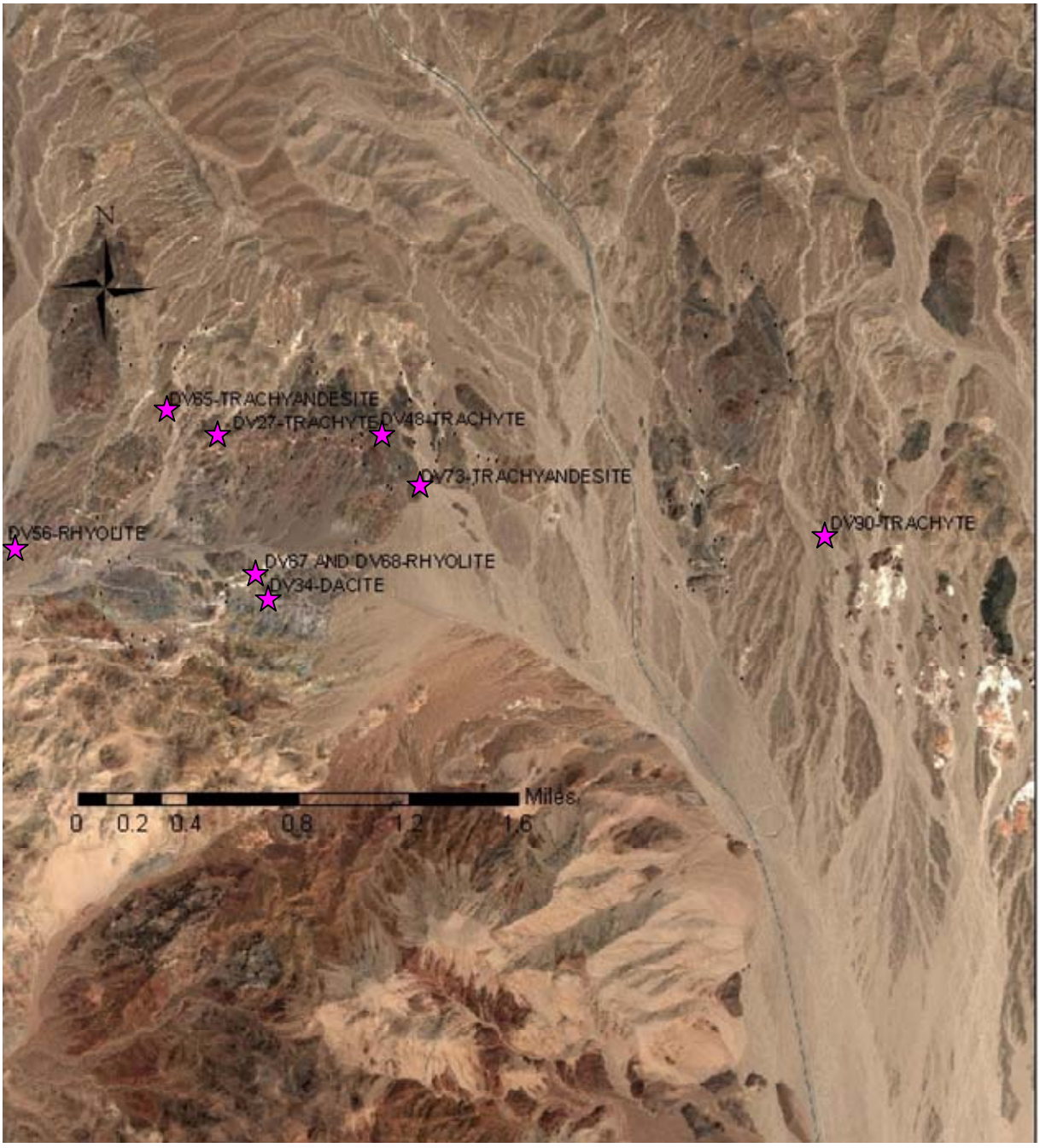

Figure 12a. Sample locations of whole rock analyses in Ibex Pass

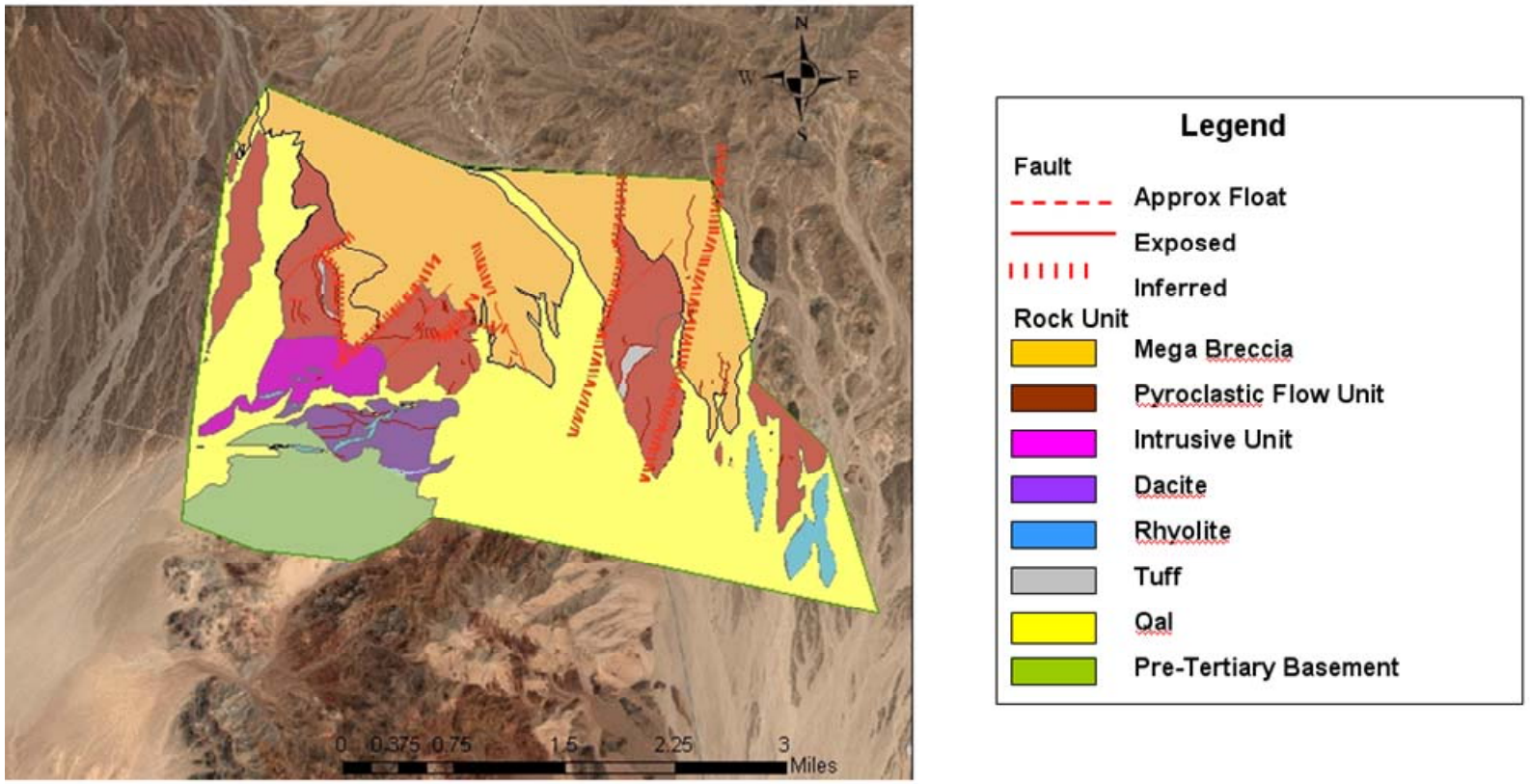

Figure 12b. Geologic Map of Ibex Pass.

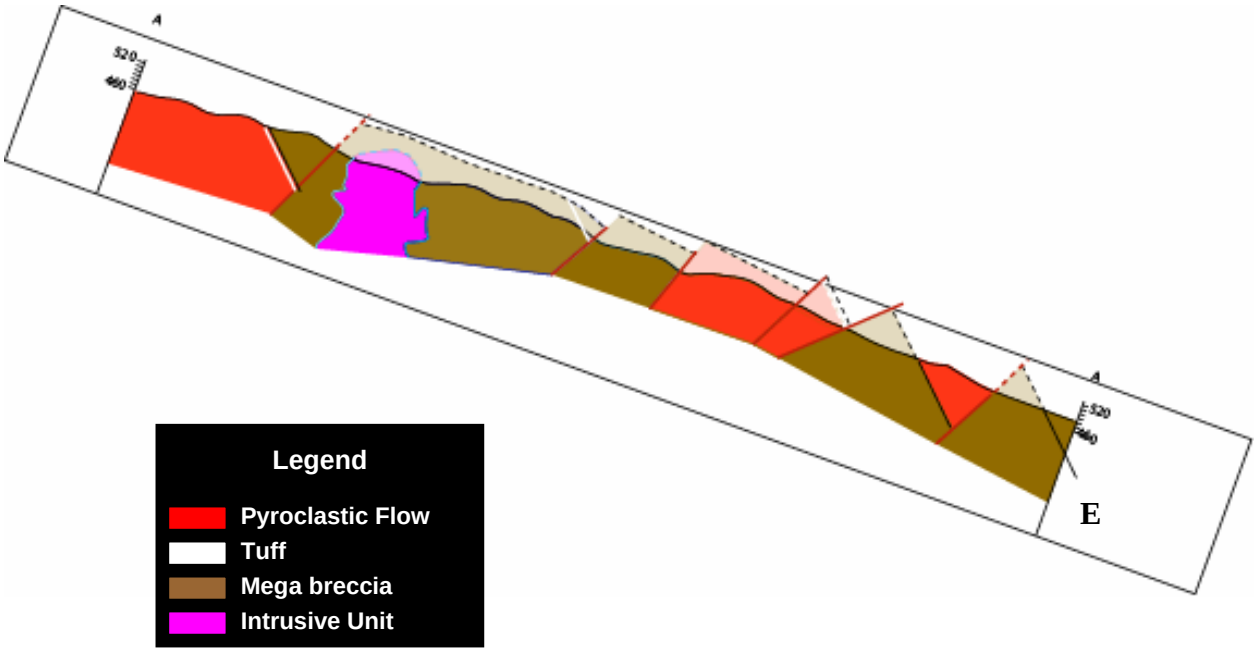

Figure 13. Cross-Section of Ibex Pass

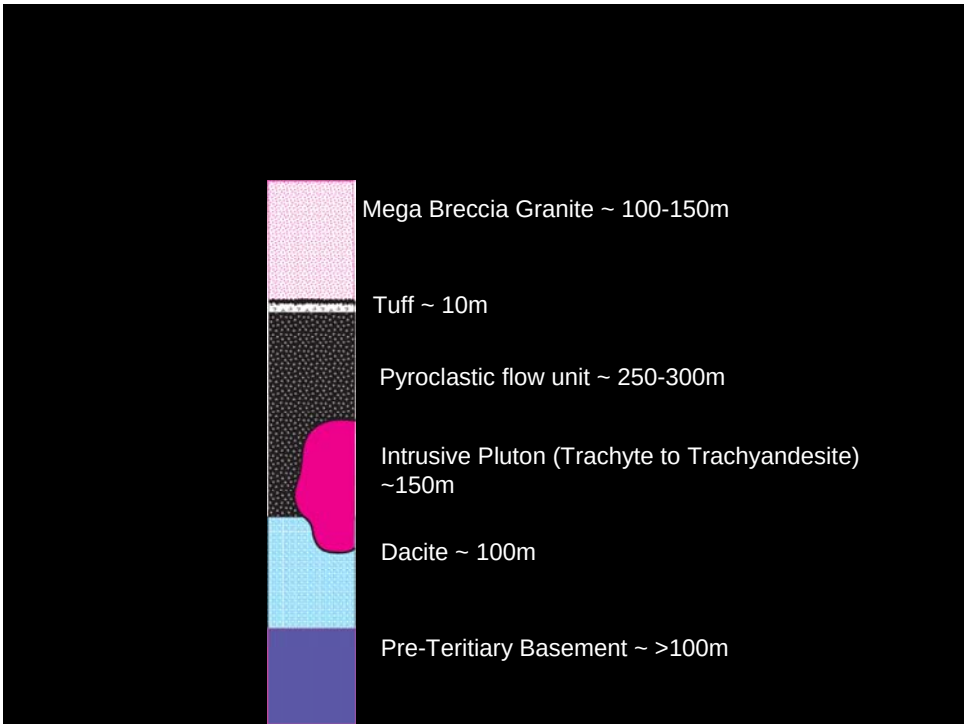

Figure 14. Stratigraphic column of volcanic assemblages in the Ibex Pass region.

Figure 15a. Photograph of Ibex Pass volcanic field.

Figure 15b. Dacite unit (D) in Ibex Pass.

Figure 15c. Intrusive trachyte of the volcanic section in Ibex Pass.

Figure 15d. Pyroclastic assemblage in Ibex Pass.

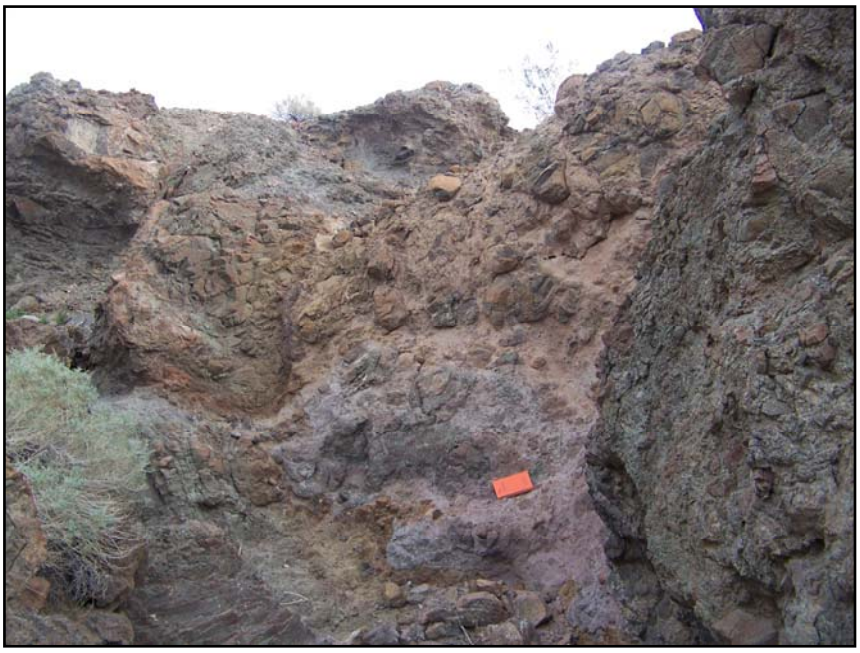

Figure 15e. Purple flow with clasts of andesite in Ibex Pass.

Figure 15f. Trachyandesite (TA) unit in Ibex Pass.

Figure 15g. Trachyte (T) unit in Ibex Pass.

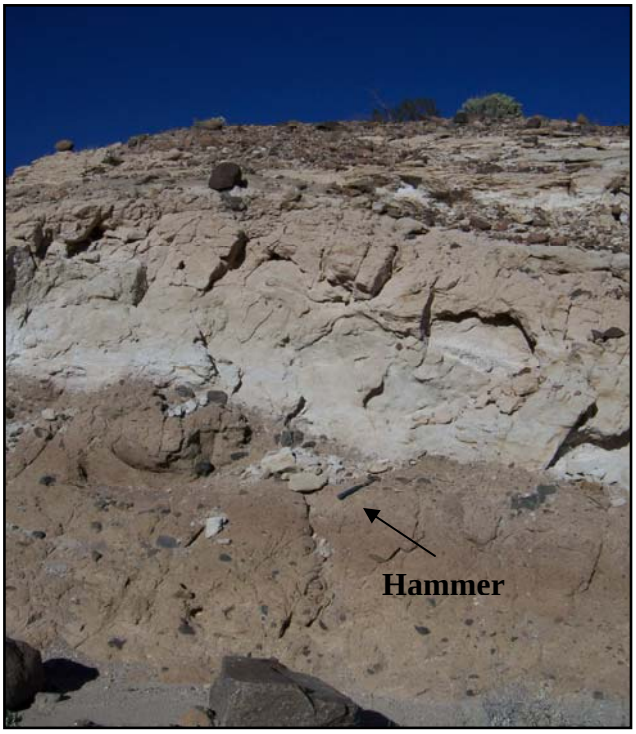

Figure 15h. Tan to white tuff unit in Ibex Pass.

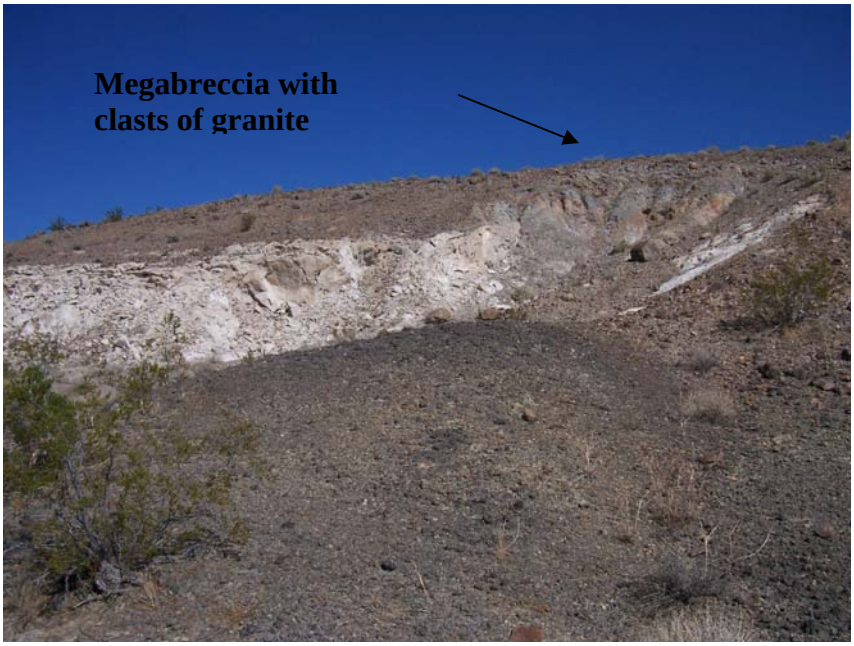

Figure 15i. Megebreccia with clast of granite in Ibex Pass, unconformably overly the white tuff unit.

Figure 15j. Rhyolite dyke(R1) in Ibex Pass.

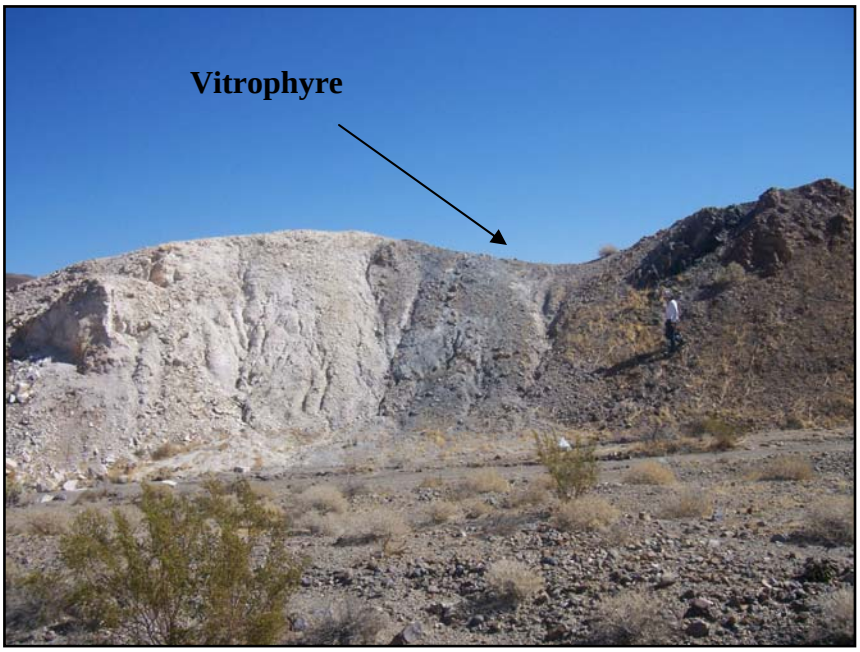

Figure 15k. Vitric rhyolite (R2) in Ibex Pass.

Figure 15l. Rhyolitic intrusion (R3) in Ibex Pass.

Figure 15m. Slickenslides on fault surface.

Figure 15n. Volcanic units repeated several times, due to normal faults in Ibex Pass.

5.3 Microprobe Analyses

Appendix A lists all chemical constituents and mineral identifications for tuff units in Ibex Pass and Wingate Wash from each thin section. The main minerals present in the tuffaceous units are needed to determine a magmatic setting for these tuffs. Certain minerals in the rock units can be compared with one another to see if they evolved from the same magma source. Formation of magmas due to subduction, extension, or a transitional phase can be reconstructed as well with mineral identifications.

(Figure 16 a.-d) are from Ibex Pass and (Figure 16e-f) are from Wingate Wash and have various feldspars plotted on the ternary diagrams from their tuff units to aid in determining magmatic composition. (Figure 16g) has all the feldspars from sampled tuffs in Ibex Pass and Wingate Wash. (Figure 17a-d) are from Ibex Pass and (Figure 17e-f) are from Wingate Wash and have their clinopyroxene data plotted on clinopyroxene ternary diagrams. All clinopyroxenes from the two comparable field locations are shown on (Figure 17g).

The feldspars from tuff units in the main field locality in Ibex Pass, plot toward the albite and orthoclase end members. DV60 has three feldspars near the albite range and DV74 has one feldspar distinctly similar to DV60. Two other feldpars from DV74 plot near the Ortholcase rich classification. The tuffs in this area are composed of clinopyroxene, feldspar, magnetite, glass, nephiline, zircon, amphibole, and spinel. Tuffs from the east side of Highway 27, samples DV93 and DV79 have feldspars that are plotting in the sanidine range. One feldspar from sample DV79 plots in the albite range and one in the orthoclase field. These tuffs have minerals that include sphene, cheksavite, magnetite, feldspars, hematite, clinopyroxene, biotite, and glass.
All feldspars from the two tuffs sampled in Wingate Wash plot in the orthoclase rich area, except sample DV2000A which has two feldspars that are identified as sanidine. Minerals identified in

these two tuffs include feldspar, zircon, zeolite, magnetite, clinopyroxene, biotite, apatite, and glass.

The clinopyroxenes of the six tuffs samples all plot in the diopside range with a few falling into the augite classification. Both DV74 and DV60 have clinopyroxene in the augite field, DV74 has a cluster of several clinopyroxene in the diopside classification. Each sample from the east side of Highway 27 had one clinopyroxene plotted on the diagram. DV93 and DV79 both had their clinopyroxene plotting in the exact same place in the augite field. The tuff units from Wingate Wash had one clinopyroxene each plotting in the diopside range. DV2000A had one feldspar that plotted in the augite area. Clinopyrexene from DV2000A, DV79, DV93, DV74, and DV60 all plot in the exact same place on the ternary diagram, which can be shown by the overlapping of symbols on (Figure 17g).

To further compare geochemical constituents in the tuff units from Ibex Pass and Wingate Wash, the composition of glass shards in the tuffs were examined for possible correlation. The data is not too reliable to make geochemical comparisons with, because not many points were studied from each sample and glass totals were generally very low. The glass in the tuff from Wingate Wash has a greater total of calcium compared to the tuff from Ibex Pass. The reason may be magnesium and calcium mineralization veins along normal faults in the Wingate Wash, which are contributed to small amounts of hydrothermal alteration in volcanic and alluvial deposits in the Wingate Wash region. Metamorphism of this degree can greatly cause changes in the geochemical signature, which may be the cause for the calcium fluxuation . (Luckow, 2000).

Microprobe analyses performed on tuff units in Ibex Pass and Wingate Wash aids in determining if tuff units contain similar mineral assemblages. However, it does not accurately demonstrate that tuffs are from the same source. Feldspars and clinopyroxenes are common minerals found in tuffs, because of this it may imply they evolved from different sources. If major differences were found between mineral assemblages it could help conclude they are not similar, but since they are similar it adds more evidence that the two tuff units may be the same.

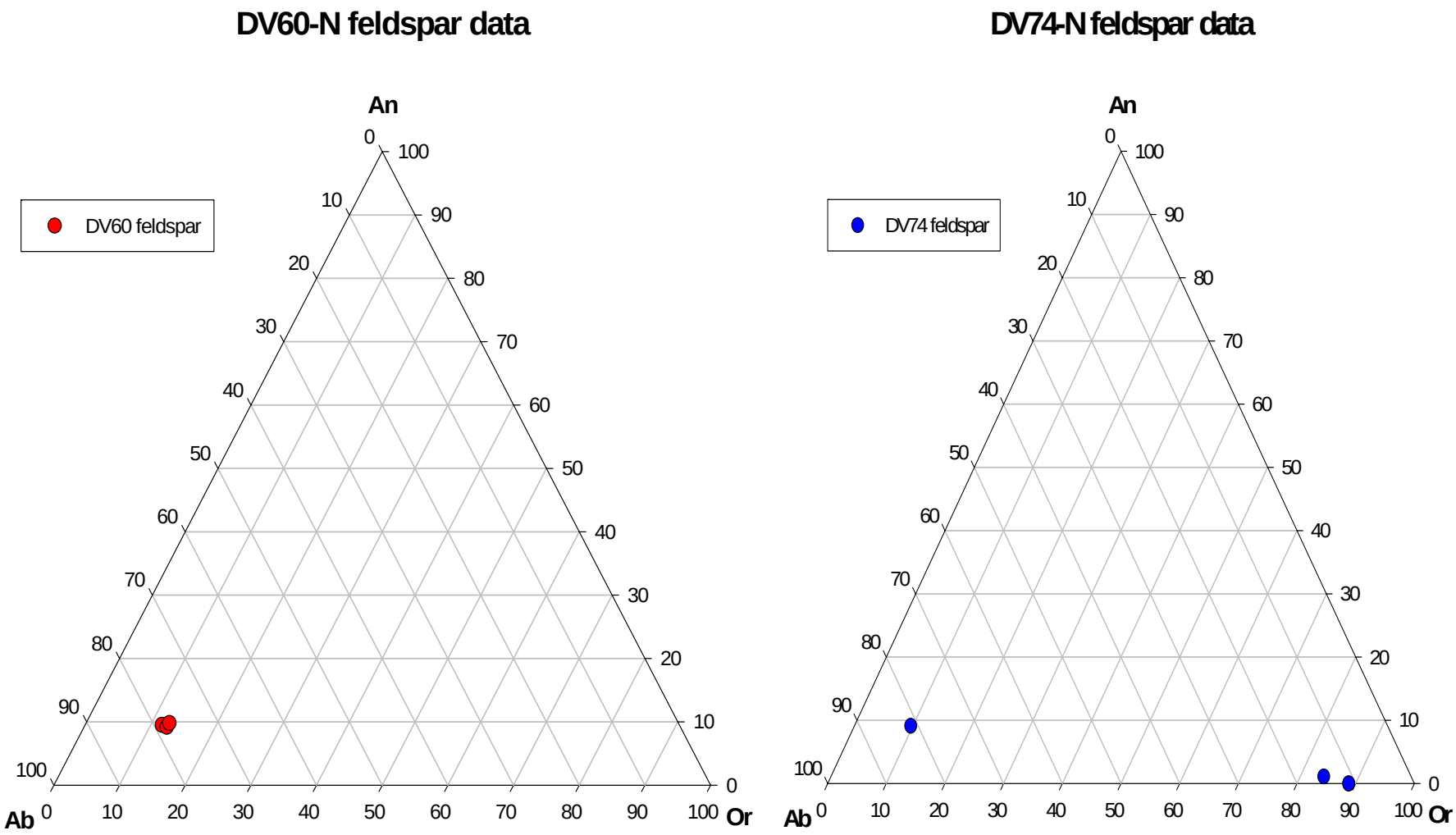

Figure 16a-16b. Feldpar ternary diagrams for tuff units DV60 and DV74 to the north of Spring Road.

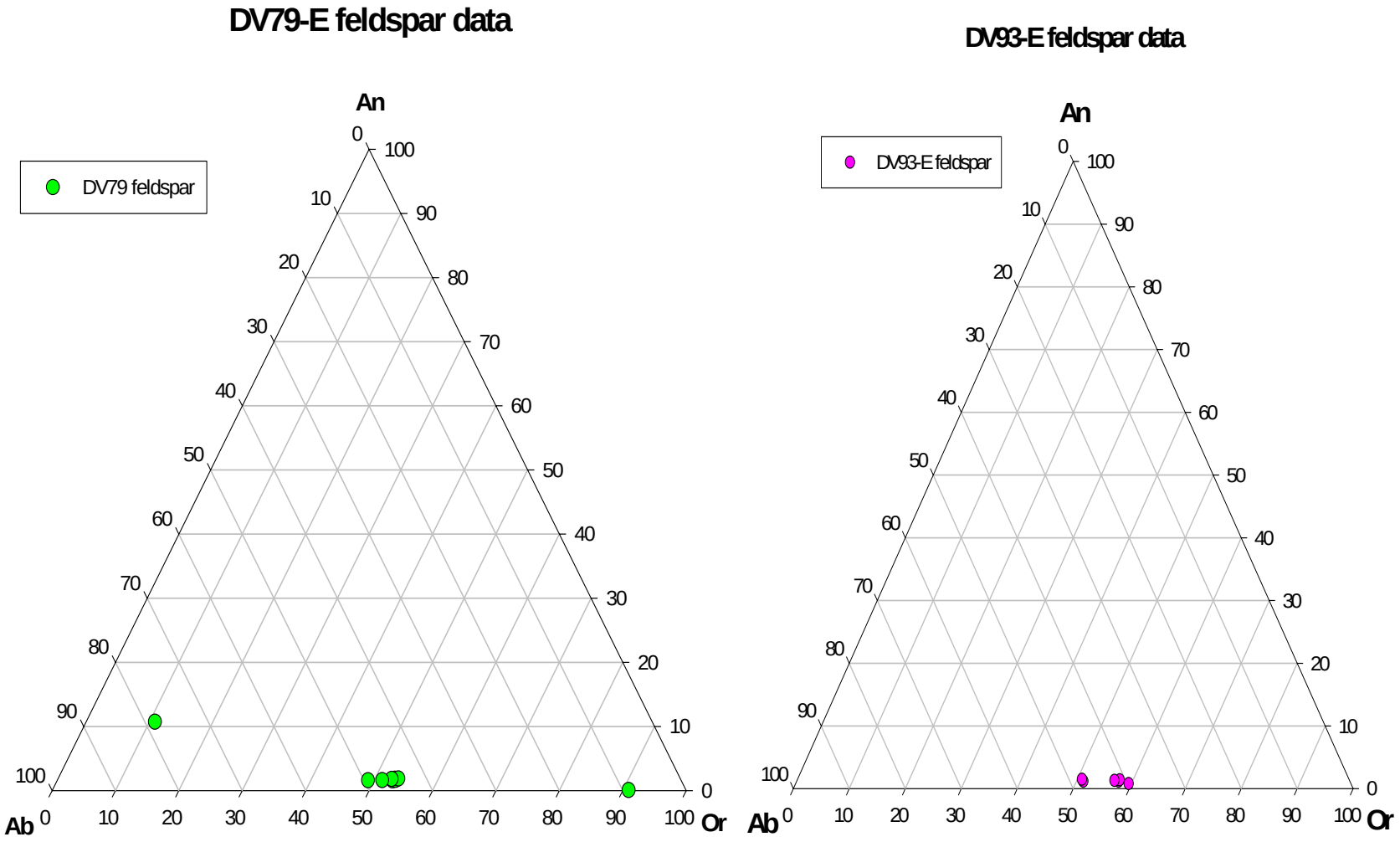

Figure 16c-16d. Feldspar ternary diagrams for tuff units DV79 and DV93 east of Highway 127

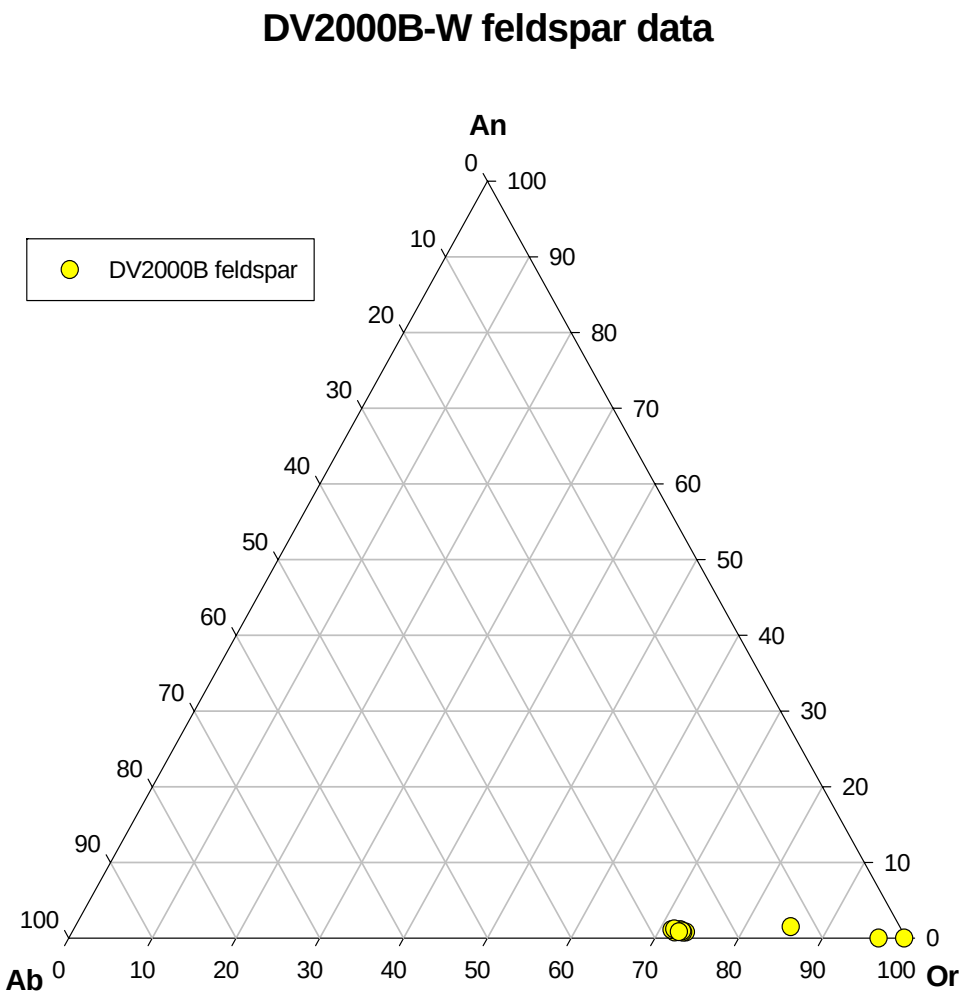

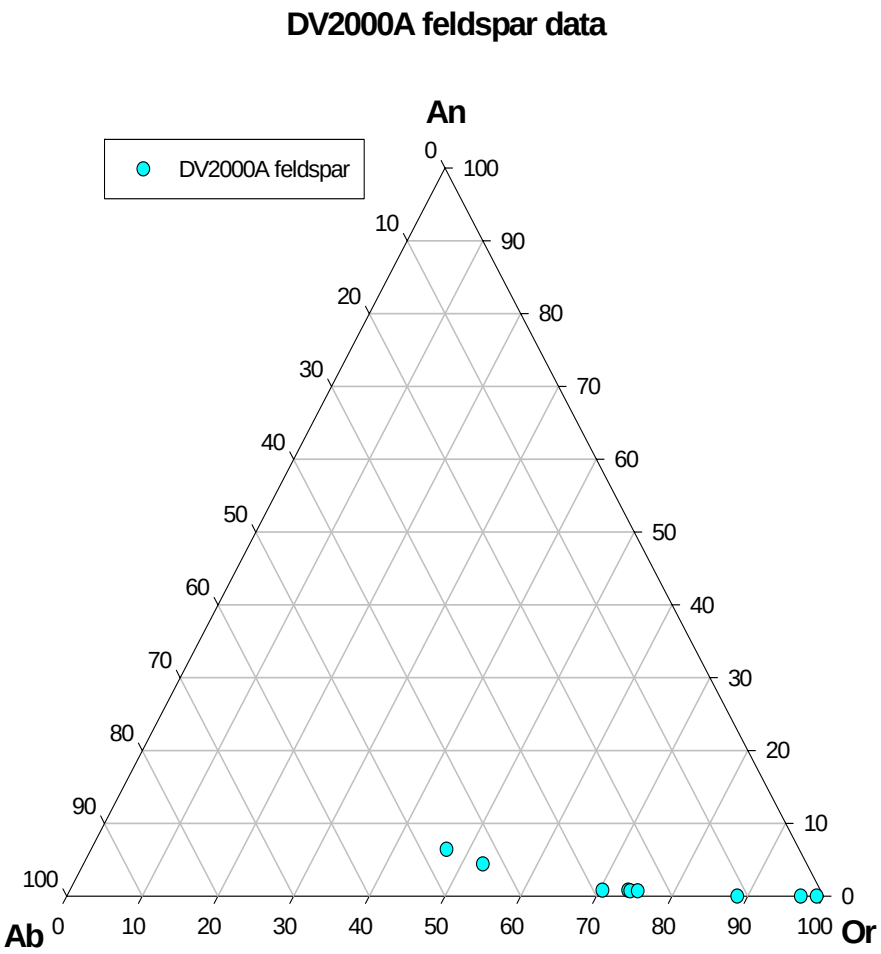

Figure 16e-16f. Feldspar ternary diagrams for tuff units DV2000B and DV20000A in Wingate Wash.

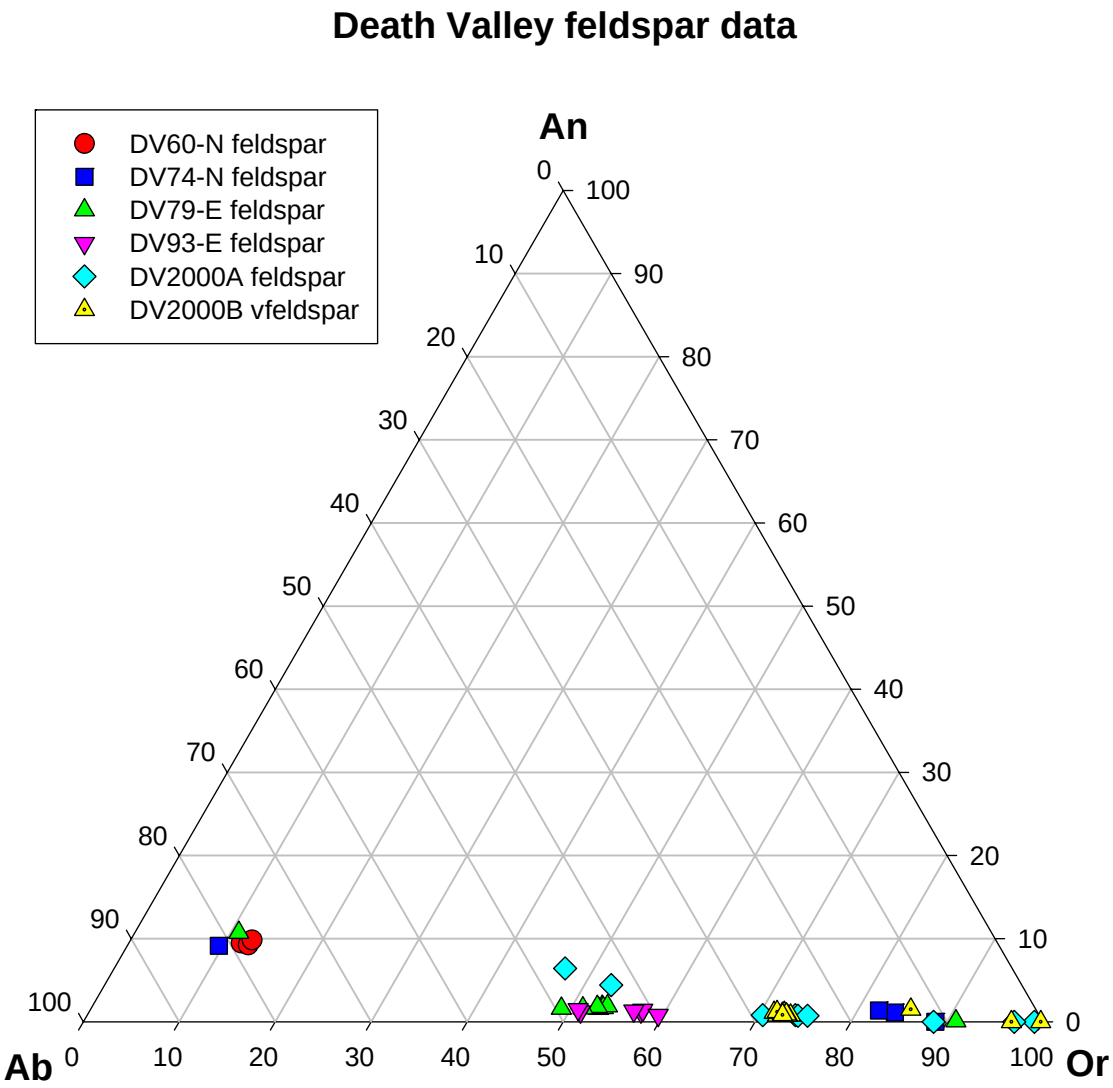

Figure 16g. Southern Death Valley feldspar ternary diagram.

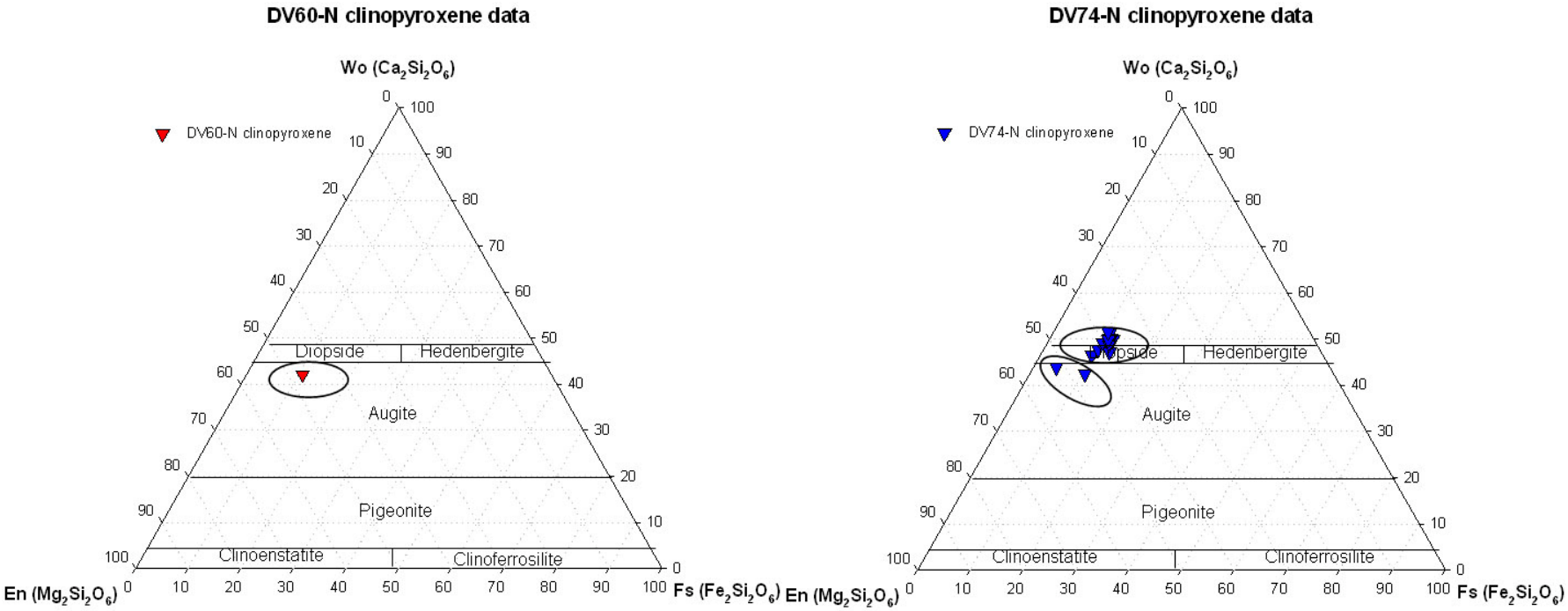

Figure 17a-17b. Clinopyroxene ternary diagrams for tuff units to the north of Spring Road.

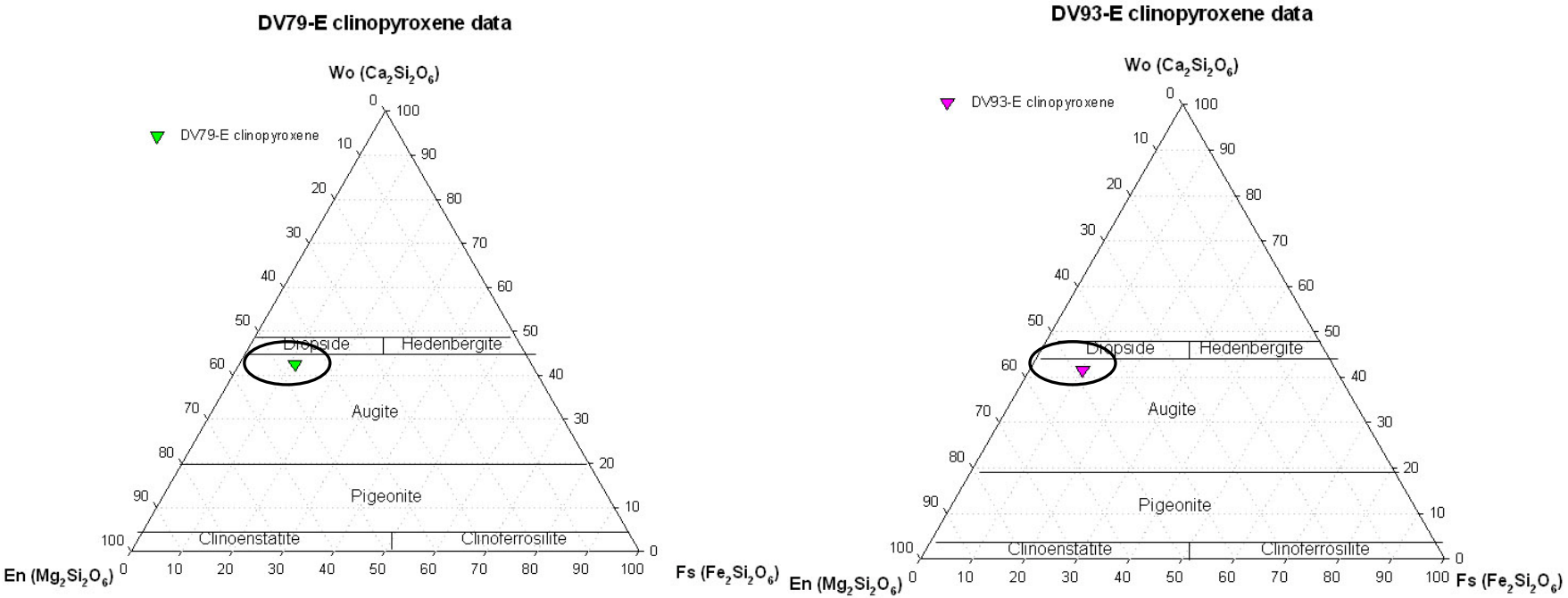

Figure 17c-17d. Clinopyroxene ternary diagrams for tuff units to the east of Highway 127.

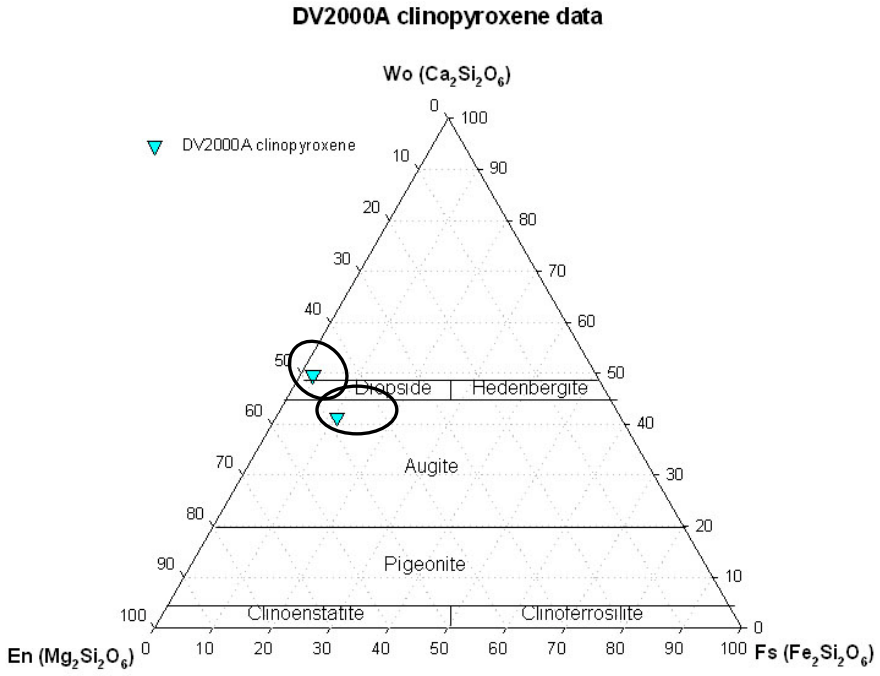

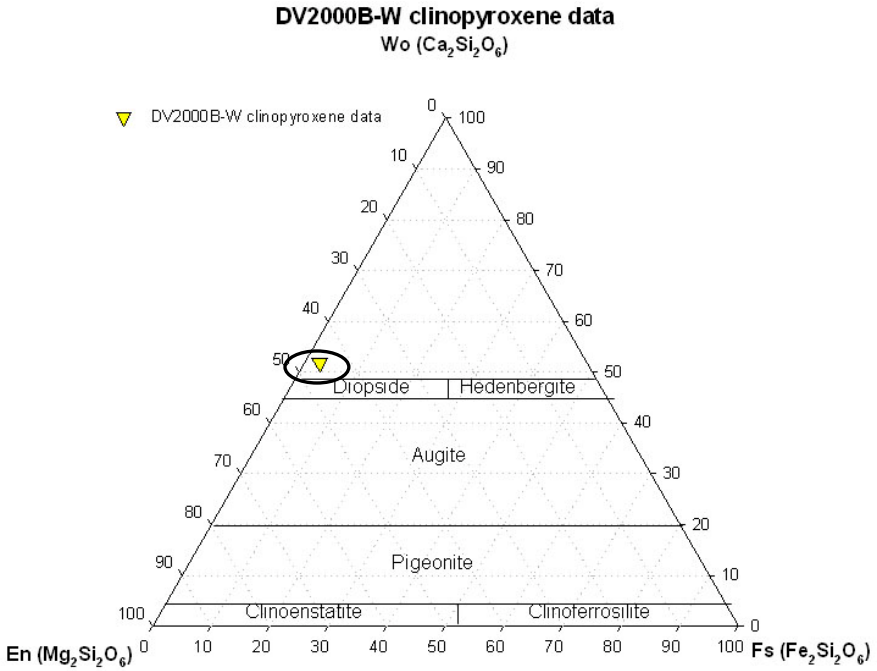

Figure 17e-17f. Clinopyroxene ternary diagram for tuffs units in Wingate Wash.

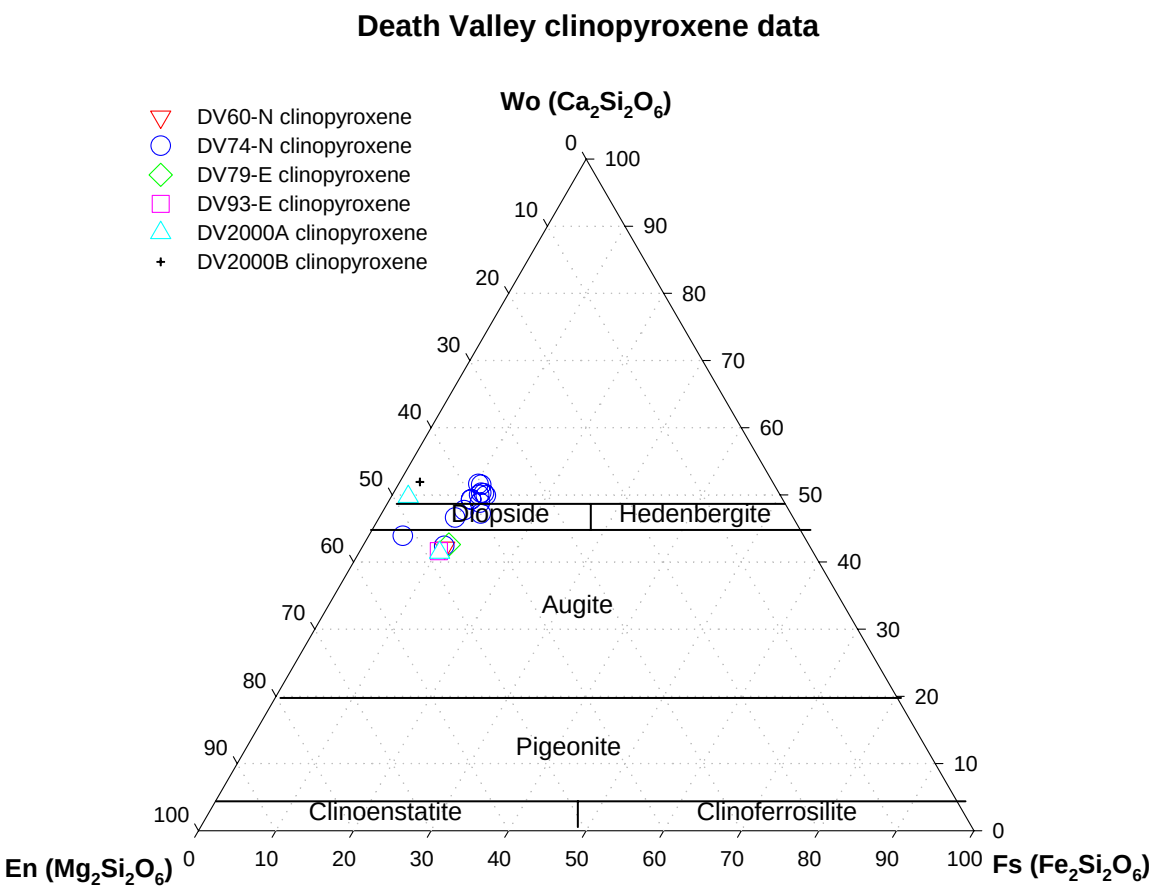

Figure 17g. Southern Death Valley clinopyroxene ternary diagram.

5.4 Whole Rock Analyses

5.4.1 TAS Classification

The total alkali silica classification is used for volcanic rocks, in determining a root name based on the value of Na2O+K2O and SiO2 contained in the rock unit (LeMaitre, 1989). A TAS diagram (Figure 18) shows the chemical makeup of rock units in Ibex Pass. The sampled units from Ibex Pass are predominately trachyte to trachyandesite and rhyolites. There is one unit from Ibex Pass that was identified as a dacite. These volcanic units all plot in the alkaline field on the figure.

5.4.2 Harker Diagrams/Variation Diagrams

Harker diagrams are very useful in displaying major and minor element chemistry in volcanic units. These bivariate plots chart major and minor element oxides against silica concentration. These diagrams can generate trends showing magmatic evolution with enrichment of silica and provide insight into the processes of magmatic differentiation. (Winter, 2001). Bowen (1928) extensively used these diagrams to illustrate the liquid line of descent during igneous differeation (Shaw, 2006). Variation diagrams are also useful, in acquiring information on the processes that created these magmamtic rocks. Plotting selective elements against each other can display magmatic trends and be helpful in comparing volcanic units geochemically (Shaw, 2006).

(Figure 19) displays the subalkaline composition of volcanic units in Ibex Pass. High, medium, and low K fields can be seen when plotted against K2O. The units in Ibex have values of 2.99%-6.02%. All but one of the nine volcanics sampled from Ibex Pass,a rhyolite DV68, plot in the high-K range and the rhyolite plots almost on the line (Figure 20). Major elements are plotted against silica for rock samples from Ibex Pass (Figure 21). Na2O and three minor

elements are also plotted against silica (Figure 22).Certain trace elements versus silica are displayed on Harker diagrams (Figure 23-24). The units range in silica value from 59.4 % to the rhyolitic range that reaches 75.3 %. K2O increases as silica increases and Na2O and Al2O3 remain constant as silica increases. TiO2, FeO, CaO, P2O5, MgO, and MnO decrease as the percentage of silica rises.

The values in Al2O3 range from 13.3%-18.74%, and FeO values are low in the rhyolites starting with 0.96% and increase to the maximum value of 5.59% for a trachyandesite unit. CaO levels vary from 0.79%-6.34% and MgO values are from 0.55%-3.34%. Levels are CaO and MgO are low in the rhyolites and increase in percentage in the trachyandesites. TiO2, MnO, and P2O5 all are under 1% composition each with again the rhyolites having less percentage values than the more mafic rich trachyandesites. The trachyte units and dacite are in between the minimum and maximum of values for major and minor elements.

The trace elements vary extensively between different lithologic units in Ibex Pass. Nb is 12.56ppm in a trachyandesite unit and increases up to 27.62ppm in a trachyte rock. Th is low at 7.9ppm and increases to 38.1 ppm, Ba lowest amount is 265.8ppm and maximum is 2182ppm. Sr ranges between 137.7ppm and 1859ppm and the range for Y is 10.4ppm and 32.8ppm.Rb is between 84.2ppm to 244.4ppm in value, Zr ranges from 138.2ppm to 551.1ppm, and La lowest value is 52ppm and highest is 105.3ppm. Trace element values in La, Zr, Y, Sr, Ba, and Nb are very high in the trachyte units. The rhyolite units are higher in Rb and Th and lower in Sr, Ba, Y, and Zr.

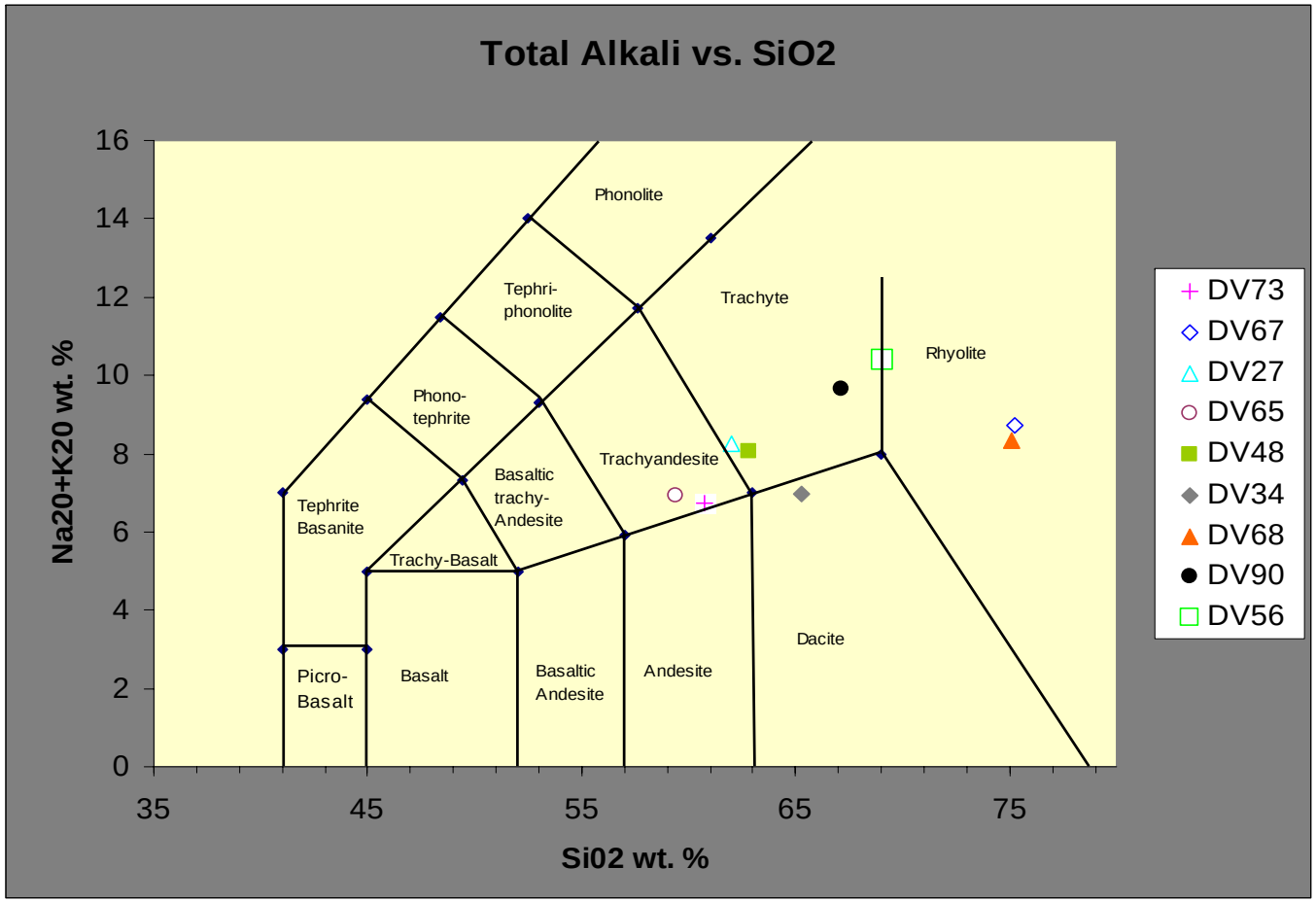

Figure 18. Total alkali vs. silica diagram for volcanic units in Ibex Pass units.

5.4.3 Spider Diagram

Spider diagrams are multicomponent diagrams that are used to compare the abundances of diagnostic elements. Certain elements are normalized by dividing their abundances in the sample by those in a suitable reference. (McBirney, 2007). The spider diagrams (Figure 25a-25d) are constructed by using the chronditic meteorites values listed in Appendix C. These diagrams are useful in trying to derive a magmatic signature and tell about the source of the magma. Volcanic units sampled in Ibex Pass are all generally enriched in Pb, Nd, U, and Th. A trachyte unit Sample DV48 is extremely enriched in Rb. The units appear to be depleted in P, Ti, Ta, and Nb. The rhyolitic units also have a distinct depletion in Ba.

5.4.4 Rare Earth Chemistry

The rare earth elements are grouped together because they display similar geochemical behavior. Smaller and heavier REES (HREES) enter the mineral phase during strong fractionation, the remaining melt is enriched with lighter and larger REES (LREES). (Yawn, 1995). The behavior of rare earth elements in Ibex Pass volcanics displays a similar behavior except for rhyolitic units which display an Eu anomaly (Figure 26). The rhyolitic units are more depleted in rare earth elements, especially the LREEs because they are more felsic in composition. The relationship between the rare earth elements in Ibex Pass implies that the magma is not too evolved.

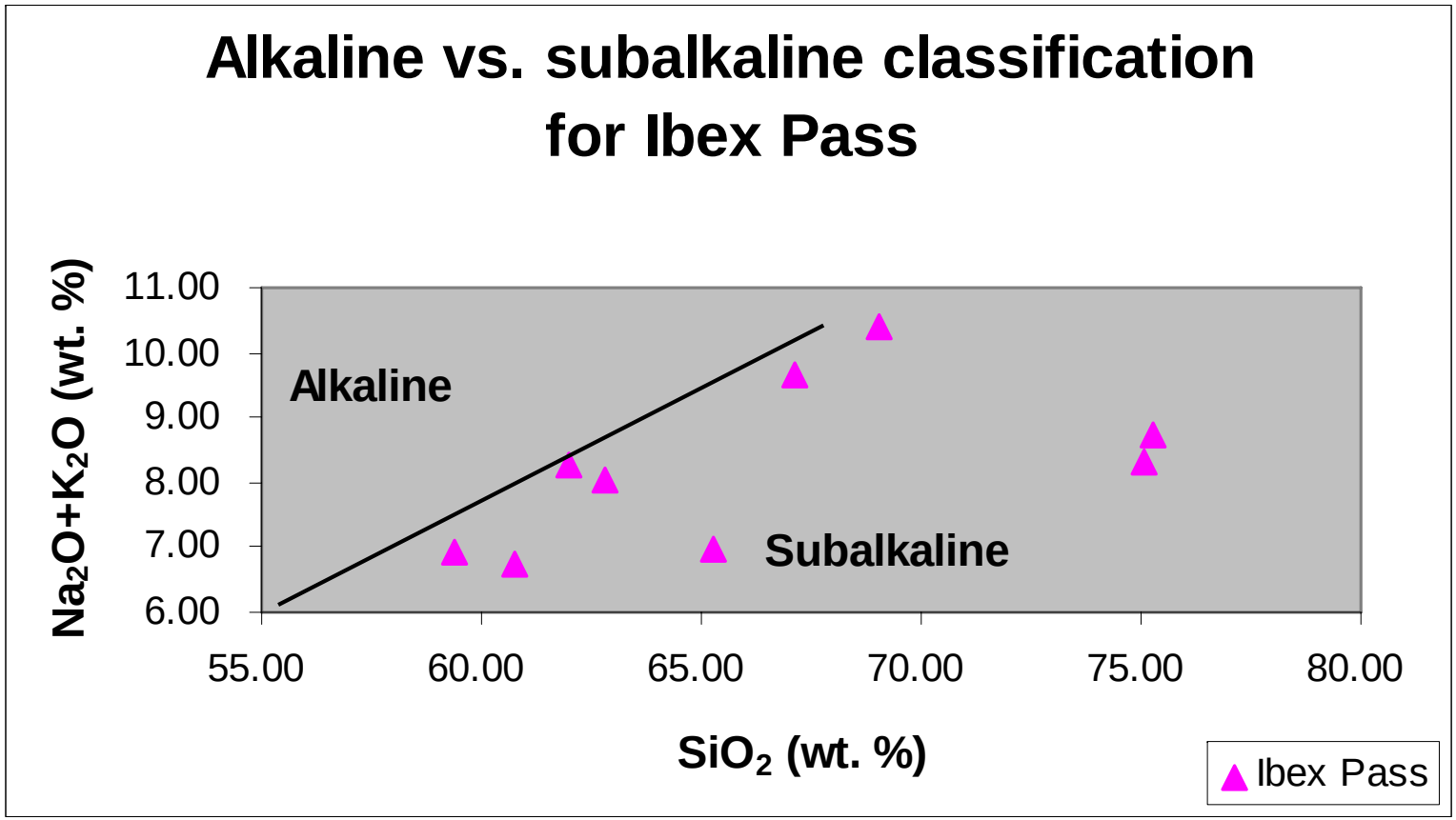

Figure 19. Alkaline vs. subalkaline classification for all units in Ibex Pass (Irvine, Barager, 1971).

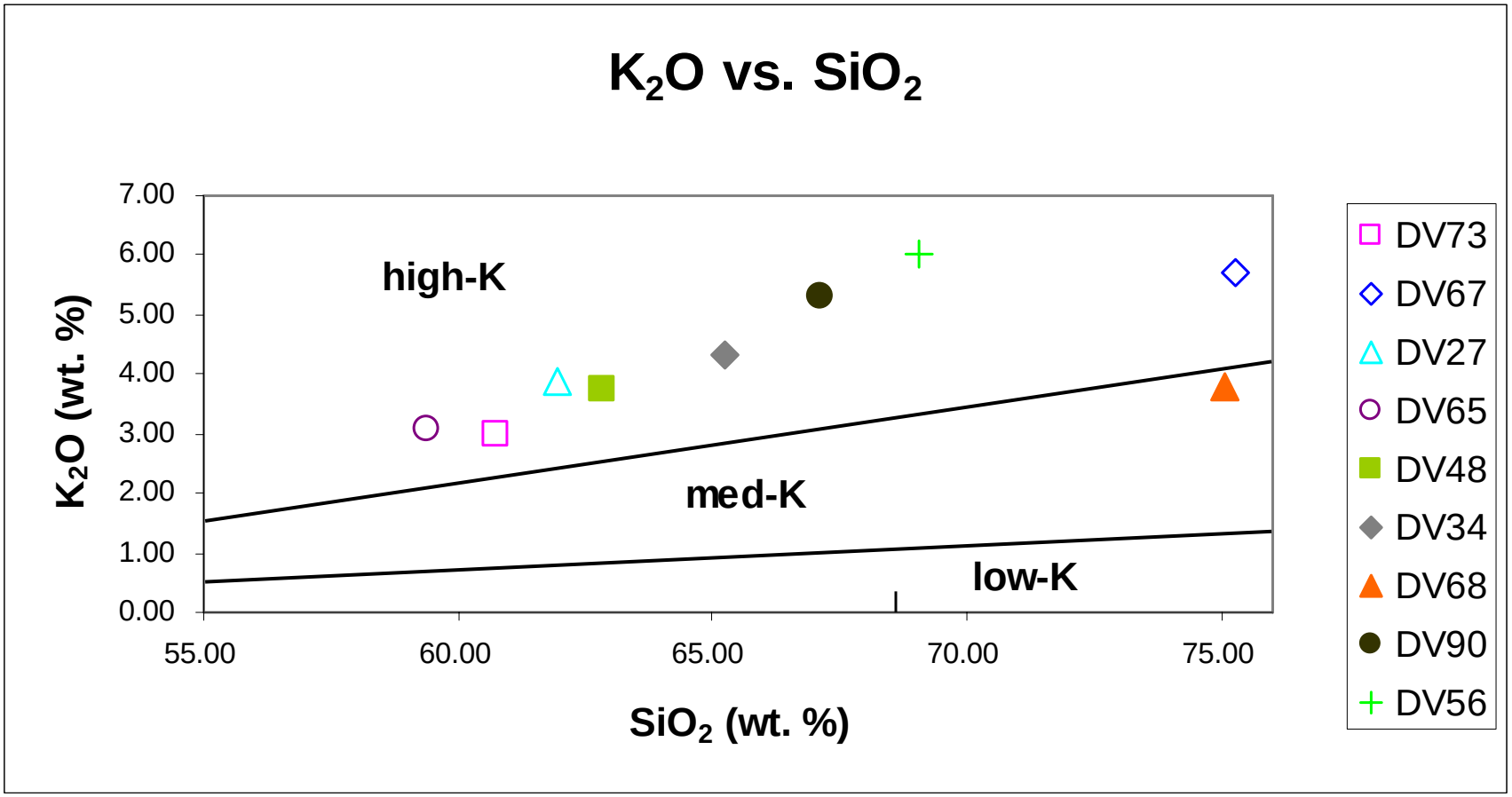

Figure 20. High, medium, and low-K fields for all Ibex Pass units.

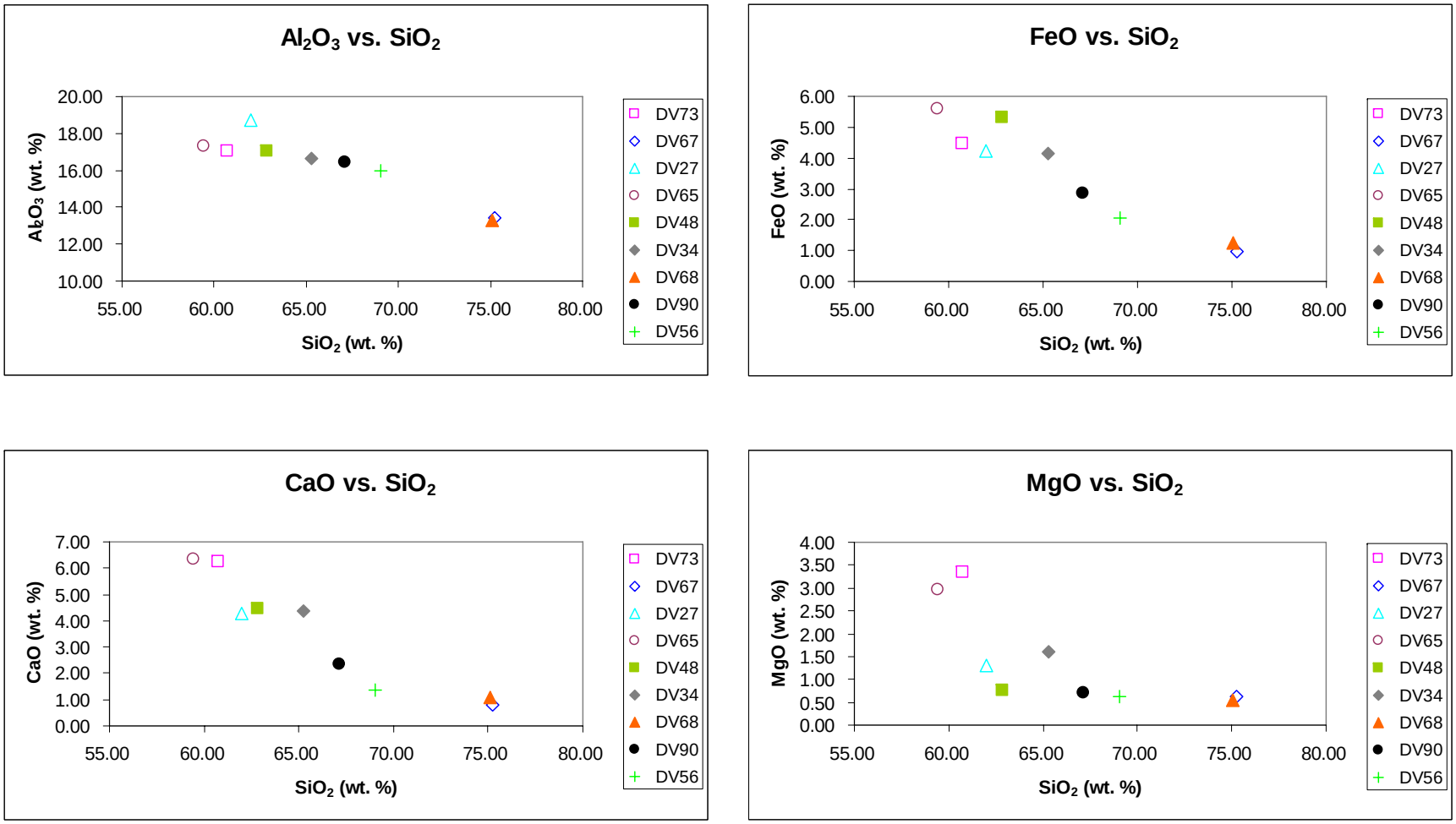

Figure 21. Major elements for units in Ibex Pass vs. silica.

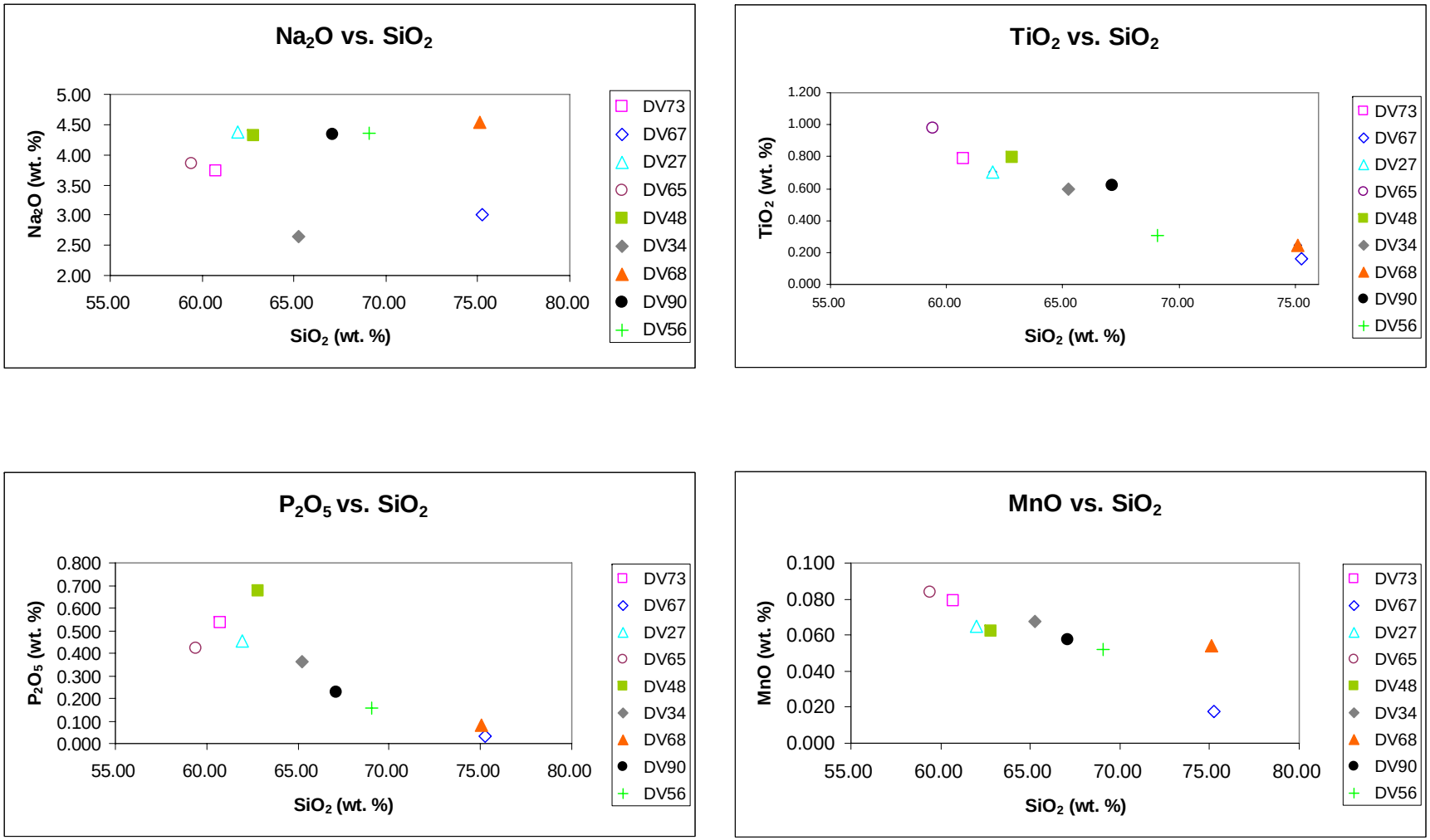

Figure 22. Major and minor elements for units in Ibex Pass vs. silica.

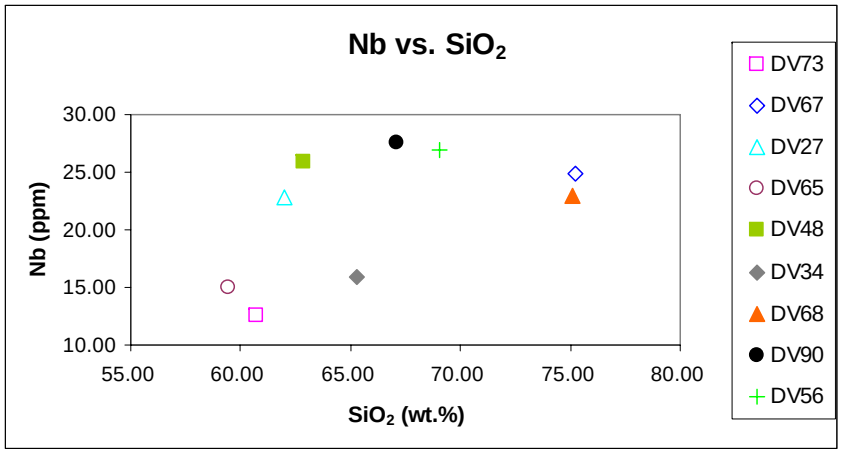

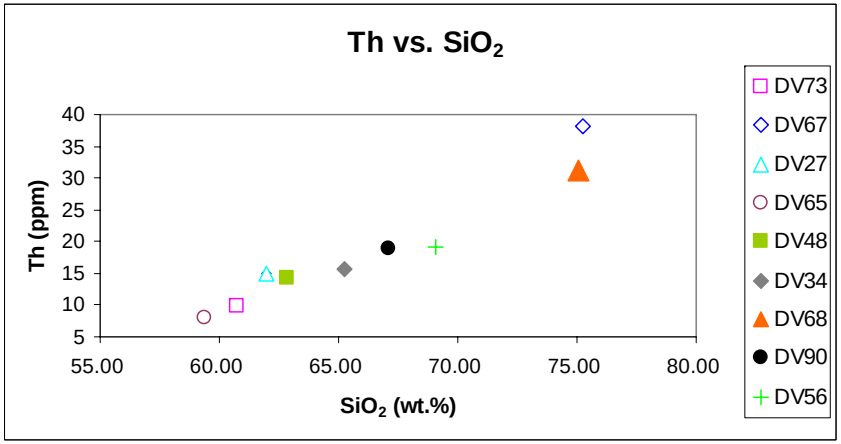

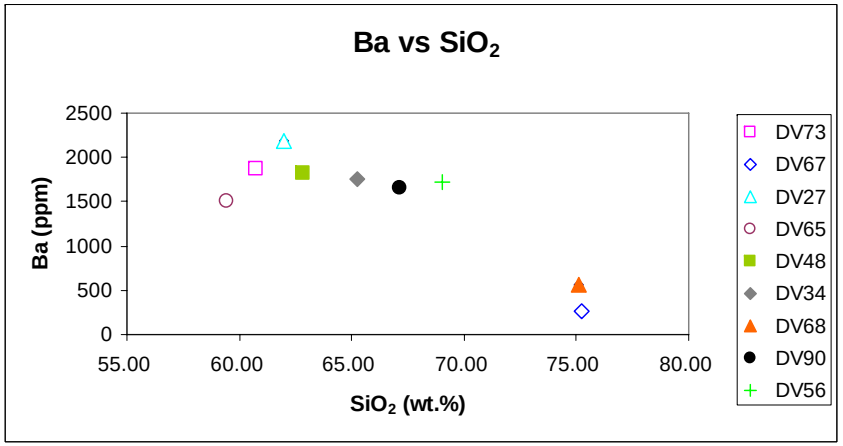

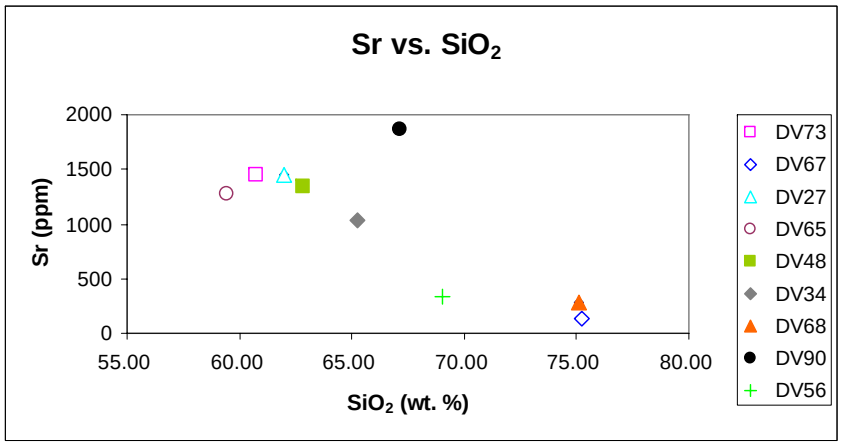

Figure 23. Trace elements for units in Ibex Pass vs. Silica.

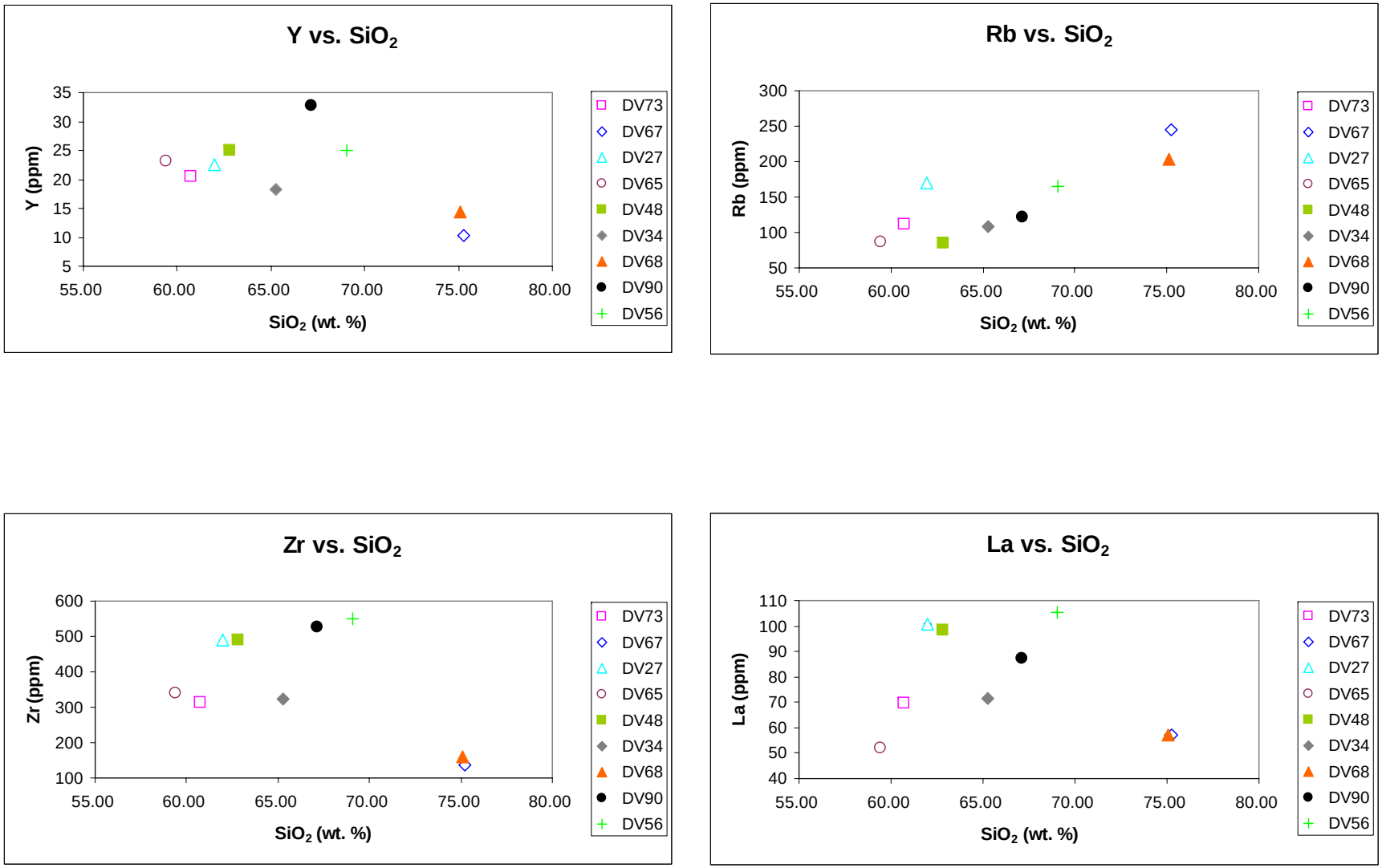

Figure 24. Trace elements for units in Ibex Pass vs. Silica.

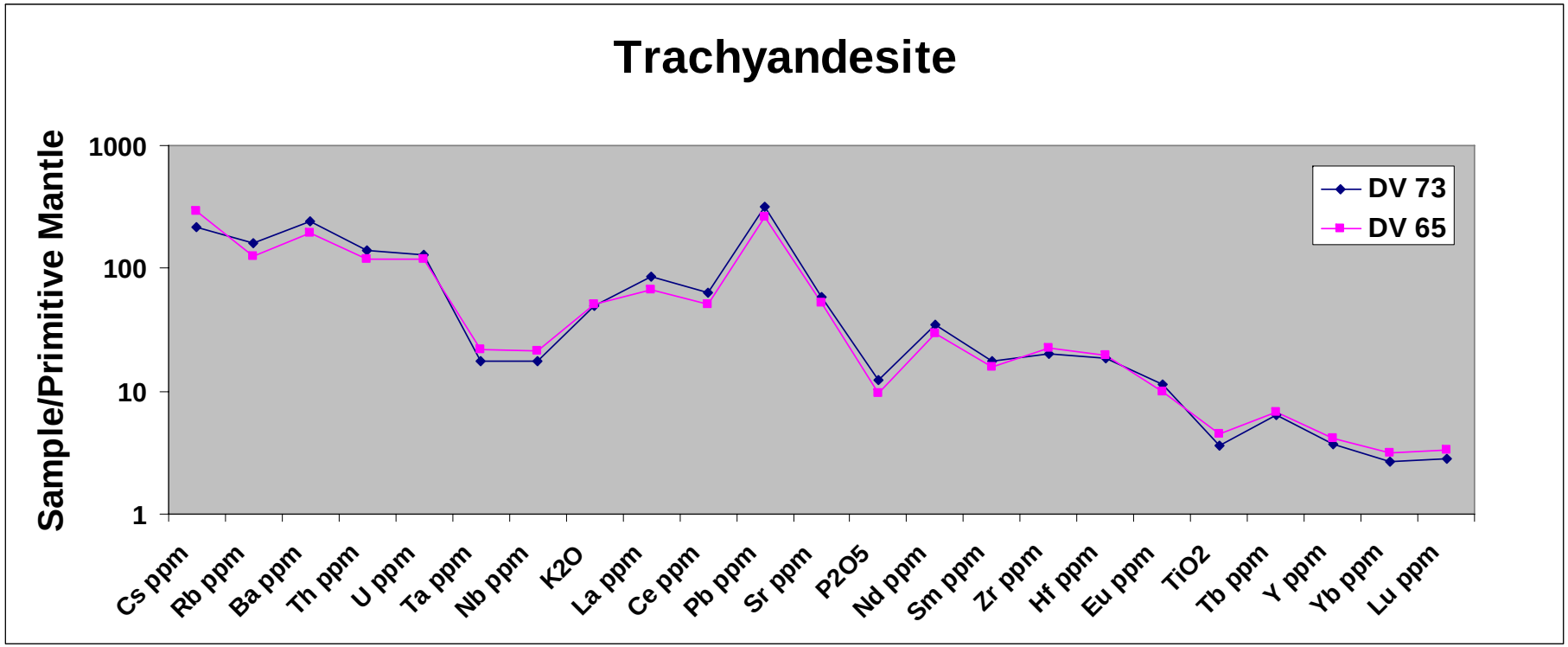

Figure 25a. Spider Diagram for all trachyandesite units in Ibex Pass.

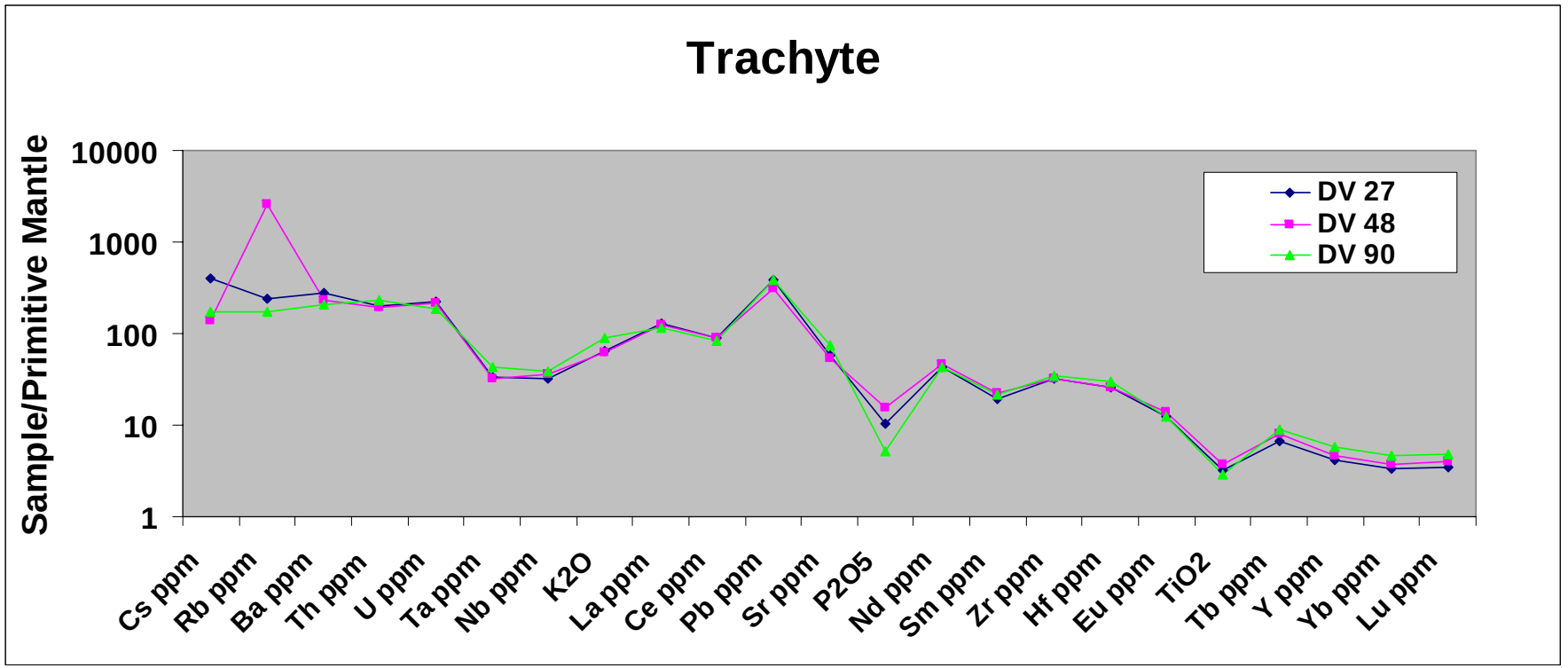

Figure 25b. Spider Diagram for all trachyte units in Ibex Pass.

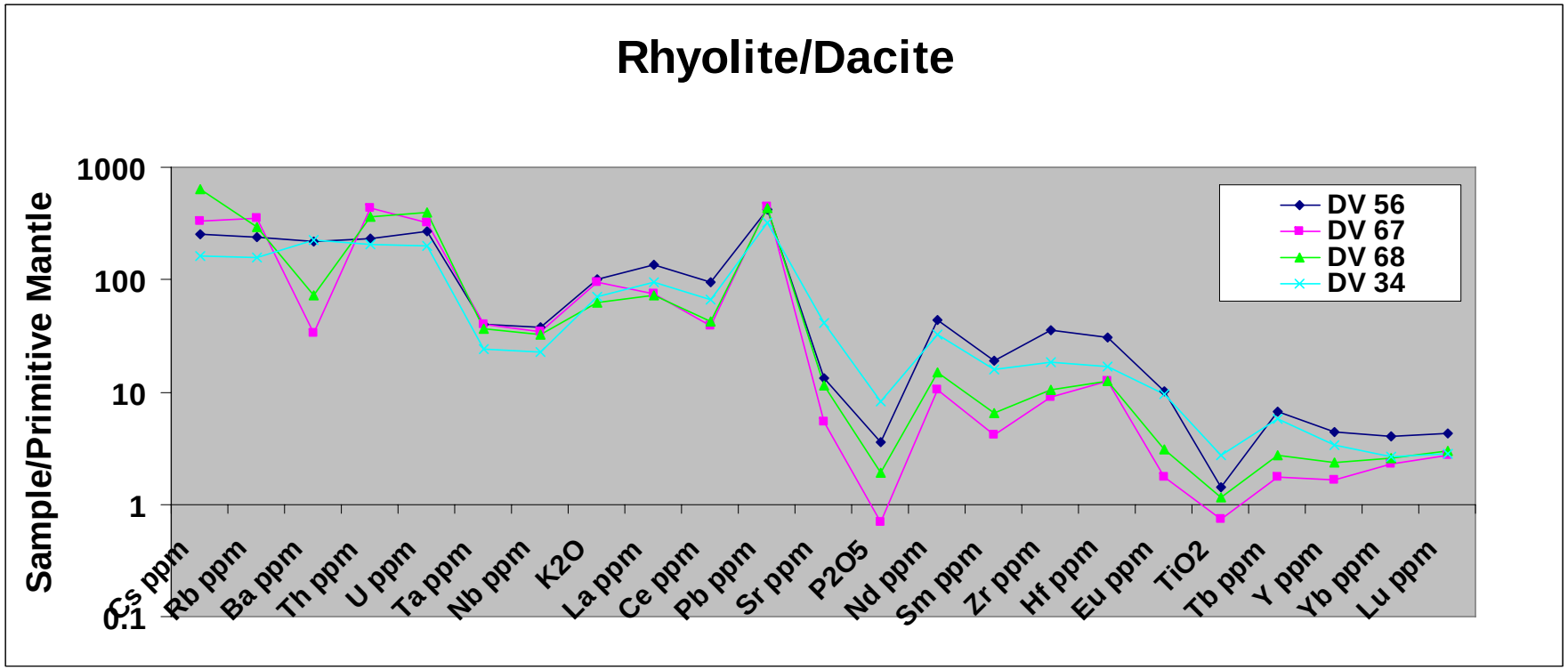

Figure 25c. Spider Diagram for all rhyolite/dacite units in Ibex Pass.

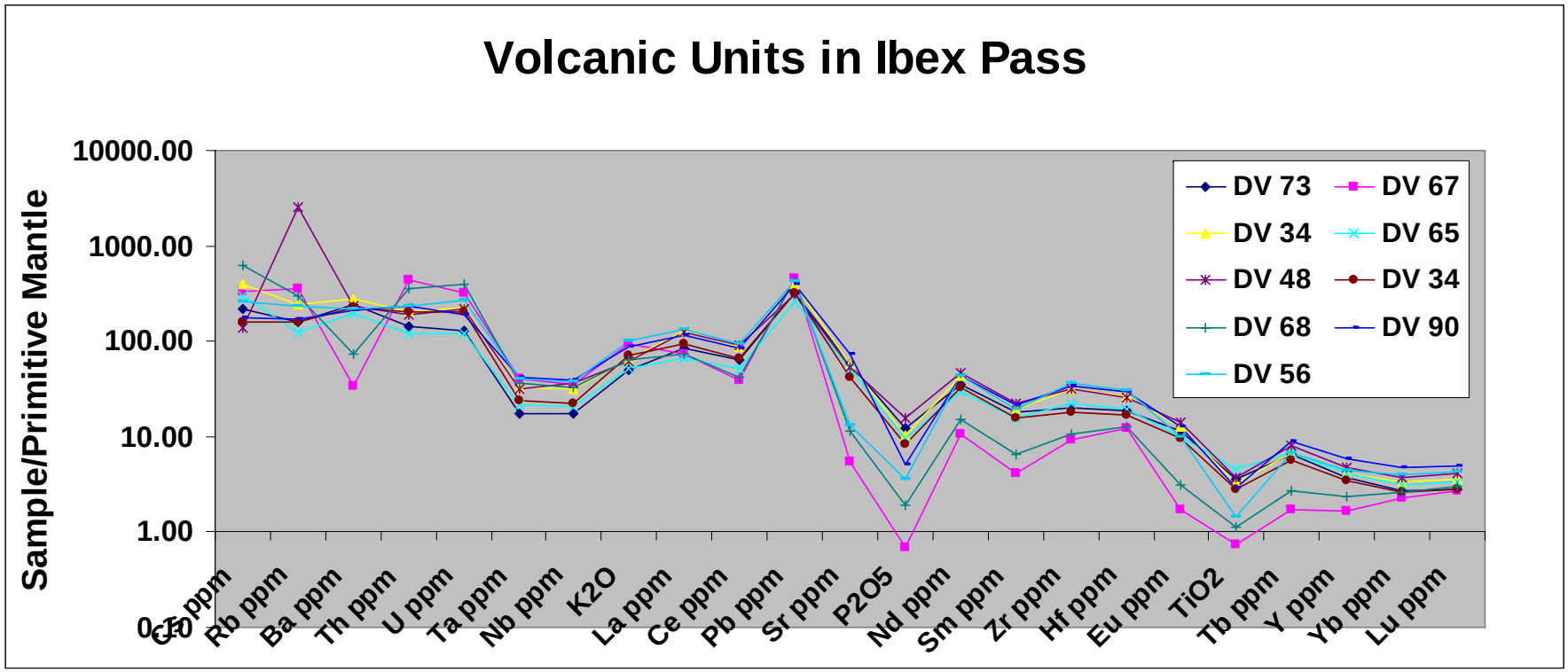

Figure 25d. Spider Diagram for all volcanic units in Ibex Pass.

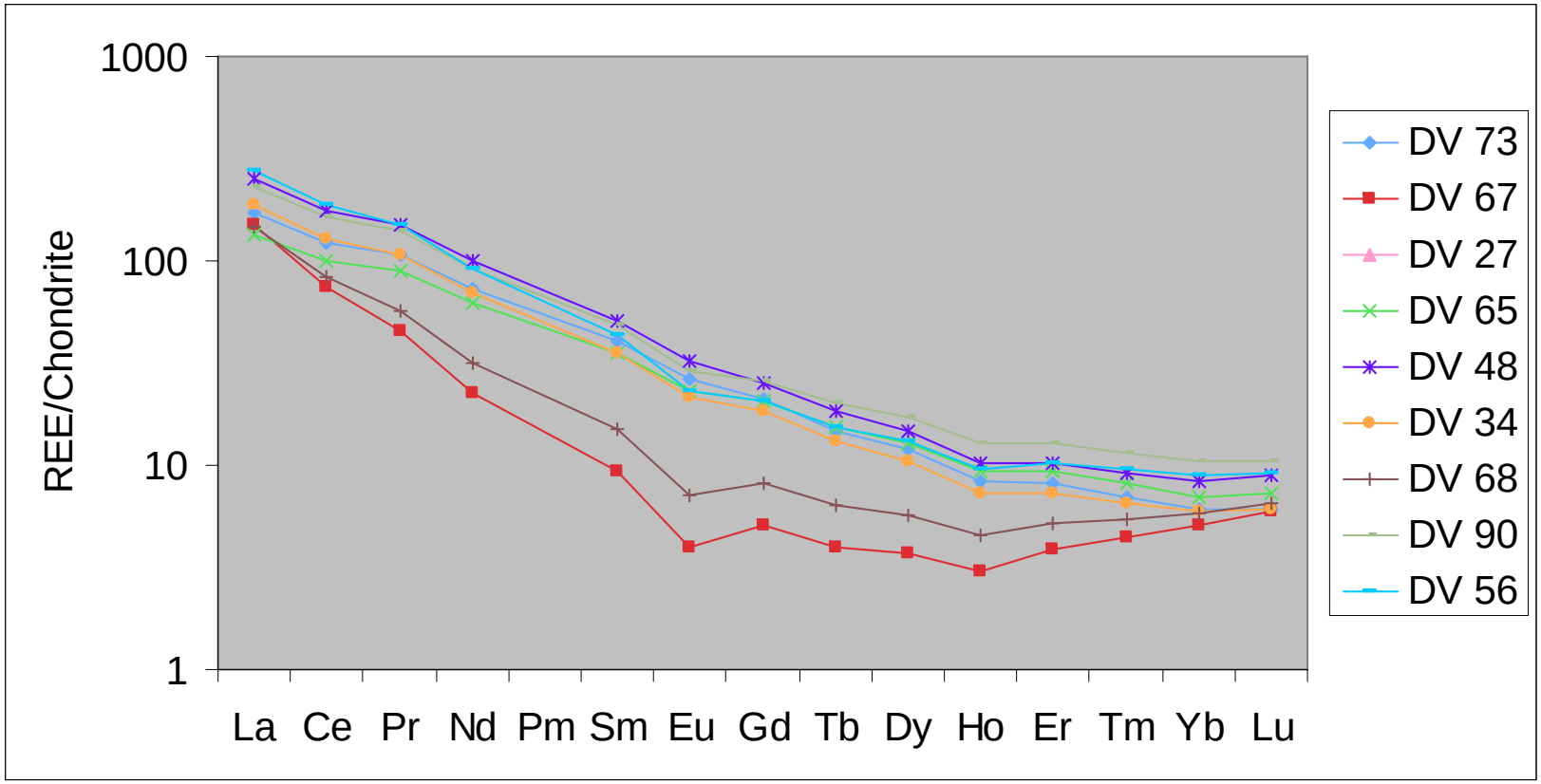

Figure 26. Rare Earth Element Diagram for all volcanic units in Ibex Pass.

6. DISCUSSION

6.1 Comparing Geochemistry

The geochemistry data provided by Yawn (1995) and Luckow et al. (2005) on volcanic assemblages in Wingate Wash provides the key data to compare with data from Ibex Pass. The samples analyzed from Yawn (1995) were selected because they were previously identified as being trachyandesite, trachyte, hyalite, and dacite in composition. The chosen samples analyzed by Luckow et al. (2005) for comparison with Ibex Pass units were from Eastern Owlshead Mountains and Wingate Wash. Geochemical data on upper, basaltic units from the North-Central Owlshead are not included in geochemical comparisons because they are lithologically different from units in Ibex Pass and are almost certainly part of a localized, distinctly younger volcanic pile. Similar data provided from Wright et al. (1991) also proved a valuable source in evaluating possible correlation with the Central Death Valley volcanic field. Geochemical data from the pre-Shoshone volcanics and Shoshone volcanics of the Central Death Valley volcanic field are used for correlation with Ibex Pass. The pre-Shoshone volcanics contains the Rhodes Tuff which is suspected to be a lithology in Ibex Pass.

In comparing geochemical data between the lithologies in Ibex Pass, the pre-Shoshone volcanics, and Shoshone volcanics it can be concluded that the Ibex Pass region does not contain rocks that correlate with the pre-Shoshone volcanics. The differences are shown on the TAS, Harker, variation, spider, and REE diagrams. There are geochemical similarities with the Shoshone volcanics, but they cannot be correlated because they do not appear to be time equivalent based on isotopic data. Field observations performed on tuff units in Ibex Pass, support that the tuff is not similar to the Rhodes tuff based on past descriptions made on the ~10Ma unit by Wright et al. (1991) and Topping (1993). The chemistry and field observations

performed on volcanic assemblages in Ibex Pass and Wingate Wash are, in contrast, very similar, implying an evolution from the same magmatic source. A TAS diagram (Figure 27) compares the chemical makeup of rock units in Ibex Pass, Wingate Wash, the pre-Shoshone volcanics, and the Shoshone volcanics. The TAS diagram displays a clear geochemical similarity between rocks in Wingate Wash and Ibex Pass. Two samples from the pre-Shoshone volcanics and four from the Shoshone volcanics are also displayed on the TAS diagram. The chemical make-up of the pre-Shoshone volcanics is distinctly different than the Ibex Pass volcanics. Trachytes and rhyolites are the majority of volcanic rocks sampled from Wingate Wash. There are also units of trachyandesite, basaltic trachyandesite, phonolite and tephri phonolite. The Ibex Pass units and the Wingate Wash volcanics plot in the same trachyandesite, trachyte, rhyolite, and dacite fields. The pre-Shoshone volcanics, in contrast, are more mafic in composition and plot in the basalt to basaltic andesite fields.

Two major concepts in igneous petrology are that in subduction environments calc-alkaline magmas are typically formed and akaline suites are generally associated with extensional regimes (Hooper, 1995). All sampled rocks from Ibex Pass and Wingate Wash formed during extension in Death Valley, and in line with that setting they contain alkalic magma suites (Figure 28). The Pre-Shoshone units are more enriched in alkalic magma because they are younger and formed when the Death Valley region was already going through extension. Wingate Wash and Ibex Pass units both plot in the high-K field and the pre-Shoshone volcanics are in the medium-K field (Figure 29).

When comparing the geochemistry plotted on the Harker diagrams (Figure 30-33) it is shown that the Ibex Pass units and volcanic assemblages from Wingate Wash seem to have evolved from the same magmatic source. On all Harker diagrams Ibex Pass and Wingate Wash

volcanic units overlap in composition and the Pre-Shoshone plot away from the comparable cluster. The evolution of the pre Shoshone volcanics is noticeably different and seems to follow a different fraction path. MgO vs. K2O and (Mg/Mg+Fe) vs. TiO2 diagrams show overlap in chemistry between Wingate Wash and Ibex Pass and noticible differences in the Pre-Shoshone volcanics (Figure 34a-34b).

The spider diagrams (Figure 35a-35c) contain data from different volcanic provinces throughout the world and from different regions in Death Valley. To demonstrate this similarity between the two localities Wingate Wash and Ibex Pass, volcanic units are compared to Pre-Shoshone, Shoshone, Big Bend, Pantellaria, and Suswa volcanics on these diagrams (Figure 35a-35c). The trachyte units from Wingate Wash and Ibex Pass are enriched and depleted similarly with very observable trends. The Ibex Pass and Wingate Wash units are lower in LREEs, illustrating less evolved volcanics than the comparable extensional produced trachytes.

Very distinct similarities are also found between the enrichment and depletion of rare earth elements from volcanics in Wingate Wash and Ibex Pass. (Figure 36a-36c) displays the data of rare earth elements abundances in trachyandesite, trachyte, and rhyolite/dacite units found in both volcanic fields. Of particular note is the absence of an Eu anomaly in Ibex Pass and Wingate Wash. When there is an Eu anomaly it means there was no fractionation of plagioclase feldspar from the magma because it requires Eu in the process (McBirney, 2007).

6.2 Comparing Physical Stratigraphy

The stratigraphy of a volcanic section exposed in the north-central Owlshead Mountains is similar in sequence and thickness to the measured volcanic section in Ibex Pass. The basal units of this section are characterized as flows interbedded with pyroclastic units (~130m thick), a white lithic tuff (17.6m thick), another series of flow units (~200m thick), and an overlying

section of basaltic flows (~450m thick) (Luckow et al., 2005). The volcanic section described here is very similar to the upper Wingate Wash section (Luckow et al., 2005). In Ibex Pass there is an upper mega breccia with clasts of granite (~100-150m thick), white lithic tuff (~10m thick), and a series of underlying pyroclastic volcanics (250-300m thick). The pyroclastic assemblage dominates in size in both field locations. The correlated stratigraphic section in Wingate Wash does not contain a mega breccia it has the tuff unlike noted in Ibex Pass. However, the mega breccia with clasts of granite is a landslide. Thus, since the units in Ibex Pass and Wingate Wash region are correlative it can be suggested to be part of the same volcanic package.

The stratigraphic relationships between the Ibex Pass volcanics and the east-central volcanics containing the Rhodes tuff, implies they are not from the same volcanic package. The Rhodes tuff overlies the Smith Mountain granite and Willow Spring pluton, and the tuff is capped by the Sheephead andesite. Based on sample descriptions of rock units in the east-central volcanic field there are no rocks in Ibex Pass that are litholgically similar. There is also a notable difference in the age of lithological units in Ibex Pass and the younger east-central volcanics.

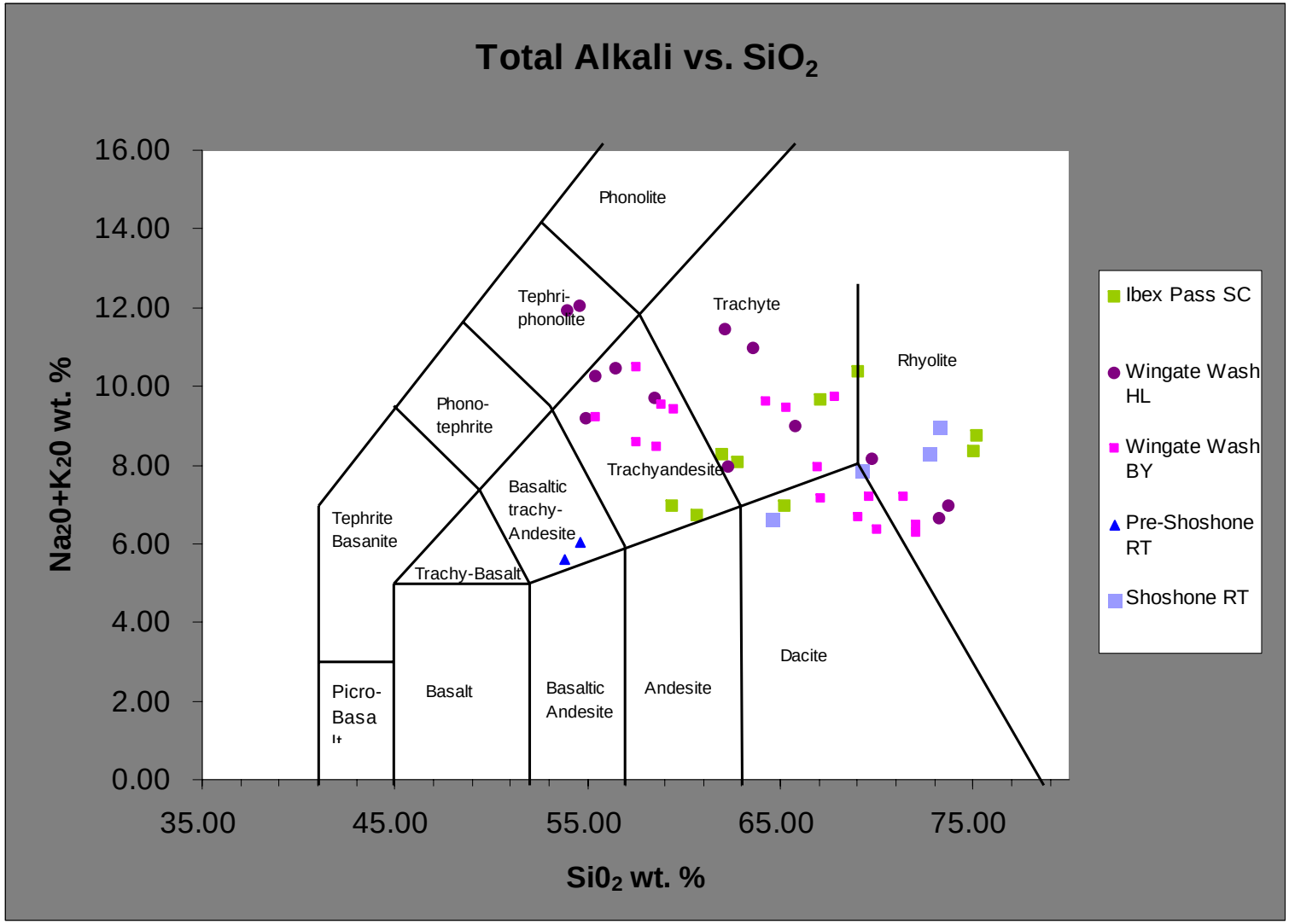

Figure 27. Total alkalis vs. silica for units in Wingate Wash, pre Shoshone volcanics, Shoshone volcanics, and Ibex Pass.

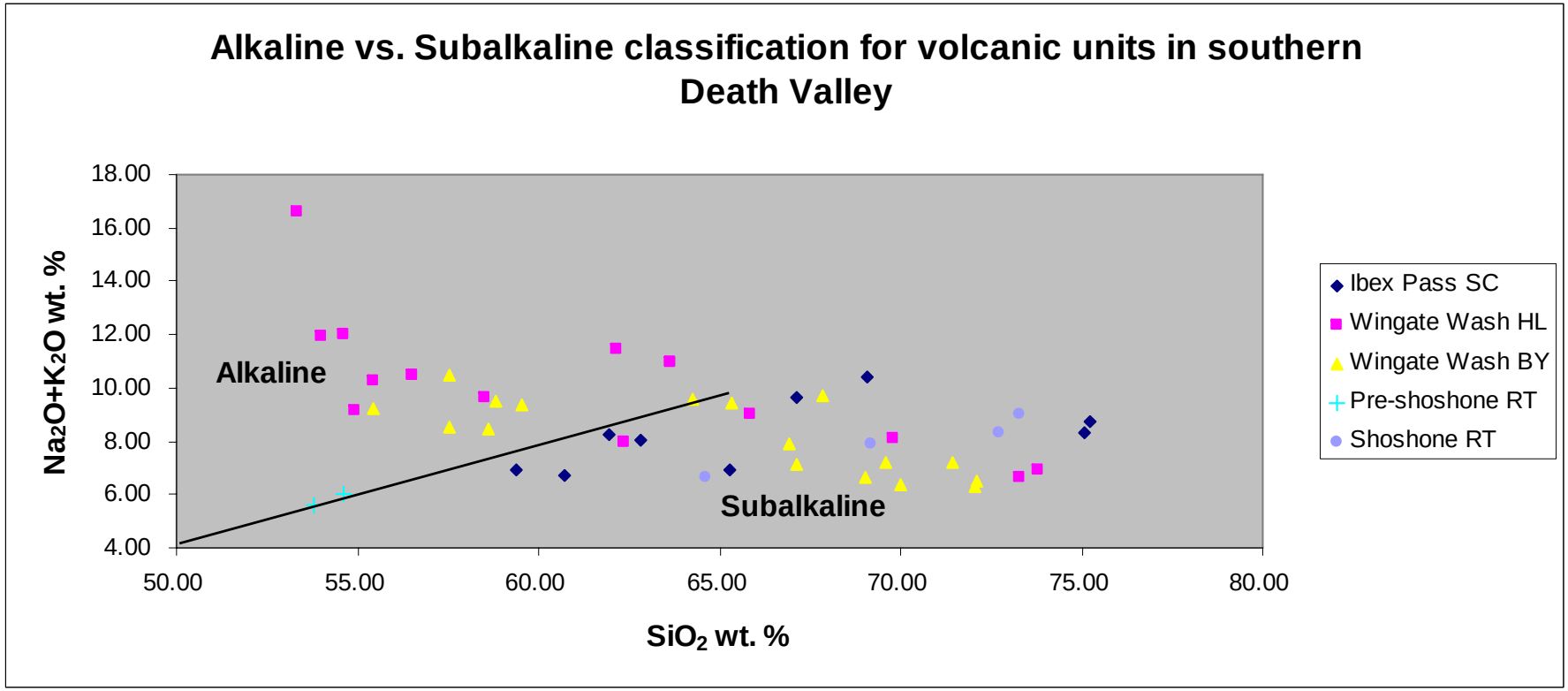

Figure 28. Alkaline vs. subalkaline classification for units in Wingate Wash, pre-Shoshone volcanics, Shoshone volcanics, and Ibex Pass (Irvine, Barager, 1971).

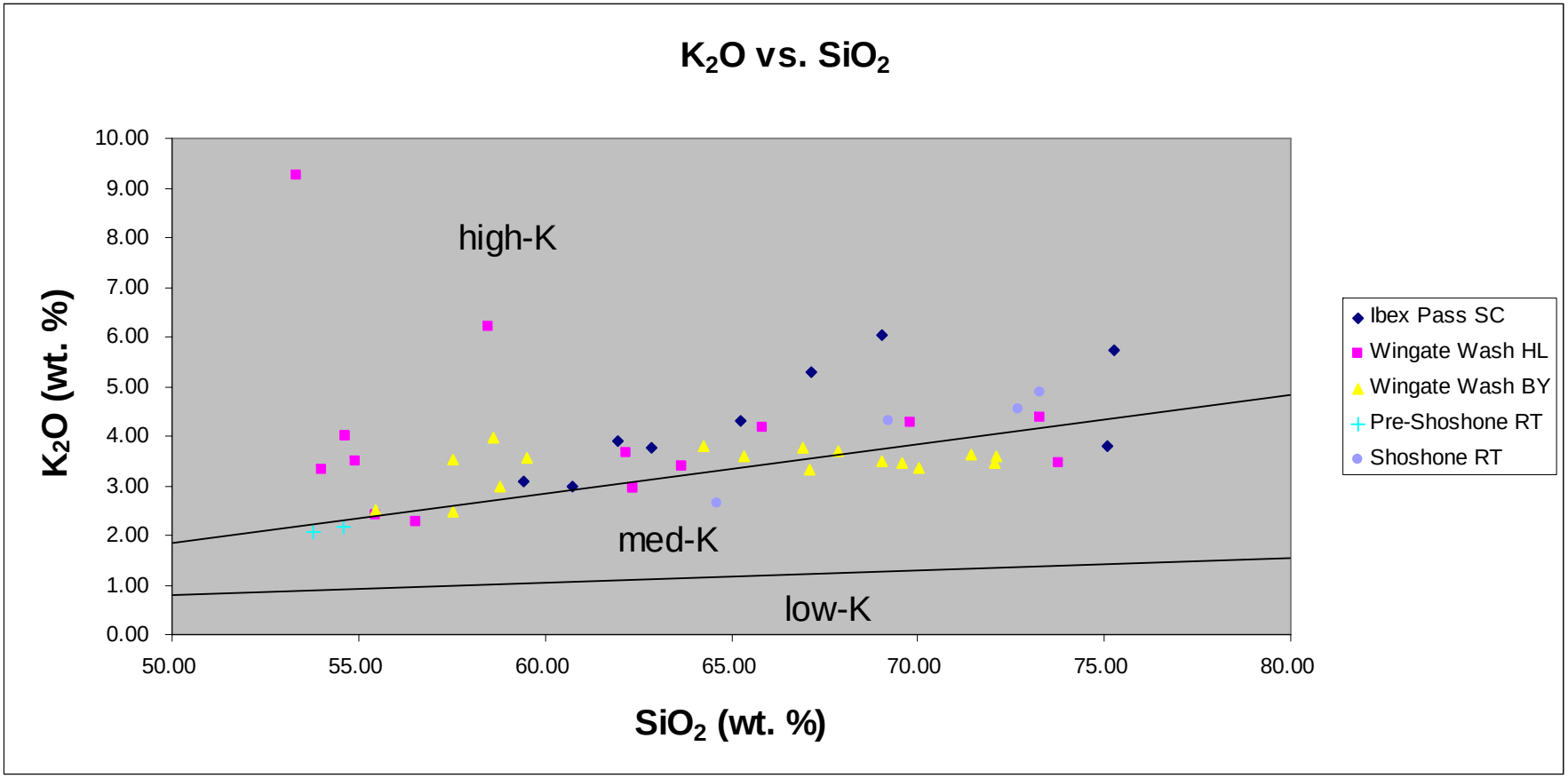

Figure 29. High, medium, and low-K fields for all units in Ibex Pass, Wingate Wash, pre-Shoshone volcanics, and Shoshone volcanics

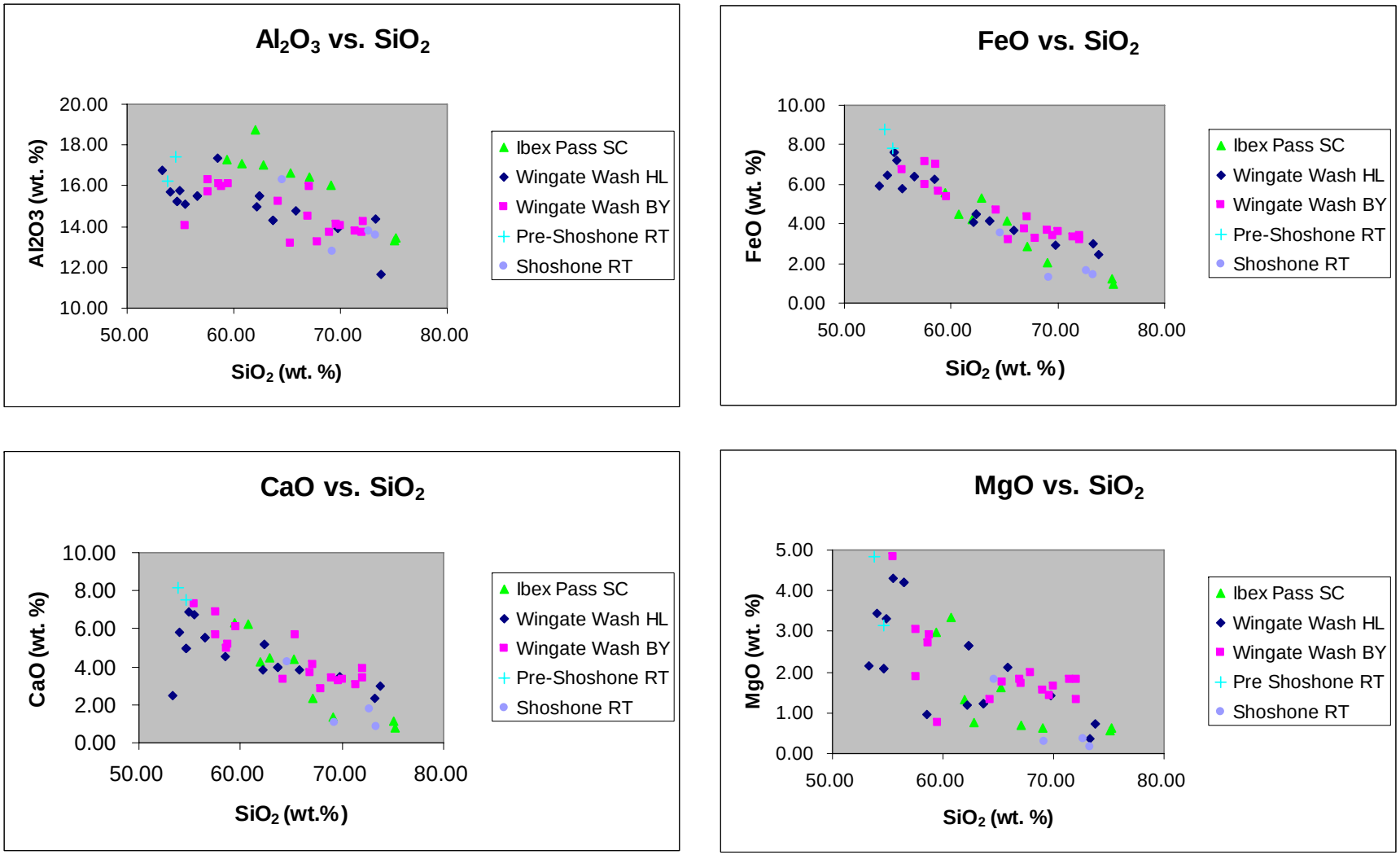

Figure 30. Major elements vs. silica for units in Ibex Pass, Wingate Wash, Pre-Shoshone volcanics, and Shoshone volcanics.

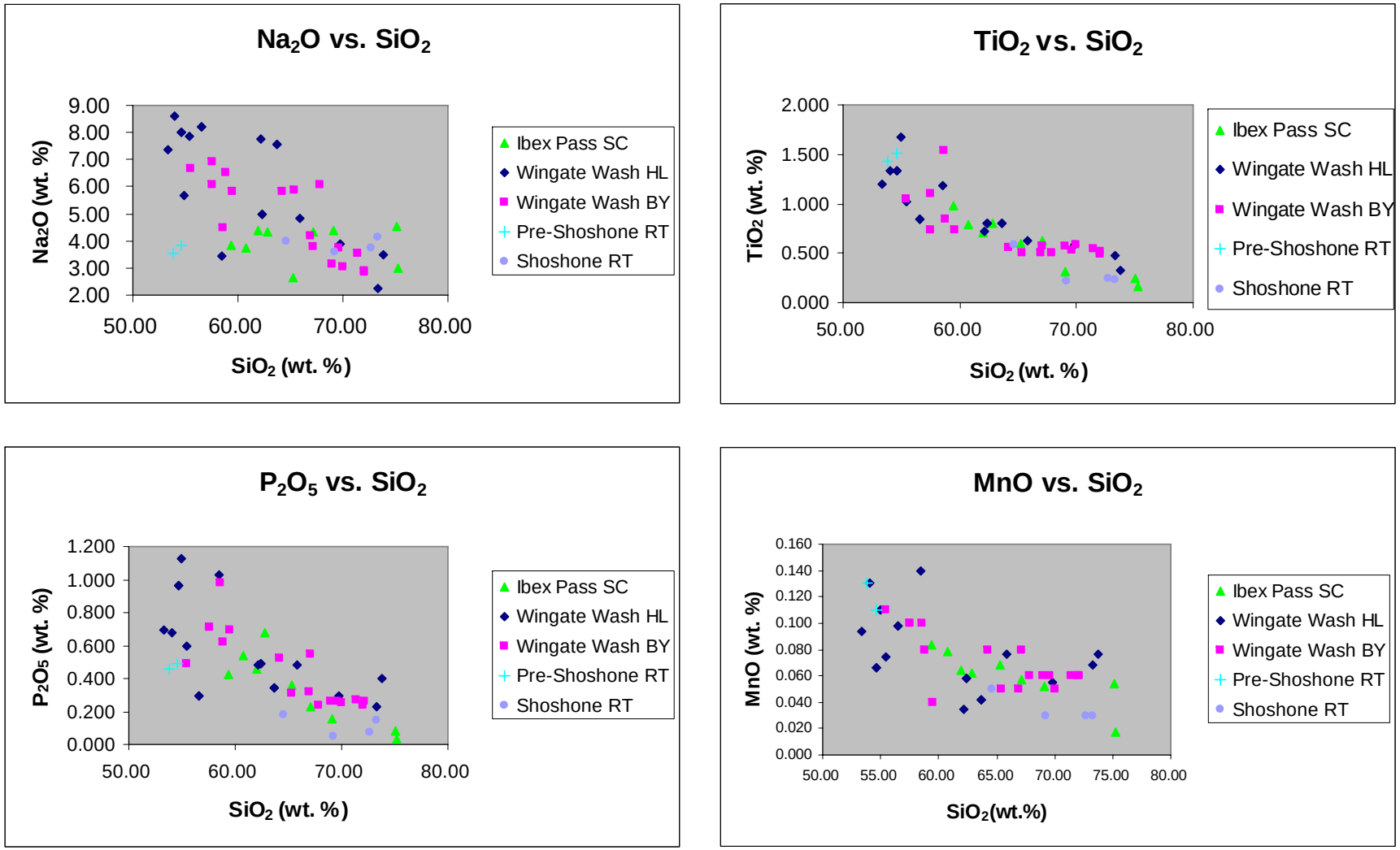

Figure 31. Major and minor elements vs. silica for units in Ibex Pass, Wingate Wash, Pre-Shoshone volcanics, and Shoshone volcanics..

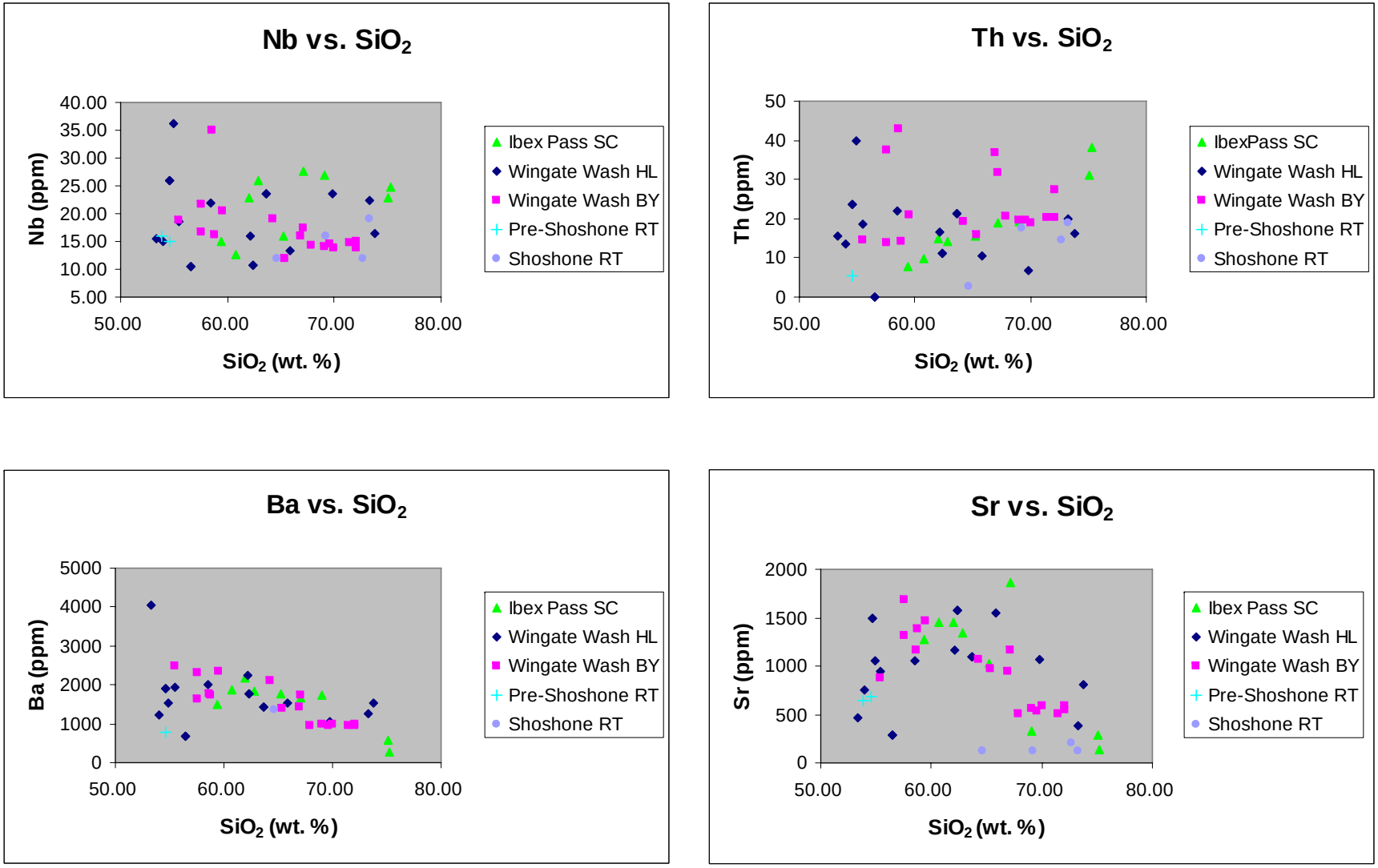

Figure 32. Trace elements vs. silica for units in Ibex Pass, Wingate Wash, pre-Shoshone volcanics, and Shoshone volcanics.

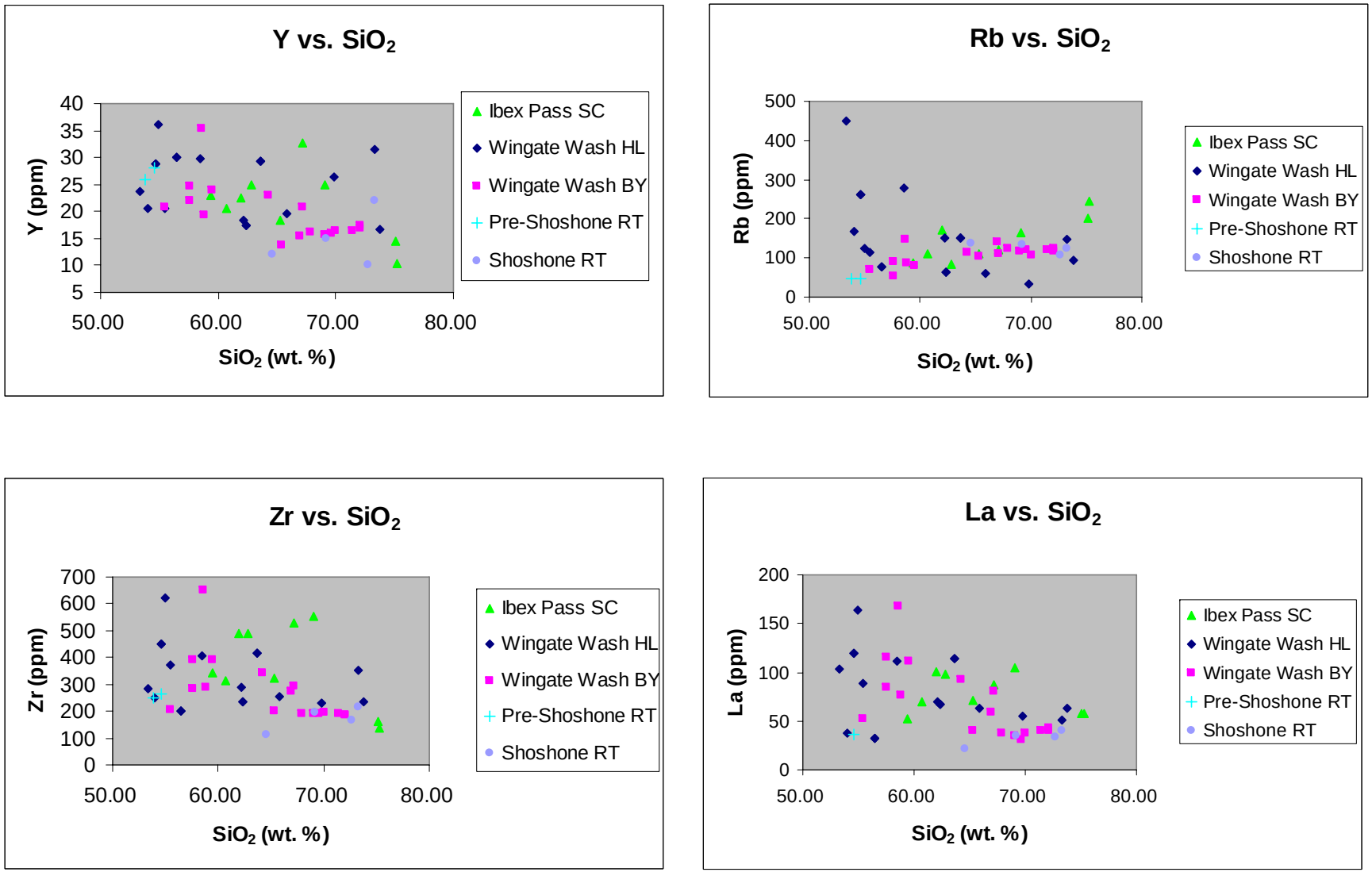

Figure 33. Trace elements vs. silica for units in Ibex Pass, Wingate Wash, pre-Shoshone volcanics, and Shoshone volcanics.

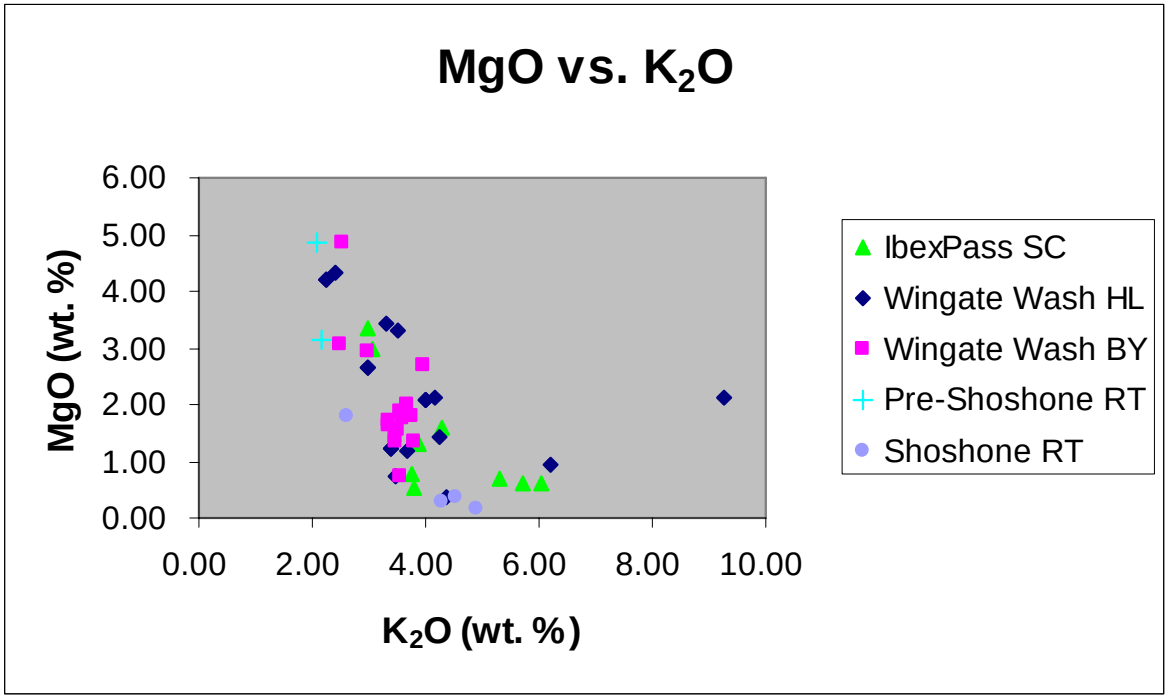

Figure 34a. K_2O vs. MgO for units in Ibex Pass, Wingate Wash, pre-Shoshone volcanics, and Shoshone volcanics.

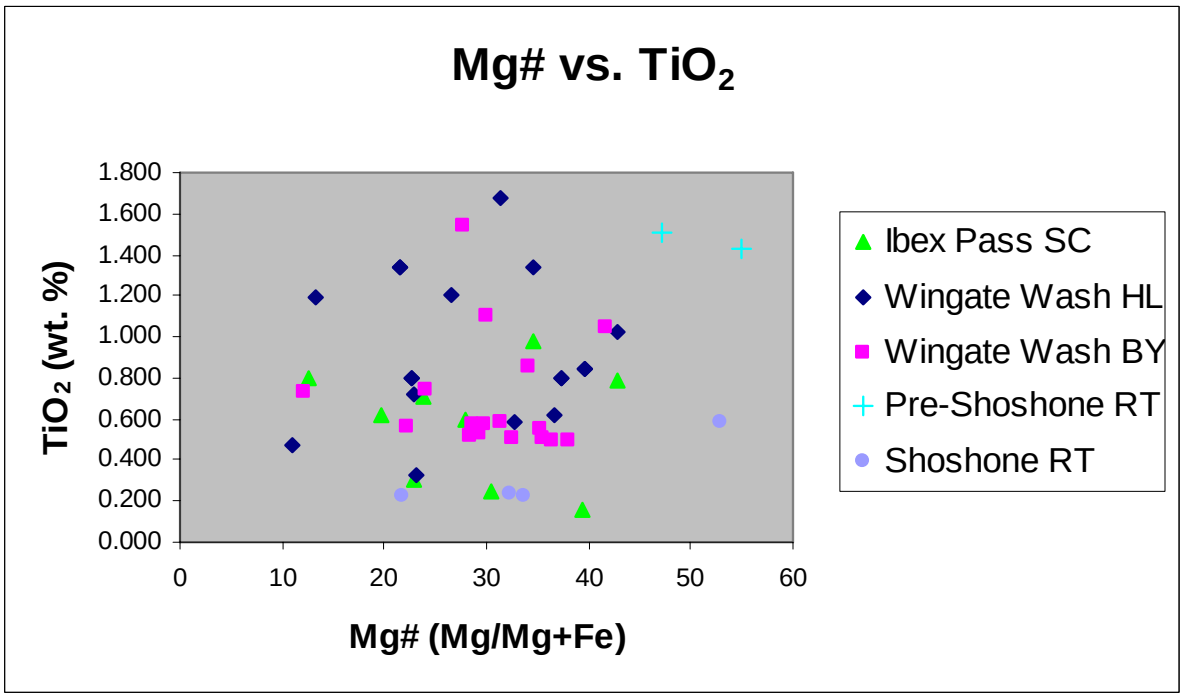

Figure 34b. Mg# vs. TiO2 for units in Ibex Pass, Wingate Wash, pre-Shoshone volcanics, and Shoshone volcanics.

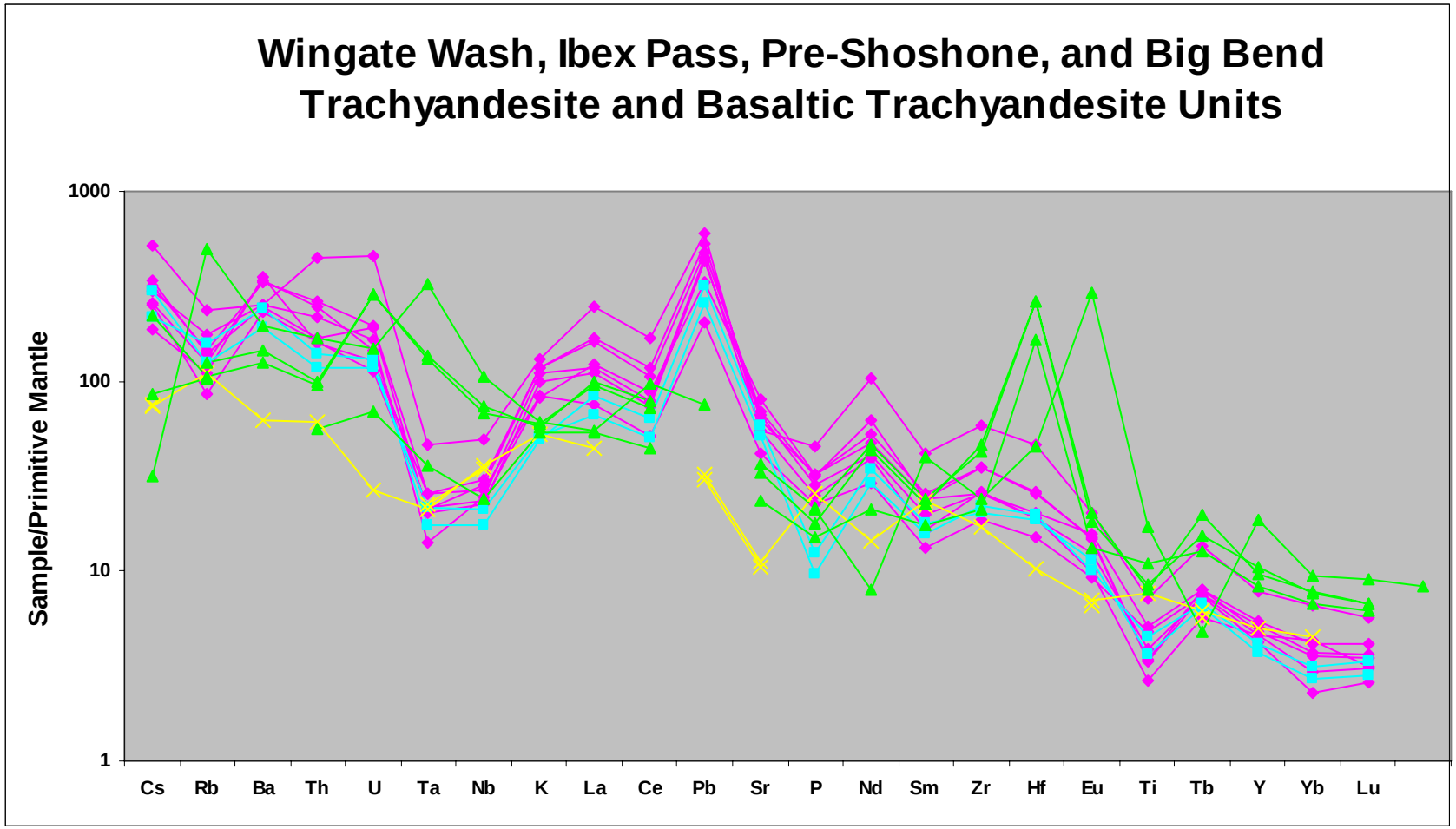

Figure 35a. Spider Diagram for trachyandesite units in Ibex Pass and Wingate Wash and basaltic trachyandesite units for the Pre-Shoshone volcanics. Symbols: pink diamond (Wingate Wash volcanics); blue square (Ibex Pass volcanics); yellow x (Pre-Shoshone volcanics); green triangle (Big Bend Volcanics).

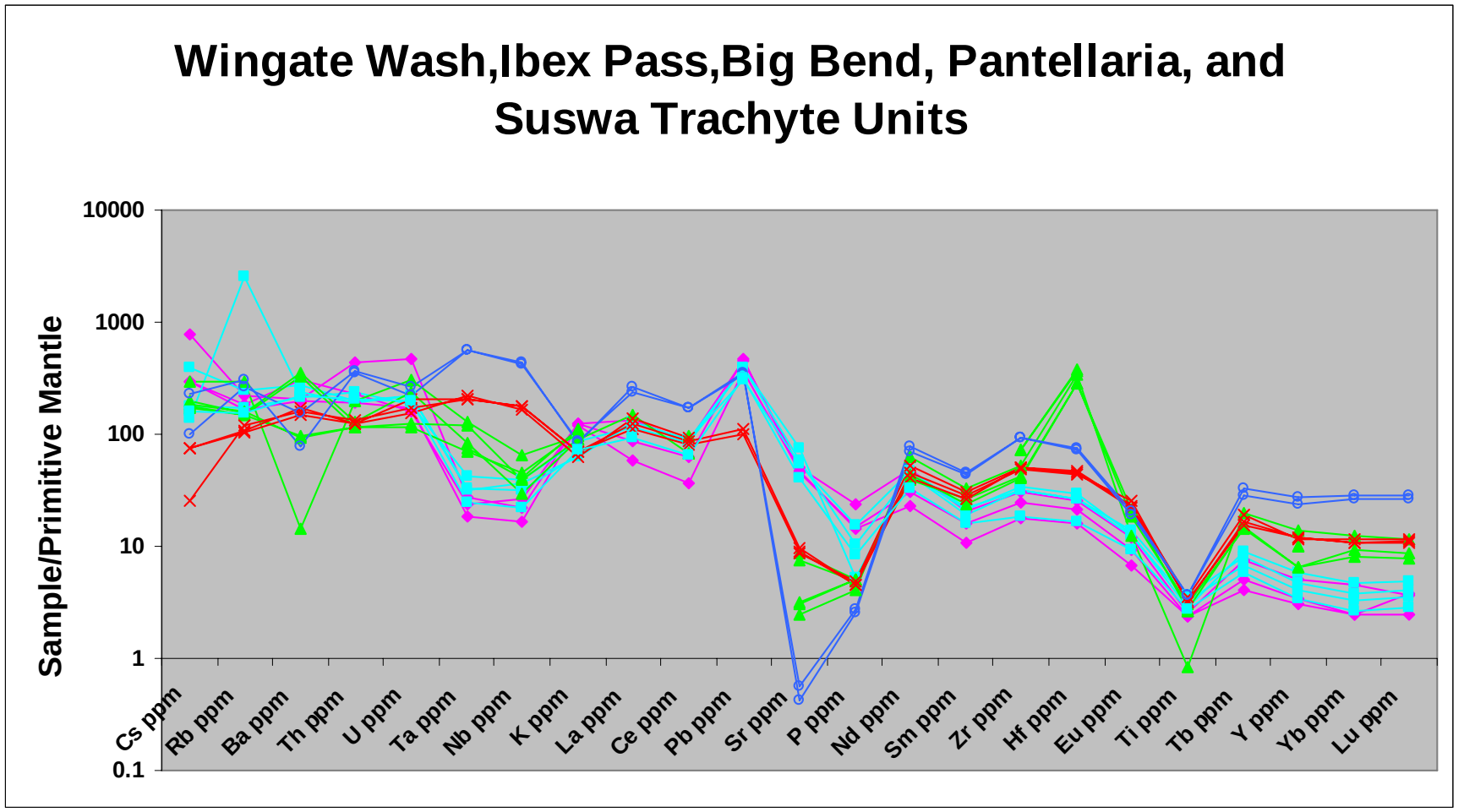

Figure 35b. Spider Diagram for trachyte units in Wingate Wash and Ibex Pass. Symbols: pink diamond (Wingate Wash volcanics); blue square (Ibex Pass volcanics); green triangle (Big Bend volcanics); red x (Pantellaria volcanics); dark blue circle (Suswa volcanics).

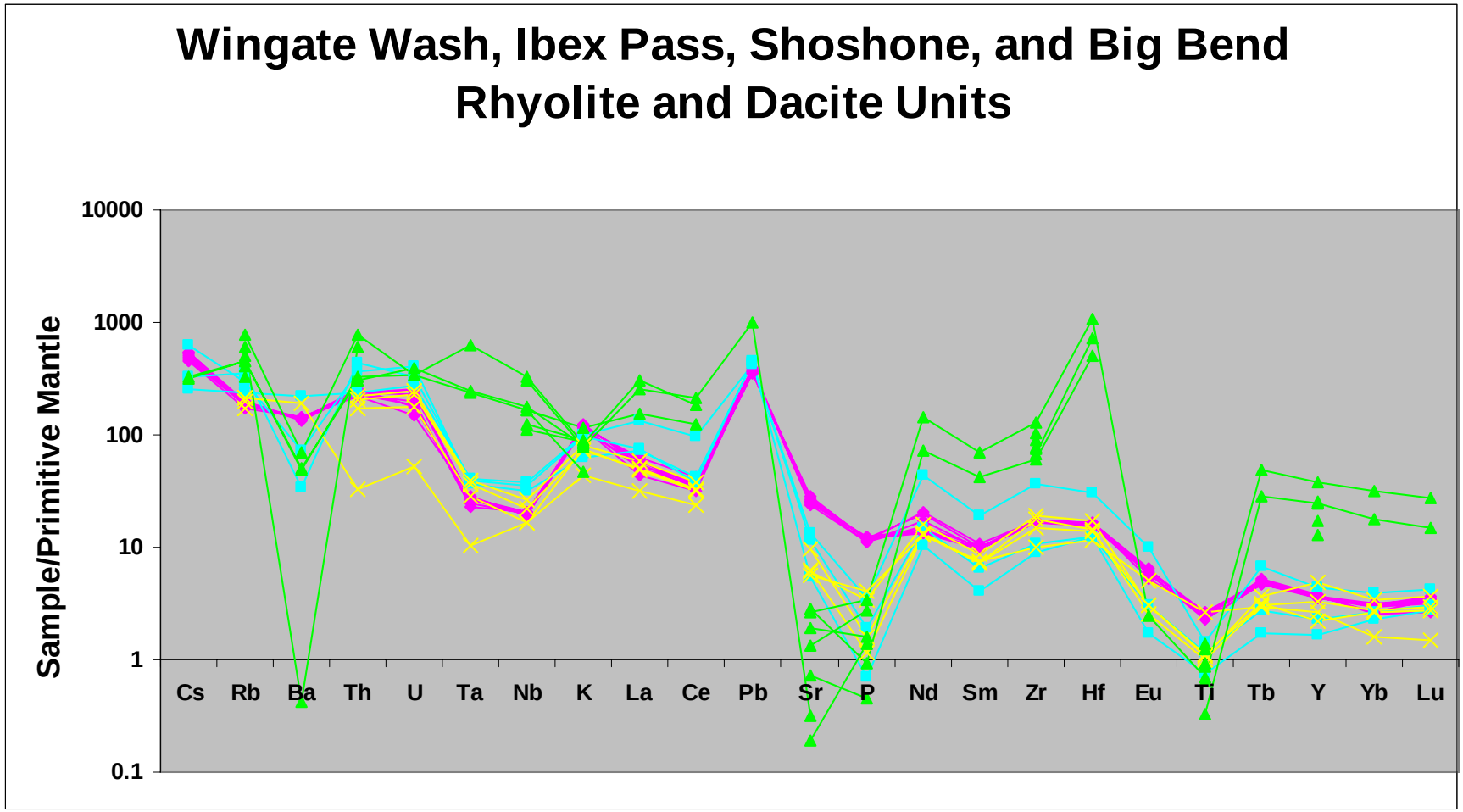

Figure 35c. Spider Diagram for rhyolite/dacite units in Wingate Wash, Ibex Pass and Shoshone Volcanics. Symbols: pink diamond (Wingate Wash volcanics); blue square (Ibex Pass volcanics); yellow x (Shoshone volcanics); green triangle (Big Bend volcanics).

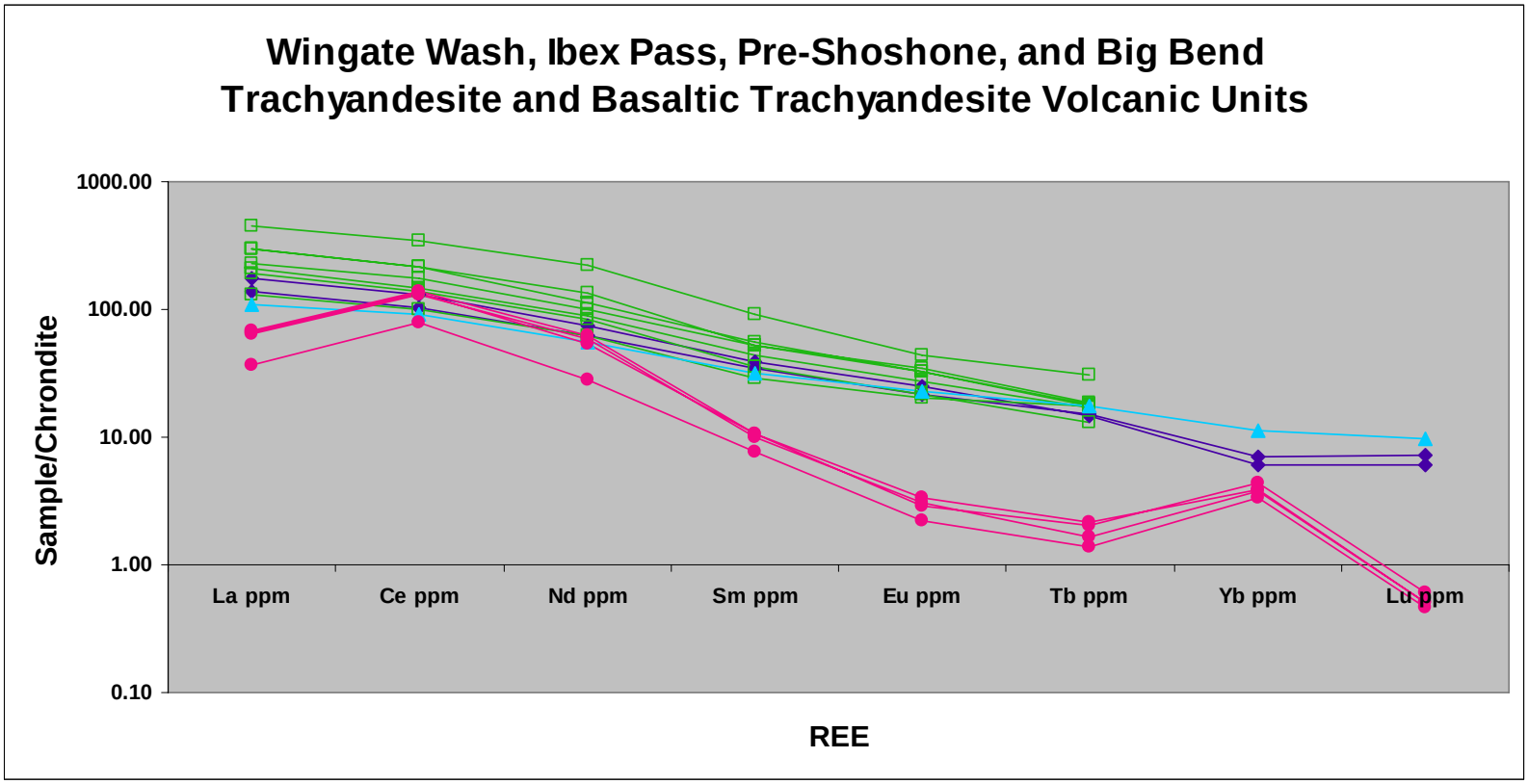

Figure 36a. Rare Earth Element diagram for trachyandesite units in Ibex Pass and Wingate Wash. Symbols: green closed squares (WingateWash volcanics); purple open diamonds (Ibex Pass volcanics); blue closed triangles (Pre-Shoshone volcanics); pink closed circles (Big Bend volcanics).

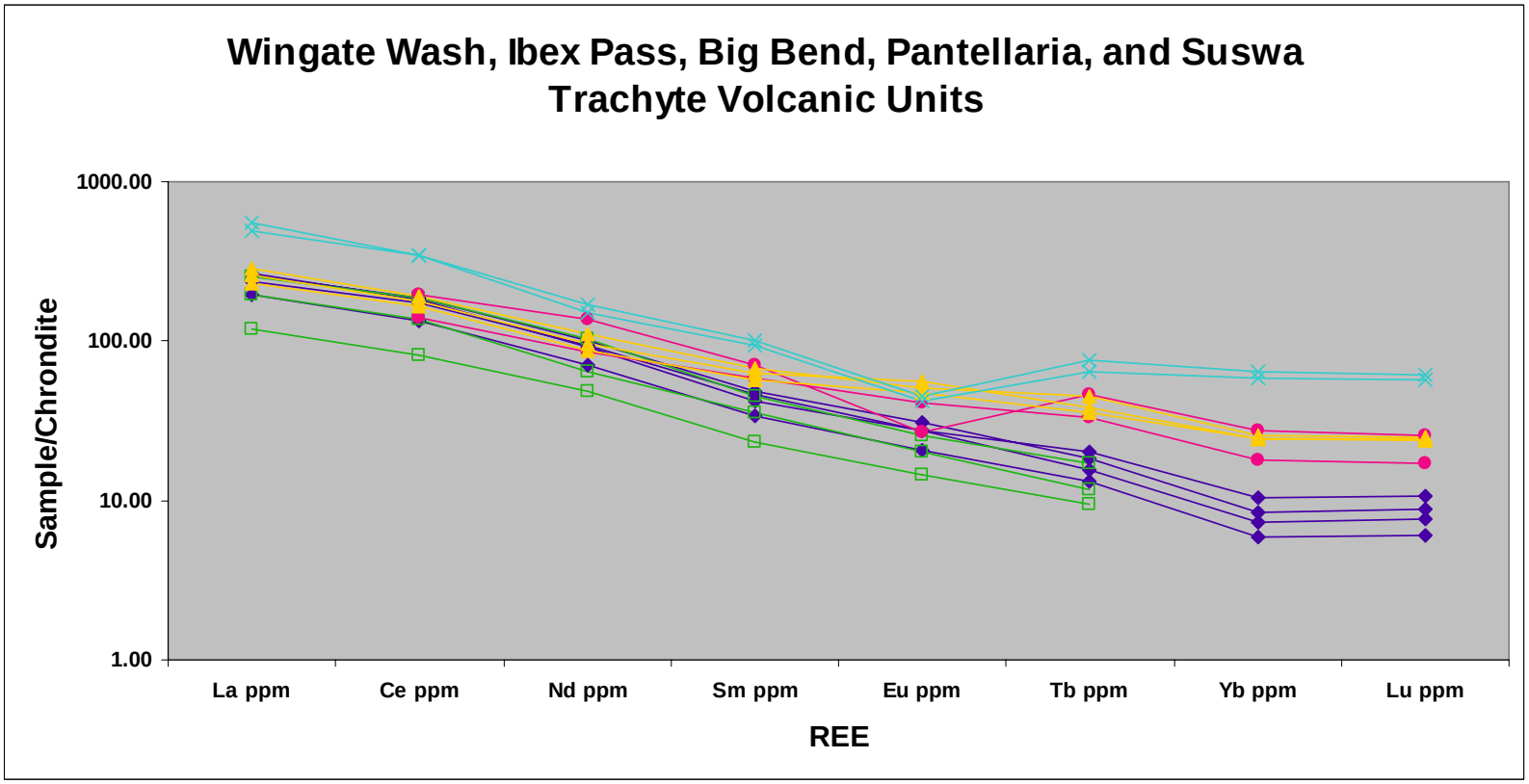

Figure 36b. Rare Earth Element diagram for trachyte units in Ibex Pass and Wingate Wash. Symbols: green closed squares (WingateWash volcanics); purple open diamonds (Ibex Pass volcanics); pink closed circles (Big Bend volcanics); orange closed triangles (Pantellaria volcanics); blue x (Suswa volcanics).

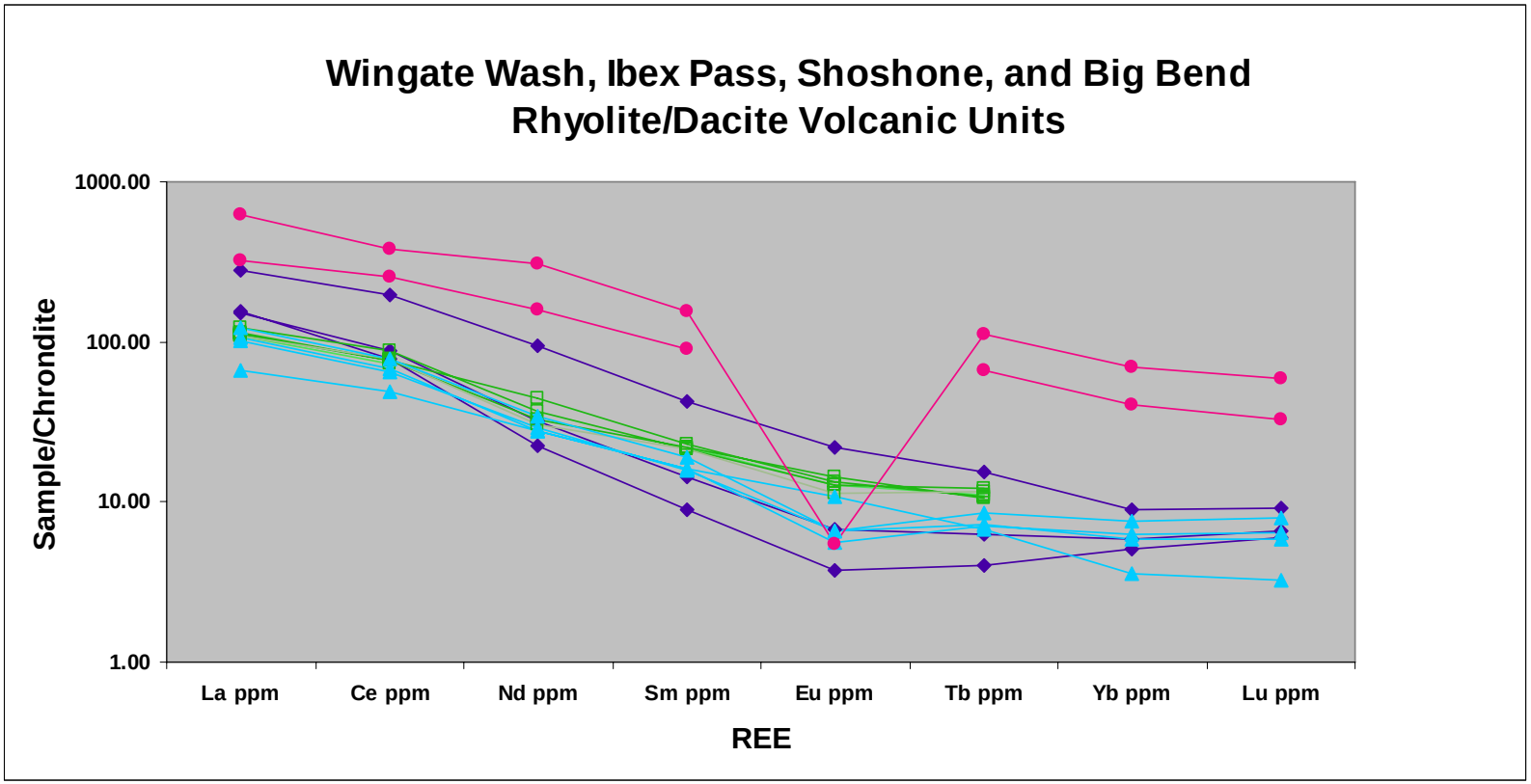

Figure 36c. Rare Earth Element diagram for rhyolite/dacite units in Ibex Pass and Wingate Wash. Symbols: green closed squares (WingateWash volcanics); purple open diamonds (Ibex Pass volcanics); blue closed triangles (Shoshone volcanics); pink closed circles (Big Bend volcanics

7. CONCLUSIONS

The southern Death Valley fault zone is a complex right lateral strike slip system. Field mapping and geochemical data on lithologic asemblages in the Ibex Pass volcanic field, provide a geologic reconstruction of the magmatic history of the area. In comparing data on the volcanics from Ibex Pass and Wingate Wash it can be determined they are stratigraphically and geochemically similar, suggesting they were once part of a continuous volcanic field was offset by the southern Death Valley fault zone. Reconstruction (Figure 37) of this volcanic field suggests ~25km to~35km of dextral offset. The differences in stratigraphic positions and geochemistry between the Pre-Shoshone volcanics and Ibex Pass can conclude the volcanics are not from the same magmatic assemblage.

Most of the rock units sampled in Ibex Pass indicate that crystal fractionation was the dominant process that created these diverse magmas. Due to the chemical constituents of volcanic units it can be implied they were produced during the onset of extension. The volcanics were derived from a mantle source; however whether it is asthenospheric or lithospheric needs to be determined through isotopic data.

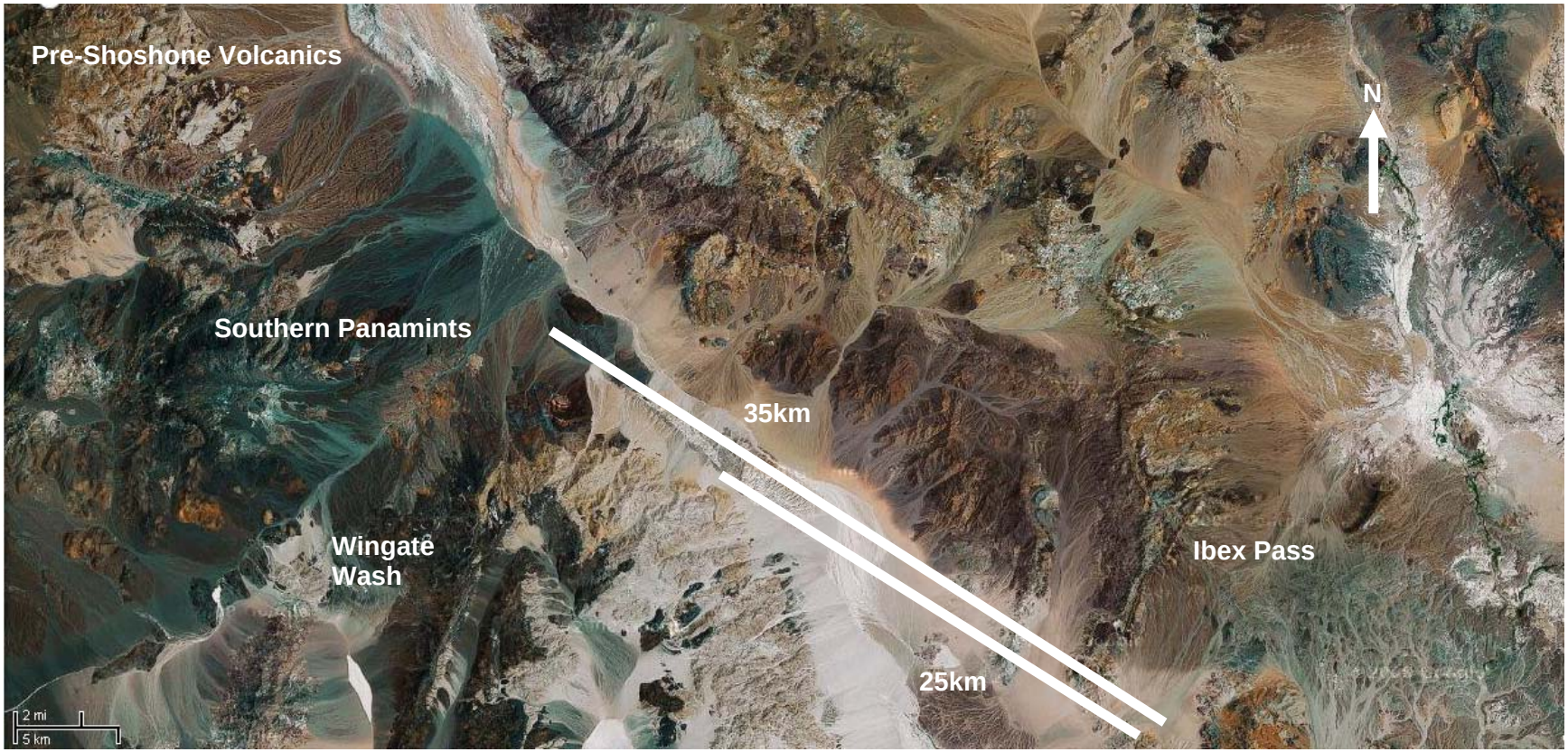

Figure 37. Reconstruction model of the Southern Death Valley Fault System.

REFERENCES

Blakely, R.J., Jachens, R.C., Calzia, J.P., Langenheim, V.E., 1999, Cenozoic basins of the Death Valley extended terrain as reflected in regional-scale gravity anomalies, in Wright, L.A., and Troxel, B.W., eds., Cenozoic basins of the Death Valley Region: Boulder, Colorado, Geological Society of America Special Paper 333.

Brady, R.H., 1986, Stratigraphy and Tectonics of the Northern Avawatz Mountains at the intersection of the Garlock and Death Valley fault zones, San Bernardino County, California-A Field Guide, Quaternary Tectonics of Southern Death Valley, p. 1-12.

Burchfiel,B.C., Stewart, J.H., 1966, "Pull apart" origin of the central segment of Death Valley, California: Geological of Society of America Bulletin, v. 77, p. 439-442.

Butler, P.R., 1988, Late Cenozoic history and styles of deformation along the southern Death Valley fault zone, California: Geological Society of America Bulletin, v. 100, p. 402-410.

Butler, P.R., 1989, Structural History of the Southern Death Valley Fault Zone (PhD Dissertation: Los Angeles, California, The University of Southern California.

Calzia, J.P., Ramo, O.T., 2000, Late Cenozoic crustal extension and magmatism, southern Death Valley region, California: Geological Society of America Field Guide 2, p. 135-164.

Davis, G.A., Burchfiel, B.C., 1973, Garlock Fault: An Intracontinental Transform Structure, Southern California, Geological Society of America Bulletin, v. 84, p. 1407-1422.

de Voogd, B., Serpa, L., Brown, L., Hauser, E., Kaufman, S., Oliver, J., Troxel, B.W., Willemin, J., Wright, L.A., 1986, Death Valley bright spot: A midcrustal magma body in the southern Great Basin, California?, Geology, v. 14, p. 64-67.

Dokka, R.K., Travis, C.J., 1990, Late Cenozoic strike-slip faulting in the Mojave desert, California. Tectonics v. 9, p. 311-340.

Frankel, K.L., Brantley, K.S., Dolan, J.F., Finkel, R.C., Klinger, R.E., Knott, J.R., Machette, M.N., Owen, L.A., Phillips, F.M., Slate, J.L., Wernicke, B.P., 2007, Cosmogenic 10Be and 36Cl geochronology of offset alluvial fans along the northern Death Valley fault zone: Implications for transient strain in the eastern California shear zone, 2007, Journal of Geophysical Research, v. 112, p. 1-18.

Friedmann, S.J., 1999, Sedimentology and stratigraphy of the Shadow Valley basin, eastern Mojave Desert, California: Geological Society of America Special Paper 333, p. 213-243.

Gan, W., Zhang, P., Shen, Z.K., Prescott, W.H., Svarc, J.L., 2003, Initiation of deformation of the eastern California Shear Zone: Constraints from Garlock fault geometry and GPS observations, Geophysical Research Letters, v. 30, n. 10, p. 1496.

Glazner, A.F., Walker, J.D., and Bartley, J.M., 2002a., Preface, in Glazner, A.F., Walker, J.D., and Bartley, J.M., eds., Geologic Evolution of the Mojave Desert and Southwestern Basin and Range: Boulder, Colorado, Geological of Society Memoir 195, p. v-vi.

Glazner,A.F., Walker, J.D., Bartley, J.M., Fletcher, J.M., 2002b., Cenozoic evolution of the Mojave block of southern California, in Glazener, A.F., Walker, J.D., and Bartlery, J.M., eds., Geologic Evolution of the Mojave Desert and Southwestern Basin and Range: Boulder, Colorado, Geological of Society Memoir 195, p.19-41.

Guest, B., Pavlis, T.L., Golding, H., Serpa, L., 2003, Chasing the Garlock: A study of tectonic response to vertical axis rotation, Geology, v. 31, p. 553-556.

Hamilton, W., Myers, W.B., 1966, Cenozoic tectonics of the western United States: Reviews of Geophysics, v. 4, p. 509-549.

Hill, M.L., Troxel, B.W., 1966, Tectonics of Death Valley Region, California, Geological Society of America Bulletin, v. 77, p. 435-438.

Holm, D.K., 1995, Relation of deformation and multiple intrusion in the Death Valley extended region, California, with implications for magma entrapment mechanism: Journal of Geophysical Research, v. 100, no. B7, p. 10495-10505.

Hooper, P.R., Bailey, D.G., and Holder, G.A.M., 1995, Tertiary calc-alkaline magmatism associated with lithospheric extension in the Pacific Northwest: Journal of Geophysical Research, v. 96, p. 10303-10319.

Le Maitre, R.W., 1989, A Classification of Igneous Rocks and Glossary of Terms: Blackwell, Oxford, p. 123-124.

Luckow, H.G., 2000, Syntectonic Volcanism and Sedimentation in a Transtensional Environment: Late Cenozoic Evolution of Wingate Wash, Death Valley (MS thesis): New Orleans, Louisiana, The University of New Orleans.

Luckow, H.G., Pavlis, T.L., Serpa, L.F., Guest, B., Wagner, D.L., Snee, L., Hensley, T.M., Kojenkov, A., 2005, Late Cenozoic sedimentation and volcanism during transtensional deformation in Wingate Wash and the Owlshead Mountains, Death Valley: Earth Science Reviews, v.73, p. 177-219.

Machette, M.N., Klinger, R.E., Knott, J.R., Wills, C.J., Bryant, W.A., and Rehis, M.C., 2001, A proposed nomenclature for the Death Valley fault system: in Machette, M.N., Johnson, M.L., and Slate, J.L., eds., Quaternary and Late Pliocene Geology of the Death Valley region: Recent observations on tectonics, stratigraphy, and lake cycles. Guidebook for the 2001 Pacific Cell-Friends of the Pleistocene Fieldtrip. United Stated Geological Survey Open File Report 01-51, p. J173-J183.

McBirney, A.R., 2007, Igneous Petrology Third Edition: Jones and Bartlett Publishers, Inc, p. 124-200.

McQuarrie, N., and Wernicke, B., 2005, An animated tectonic reconstruction of southwestern North America since 36 Ma: Geosphere, v. 1, no. 3, p. 147-172.

Monastero, F.C., Sabin, A.E., Walker, J.D., 1997, Evidence for post-early Miocene initiation of movement on the Garlock fault from offset on the Cudahy Camp Formation, east-central California: Geology, v. 25, no. 3, p. 247-250.

Miller, M.B., and Wright, L.A., 2004, Geology of the Death Valley National Park. Dubuque, IA: Kendall/Hunt Publishing Company, p. 38.

Nilsen, T.H., and Clarke, S.H. Jr., 1975, Sedimentation and tectonics in the early Tertiary continental borderland of central California: U.S. Geological Survey Professional Paper 925, p. 64.

Plescia, J.B., Henyey, T.L., 1982, Geophysical character of the proposed eastern extension of the Garlock fault and adjacent areas, eastern California: Geology, v. 10, p. 209-214.

Reed, S.J.B., 2005, Electron Microprobe Analysis and Scanning Electron Microscopy in Geology: United Kingdom, Cambridge University Press, p. 1.

Serpa, L., de Voogd, B., Wright, L., Willemin, J., Oliver, J., Hauser, E., and Troxel, B., 1988, Structure of central Death Valley pull-apart basin and vicinity from COCORP profiles in the southern Great Basin: Geological Society of America Bulletin, v. 176, p. 1437-1450.

Serpa, L., Pavlis, T.L., 1996, Three-dimensional model of the Cenozoic history of the Death Valley region, southeastern California, Tectonics, v. 15, n. 6, p. 1113-1128.

Shaw, D.M., 2006, Trace Elements in Magma: Printed in the United Kingdom at the University Press, p. 124.

Snow, J.K., and Wernicke, B., 2000, Cenozoic tectonism in the central Basin and Range: Magnitude, rate, and distribution of upper crustal strain: American Journal of Science, v. 300, p. 659-719.

Stewart, J.H., 1967, Possible large right-lateral displacement along fault and shear zones in Death Valley-Las Vegas area, California and Nevada: Geological Society of America Bulletin, v. 78, p. 131-142.

Stewart, J.H., 1983, Extensional tectonics in the Death Valley area, California: Transport of the Panamint Range structural block 80 km northwestward, Geology, v. 11, p. 153-157.

Troxel, B.W., and Calzia, J.P., 1994, Geology of the middle Miocene Ibex Pass volcanic field, southern Death Valley, California: Geological Society of America Abstracts with Program, v. 26, p. 99.

Topping, D.J., 1993, Paleogeographic reconstruction of the Death Valley extended region: Evidence from Miocene large rock-avalanche deposits in the Amargosa Chaos Basin, California, Geological Society of America Bulletin, v. 105, p. 1190-1213.

Vaniman, D., 2006, Tuff Mineralogy: Geological Society of America Special Paper 408, p. 11-15.

Wernicke, B.P., 1988, Magnitude and timing of extreme continental extension, the central Death Valley region, California. Abstracts with Programs, Geological Society of America 29, 381.

Winter, J.D., 2001, An Introduction to Igneous and Metamorphic Petrology: Upper Saddle River N.J., Prentice-Hall Inc., p. 136.

Wright, L.A., Troxel, B.W., 1967, Limitations on right-lateral strike-slip displacements, Death Valley and Furnace Creek fault zones, California: Geological Society of America Bulletin, v. 78, p. 933-950.

Wright, L.A., Troxel, B.W., 1970, Summary of Regional Evidence for right-lateral displacement in the Western Great Basin: Discussion: Geological Society of America Bulletin, v. 81, p.2167-2174.

Wright, L.A., and Troxel, B.W., 1973, Shallow-Fault Interpretation of Basin and Range structure, Southwestern Great Basin, Gravity and tectonics, John Wiley and Sons, New York, p. 397-407.

Wright, L.A., Otton, J.K., Troxel, B.W., 1974, Turtleback surfaces of Death Valley viewed as phenomena of extensional tectonic: Geology, v. 2, p. 53-54.

Wright, L.A., Pavlis, T.L., Ellis, M.A., Thompson, R.A., DeWitt, E.H., Miller, M.G., Troxel, B.W., Otton, J.K., Serpa, L.F., 1991, Cenozoic Magmatic and Tectonic Evolution of the East-Central Death Valley Region, California, Guidebook for the 1991 Annual Meeting, Geological Society of America.

Yawn, B. 1995, Volcanic Stratigraphy and Petrogenesis of the Wingate Wash Area, (MS thesis): New Orleans, Louisiana, The University of New Orleans.

APPENDIX A

Field descriptions and optical observations are made for all twenty-eight thin sections studied. There are two photos that follow the description of each thin section. One is a petrographic view under plane polarized light (PPL) and the other photograph is under crossed polar light.

Thin Section Number: DV24
Digenetic Facies Type: TRACHYTE
Field Observations: Light grey rhyolite. Rock is very altered and weathered.
Optical Notes: * Alkali Feldspar (some clustered up) *Trickitic texture *Oxides *Big phenocrysts of amphibole *Small amounts of clinopyroxene *Glassy groundmass *Perlitic cracks *Plagioclase *Appears to be a very altered feldspar.

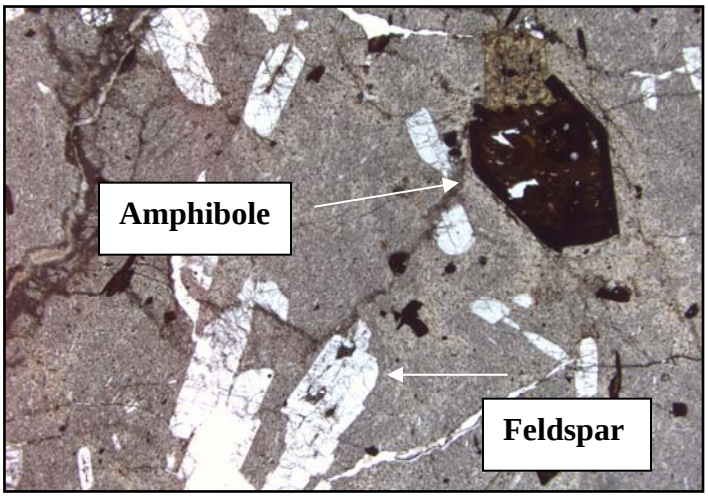

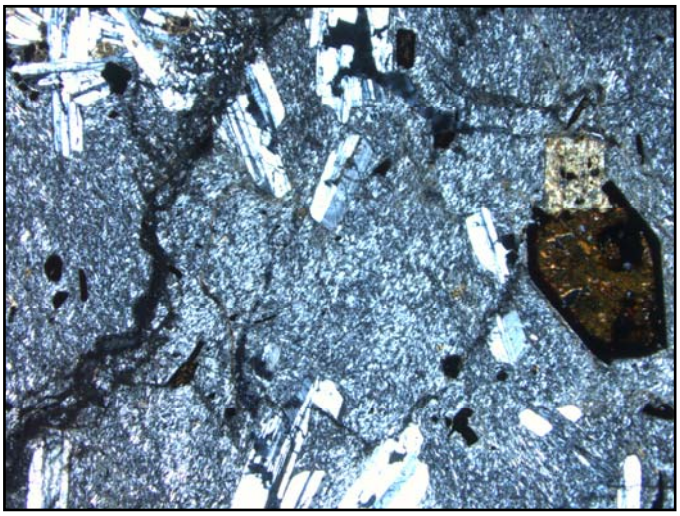

Thin Section Number: DV47
Diagenetic Facies Type: TRACHYTE
Field Observations: In contact with andesitic unit. Fault well exposed.
Optical Notes: * Alkali Feldspar *Fined grained texture/ground mass *Quartz veins * Oxides *Well altered *Small crystals of CPX *Trickitic texture

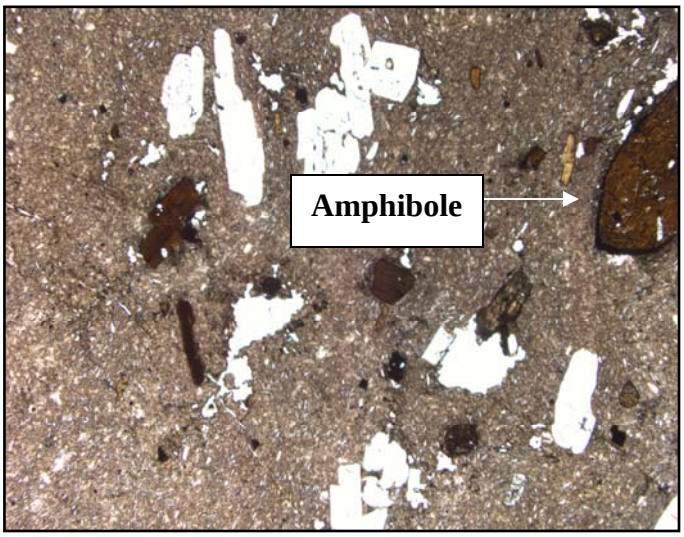

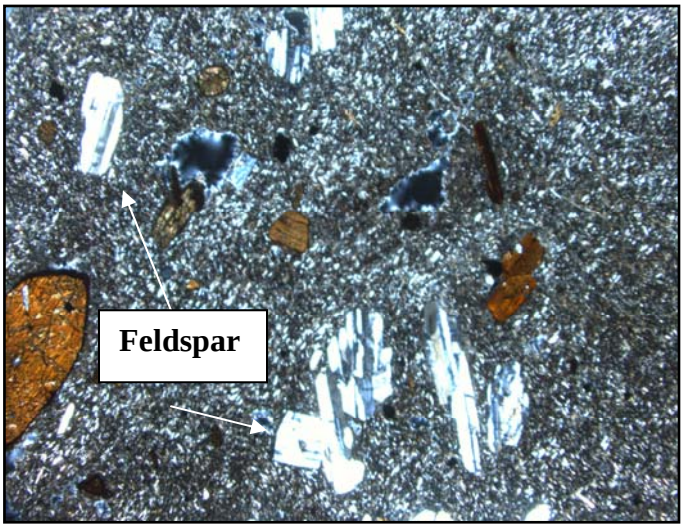

Thin Section Number: DV74
Diagenetic Facies Type: TUFF
Field Observations: Very lithic white tuff
Optical Notes: Sanidine and Quartz. Glass present

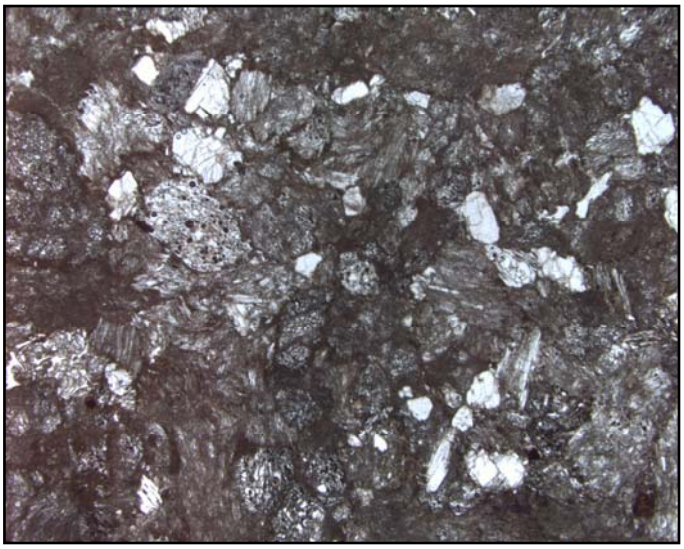

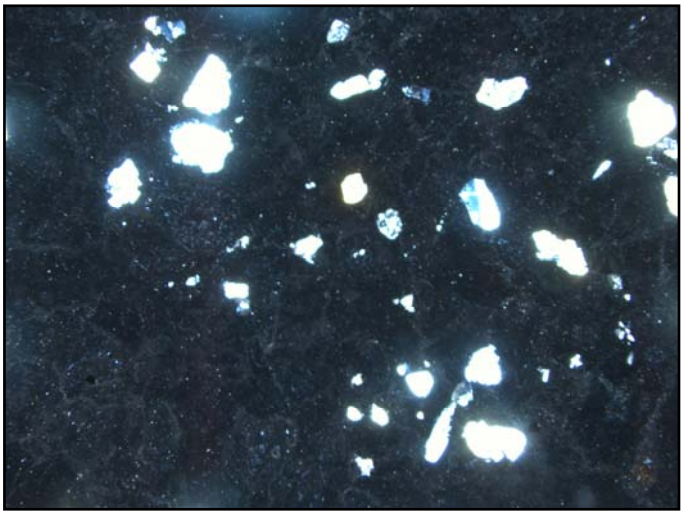

Thin Section Number: DV27
Diagenetic Facies Type: TRACHYTE
Field Observations: Amphibole rich volcanic rock. Flow unit appears to be in contact with andesite.
Optical Notes: *Glass *Alkali feldspar (abundant)/randomly oriented *Hornblende *Trickitic texture *Oxides *Small amount of CPX

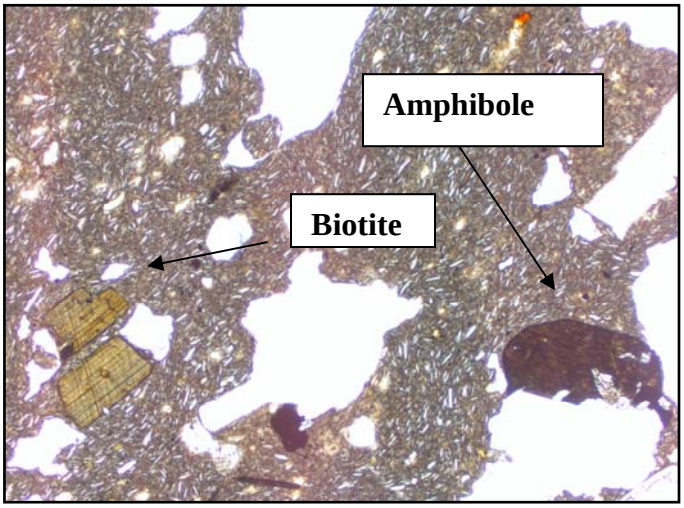

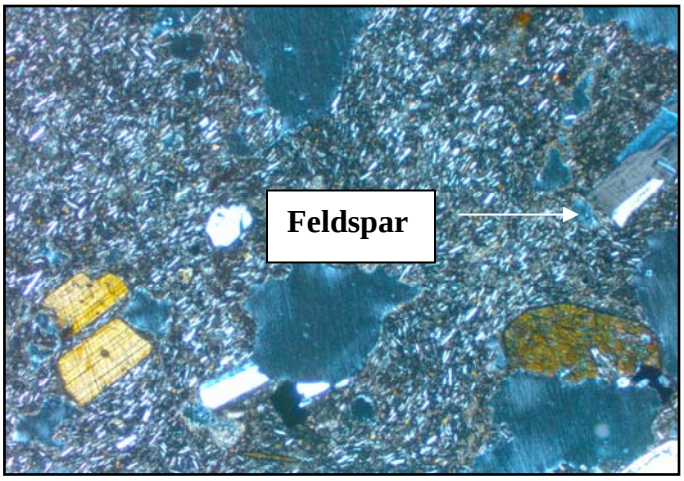

Thin Section Number: DV51
Diagenetic Facies: TRACHYTE
Field Observations: Flow unit that appears to have clasts of purple orange andesite.
Optical Notes: An abundant amount of feldspars that are randomly oriented.

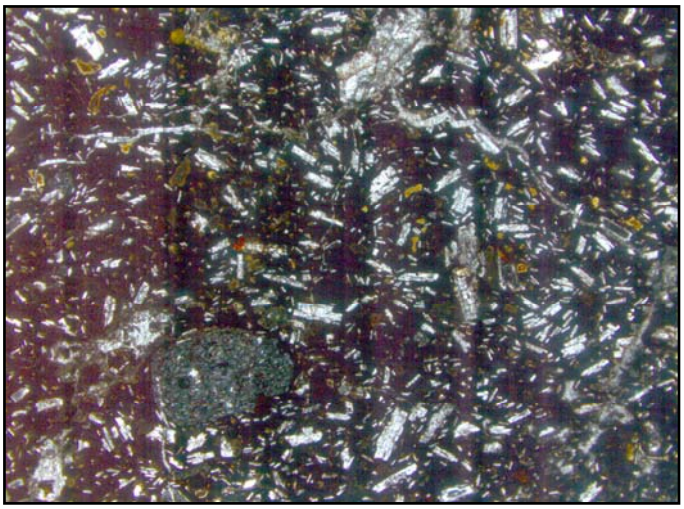

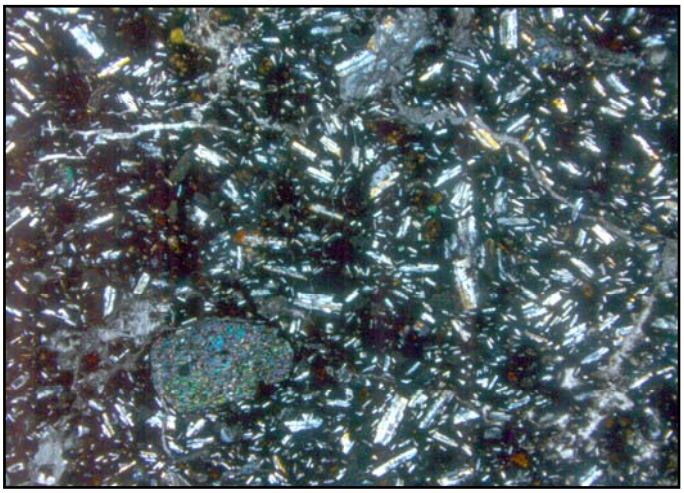

Thin Section Number: DV34
Diagenetic Facies Type: DACITE
Field Observations: Basalt and andesite are in contact
Optical Notes: *Fine grained groundmass *Plagioclase *Microphenocrysts of amphibole

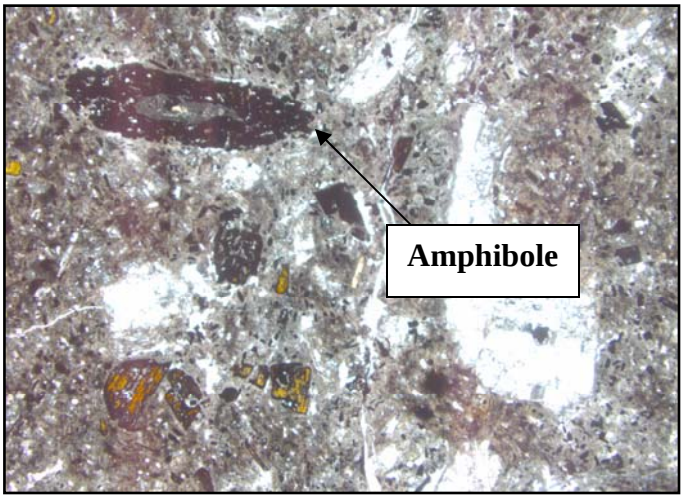

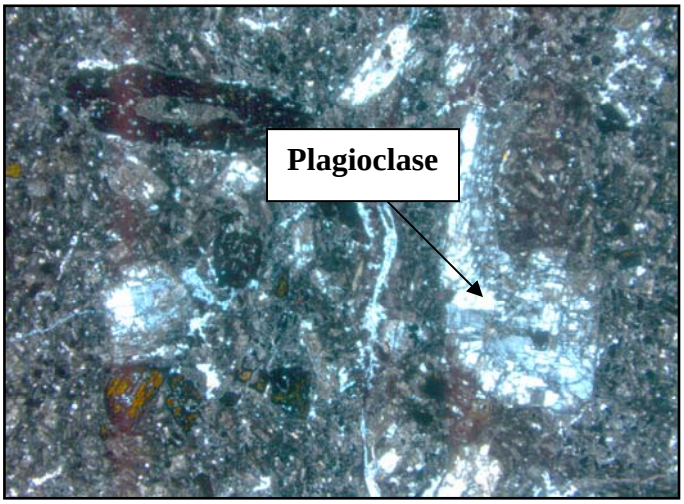

Thin Section Number: DV33
Diagenetic Facies Type: RHYOLITIC TUFF
Field Observations: Very altered rhyolite. Feldspars and amphiboles visible. Flow unit in contact with black vitrosphere. Purplish grey in color.
Optical Notes: *Small phenocrysts of amphibole and zoned feldspars *Glassy matrix *Tuffaceous and cryptocrystalline texture *Smaller mineral maybe quartz

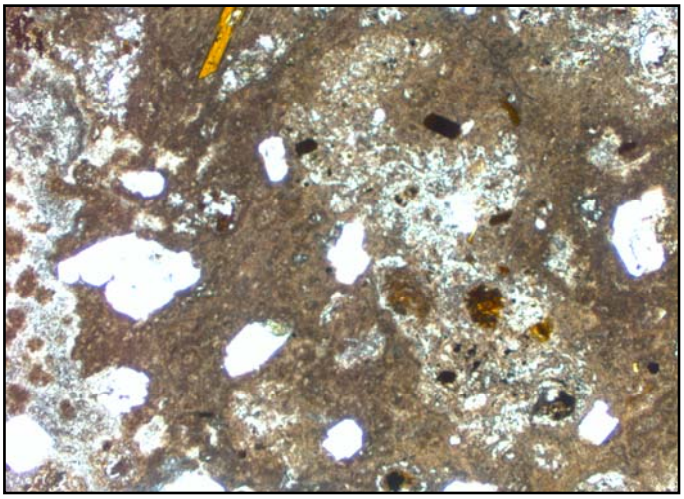

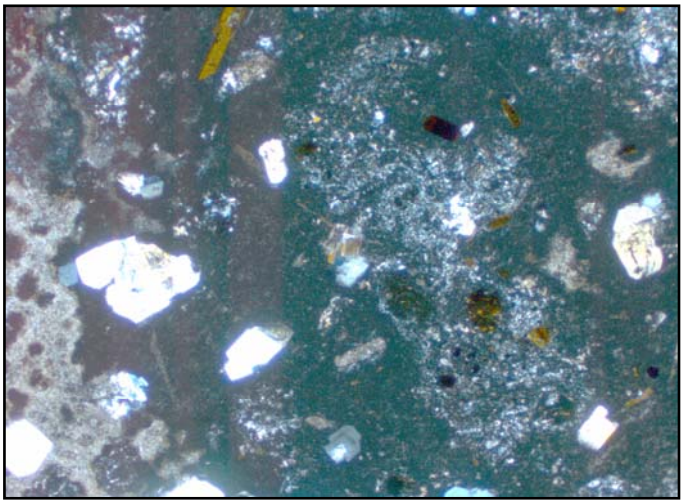

Thin Section Number: DV09
Diagenetic Facies Type: TRACHYANDESITE
Field Observations: Chunky basalt/clast supported. Grayish tanish brown. Overlain by Mega Breccia Granite.
Optical Notes: *Intergranular texture *Abundant amounts of feldspar phenocrysts *Zoned pyroxene *Altered calcite

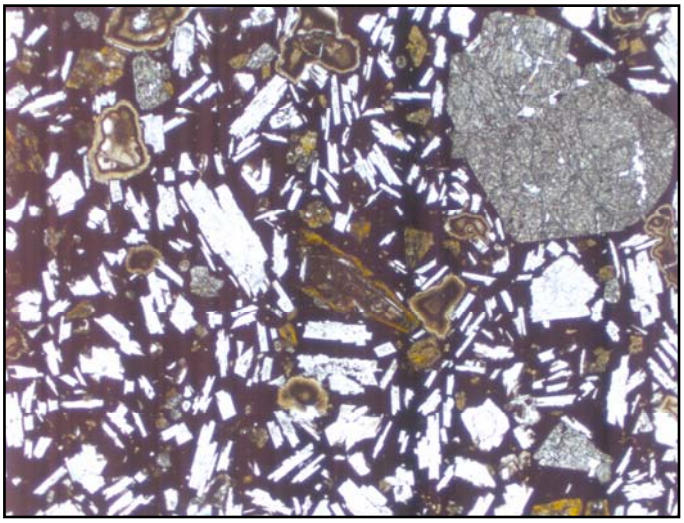

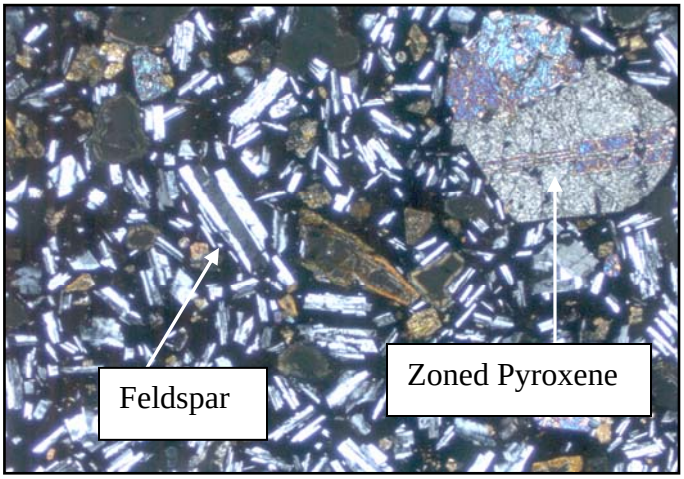

Thin Section Number: DV64C
Diagenetic Facies Type: TRACHYANDESITE
Field Observations: In contact with tuff.
Optical Notes: *Small phenocrysts of CPX *Fine grained groundmass *Feldspars have twinning and zoning *Hornblende

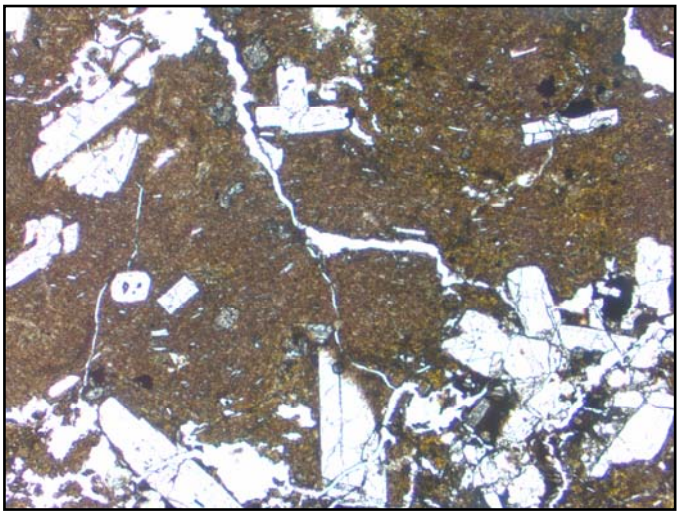

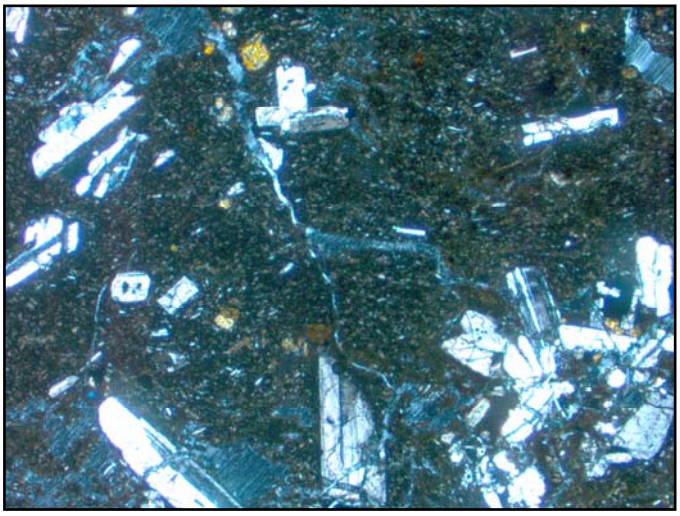

Thin Section Number: DV49
Diagenetic Facies Type: TRACHYTE
Field Observations: Pinkish grey flow unit. Has lots of feldspars and small amounts of mafic mineral. Fault surface.
Optical Notes: *Trickitic texture * Twinned feldspars *Few CPX *Oxides *Amphibole with very high relief

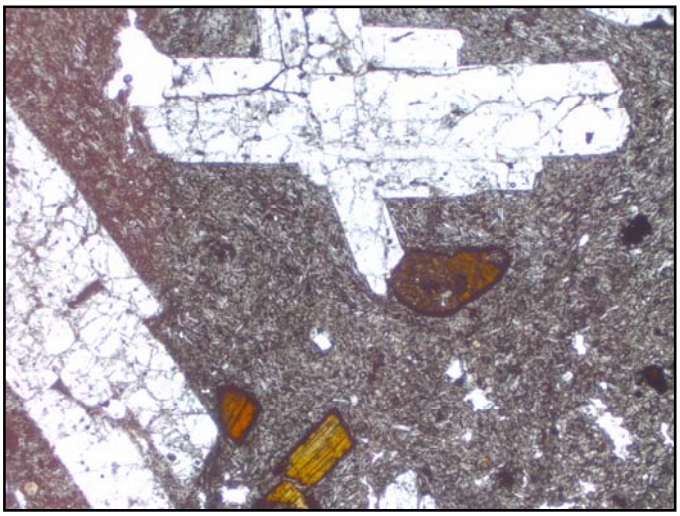

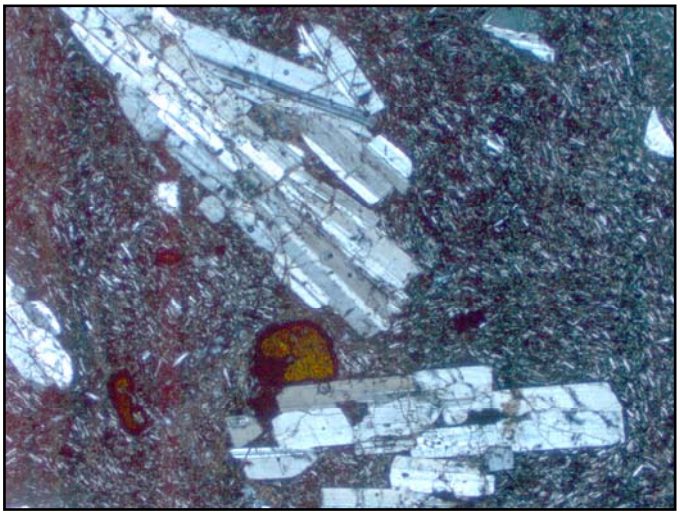

Thin Section Number: DV52
Diagenetic Facies Type: TRACHYANDESITE
Field Observations: Tuffaceous unit with large clasts. In contact with andesitic flow. Lots of fragments. Clasts appear to be andesitic/basalt in composition.
Optical Notes: *Trickitic texture *Lots of feldspars that are randomly oriented *CPX *Mafic glassy matrix

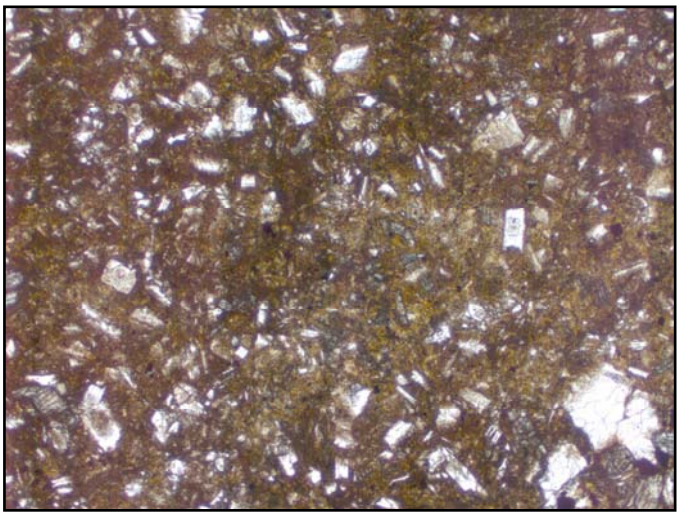

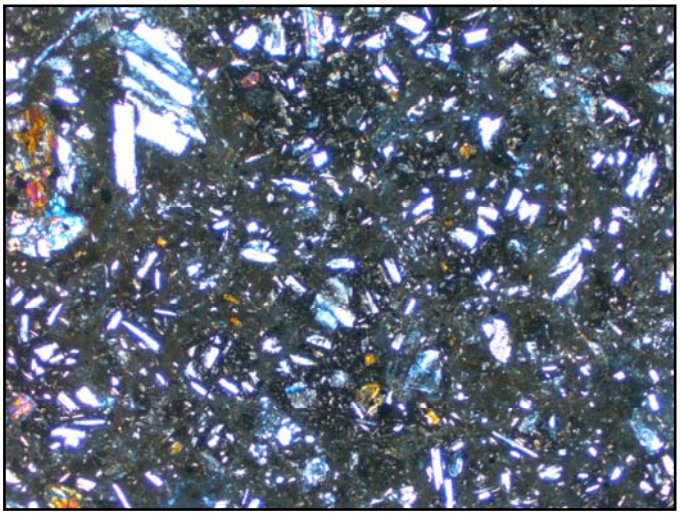

Thin Section Number: DV50
Diagenetic Facies Type: TRACHYANDESITE
Field Observations: Unit in contact with andesitic flow unit. Red weathering on rock. Unit is brown gray in color. Feldspar and mafic minerals. Fine grained.
Optical Notes: *Trickitic texture *Highly opylitic *Very small amounts of CPX *Feldspar crystals

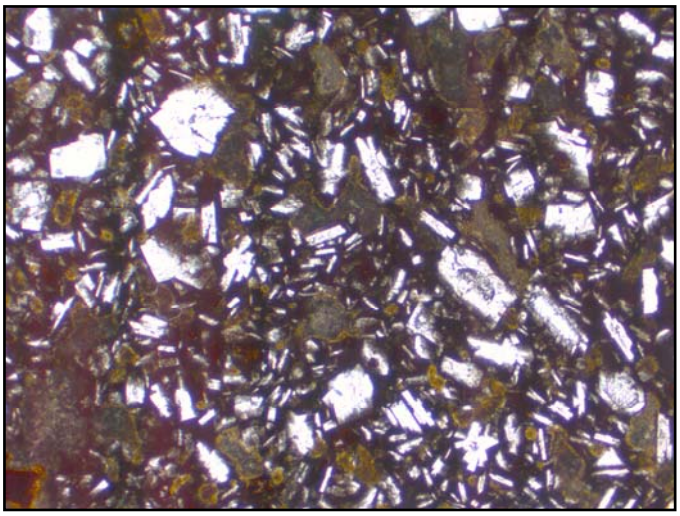

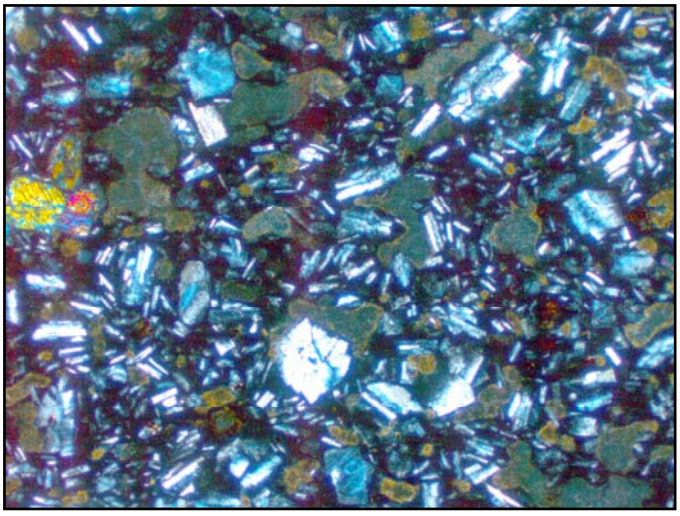

Thin Section Number: DV44
Diagenetic Facies Type: BASALTIC TRACHYANDESITE
Field Observations: Brecciated flow. Gray matrix with clasts of basalt, scoria, and pumice
Optical Notes: *CPX is in clustered groups *Extreme fine grained trickitic texture *Oxy hornblende *Lots of phenocrysts of feldspars that have some orientation

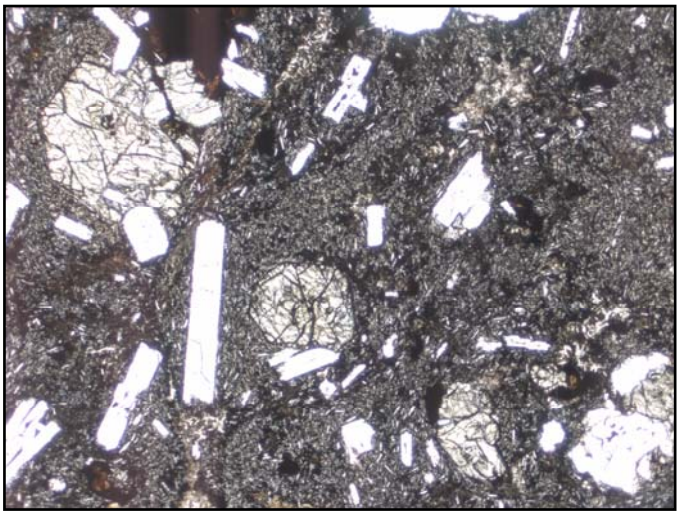

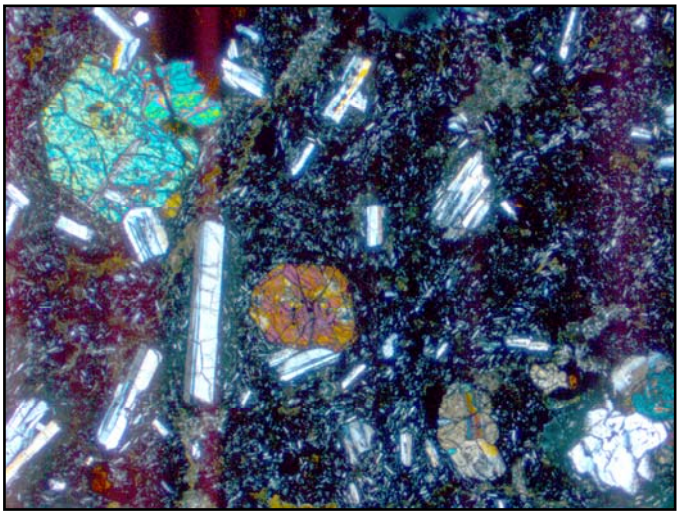

Thin Section Number: DV23
Diagenetic Facies Type: ANDESITE
Field observations: Very solid andesite
Optical Notes: *Very glassy matrix *Feldspars are very abundant *Small amounts of amphibole *Mica and quartz may be present

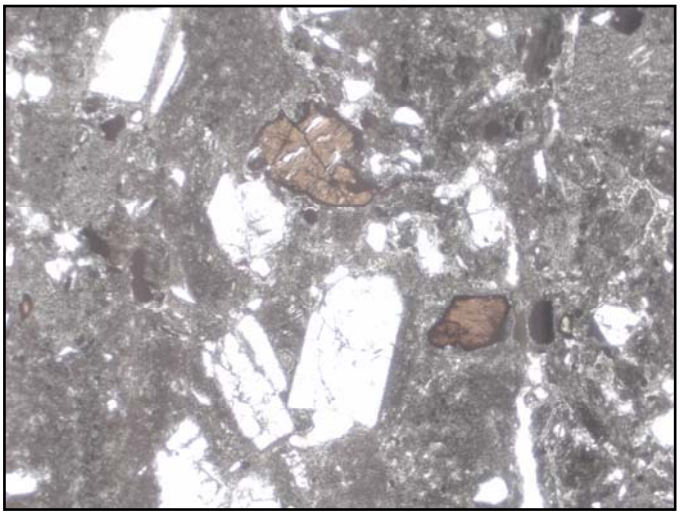

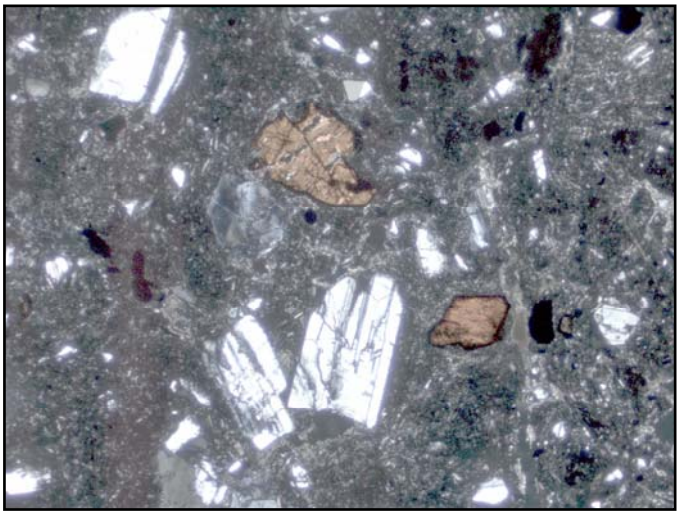

Thin Section Number: DV45
Diagenetic Facies Type: RHYOLITE
Field observations: Intrusive and is contact with a tuff unit
Optical Notes: *Very flowish rock *Banding is observable *Big phenocryts of alkali feldspar and plagioclase

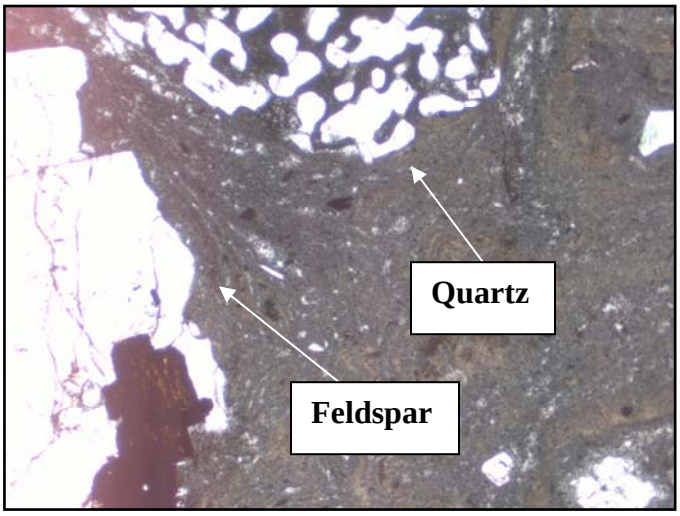

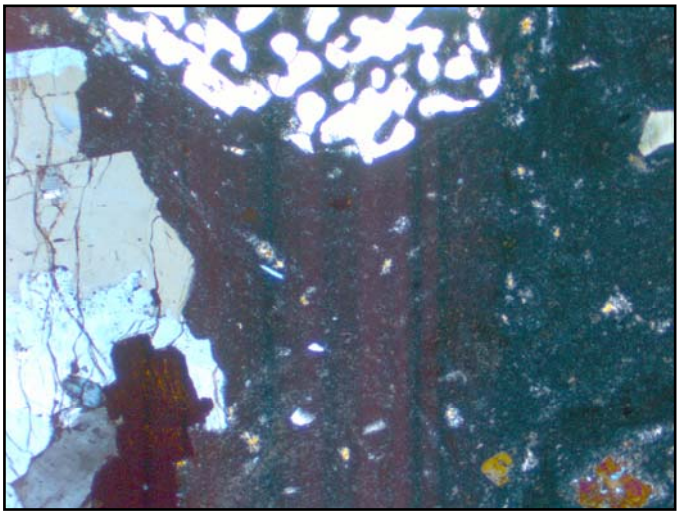

Thin Section Number: DV48
Diagenetic Facies Type: TRACHYANDSESITE
Field observations: In contact with rhyolite. Fault surface.
Optical Notes: *Glass matrix *Little amounts of pyroxene *Feldspars with twinning and zoning

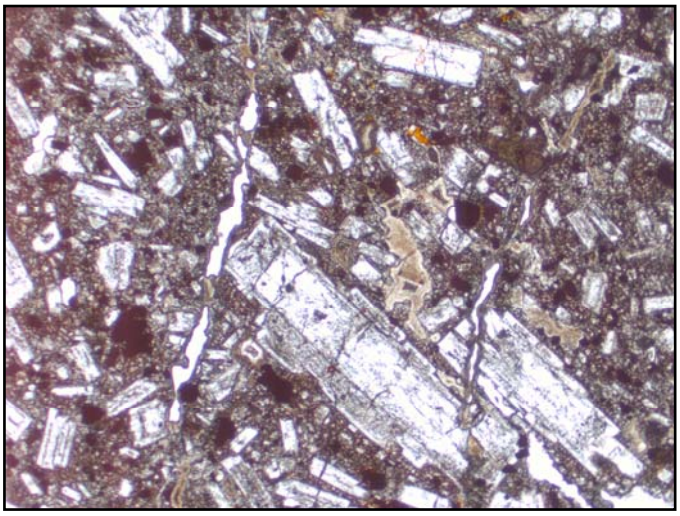

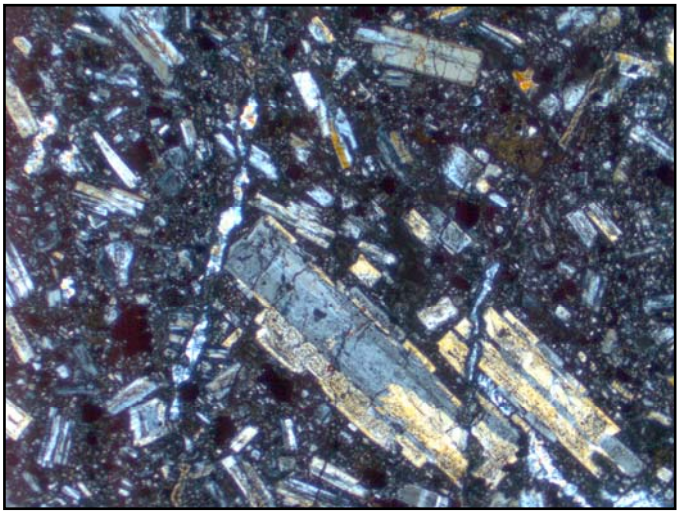

Thin Section Number: DV32
Diagenetic Facies Type: RHYOLITE
Field observations: White pinkish tuff unit
Optical Notes: *Sanidine and feldspars *Super glassy matrix *Tuffaceous texture *Biotite and quartz also may be present

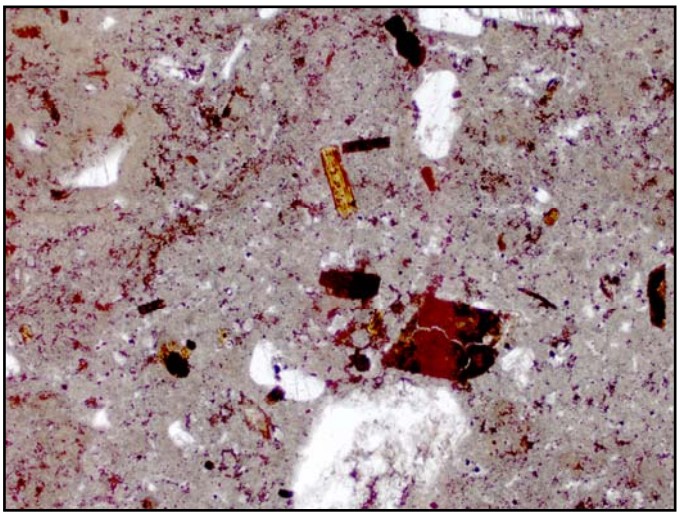

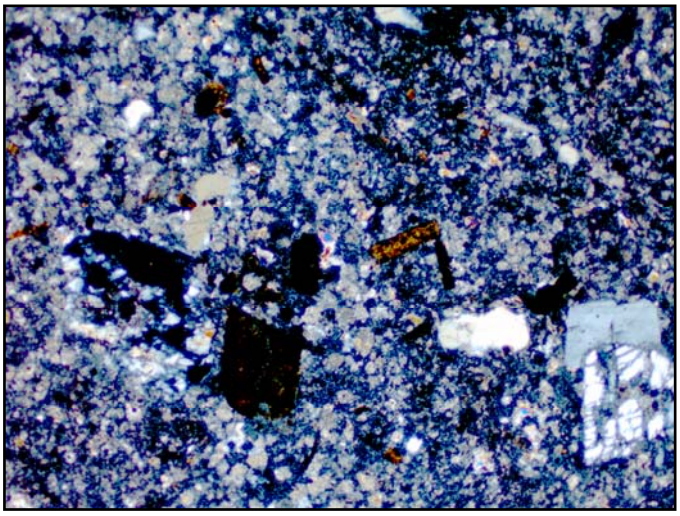

Thin Section Number: DV70
Diagenetic Facies Type: DACITE
Field observations: ~100 m in thickness
Optical Notes: *Large amounts of amphibole *Pyroxene altered to iron oxide (hematite)

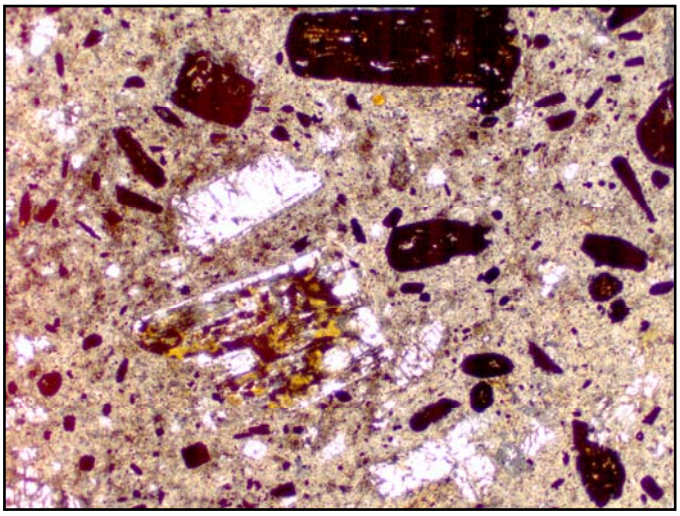

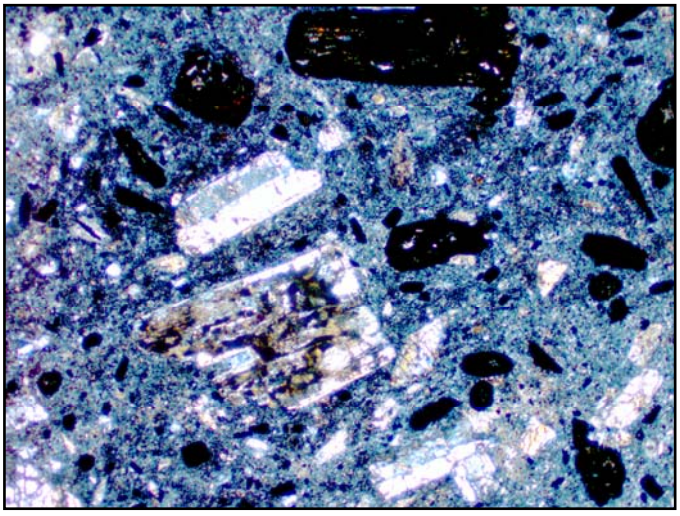

Thin Section Number: DV73
Diagenetic Facies Type: TRACHYANDESITE
Field observations: In contact with tuff
Optical Notes: *CPX *No quartz

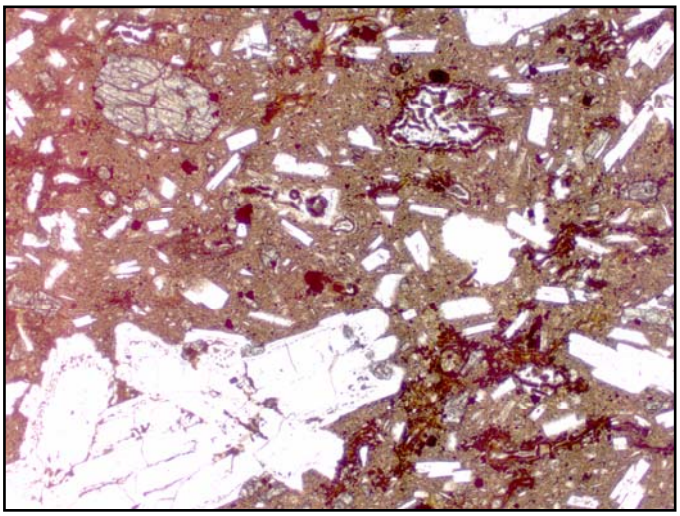

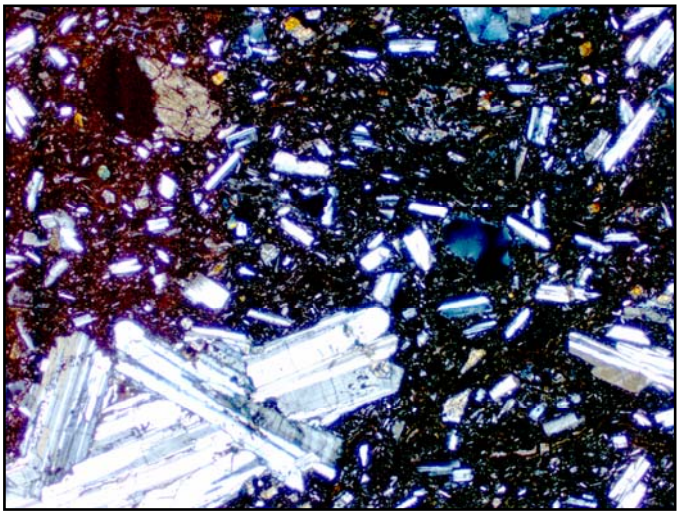

Thin Section Number: DV69
Diagenetic Facies Type: TRACHYTE
Field Observations: In contact with rhyolite
Optical Notes: *Lots of feldspars

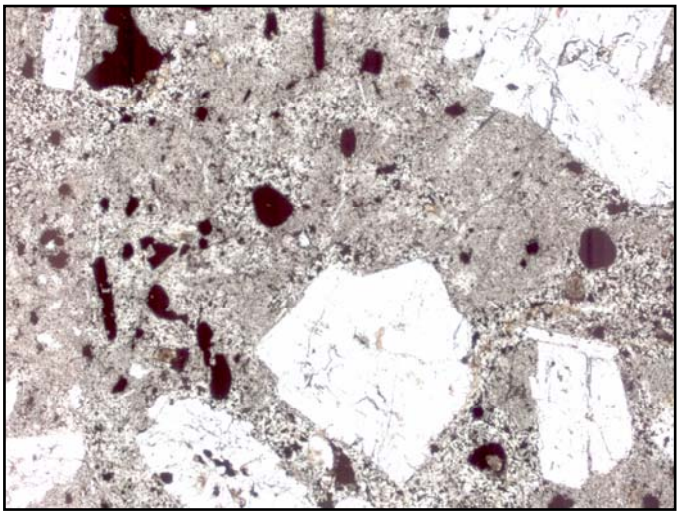

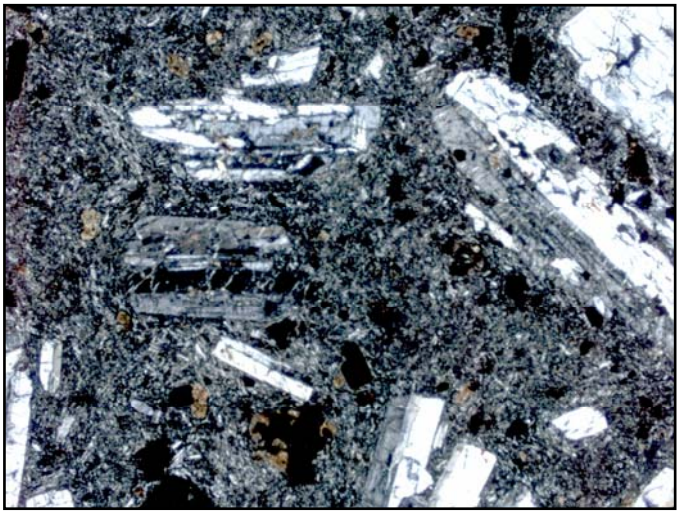

Thin Section Number: DV58
Diagenetic Facies Type: RHYOLITIC TUFF
Field Observations: Extremely welded. Fault surface
Optical Notes: *Feldspar and CPX *Sanidine *Biotite or amphibole may be present

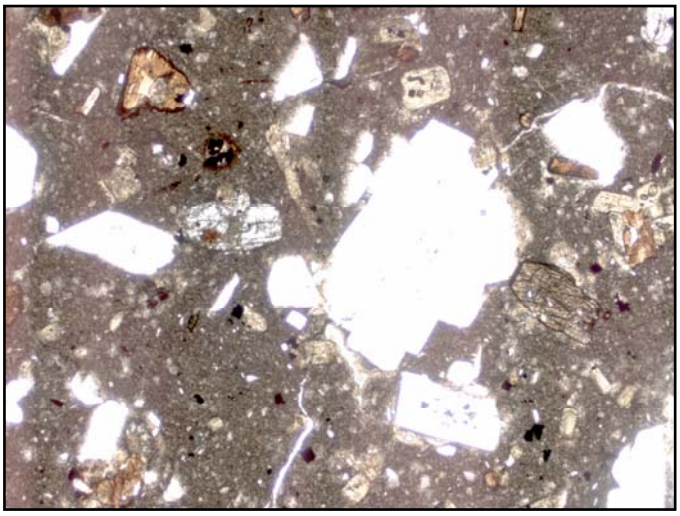

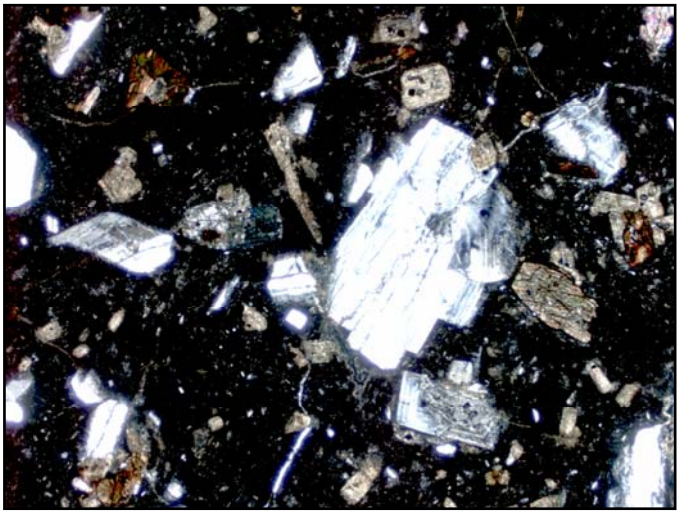

Thin Section Number: DV57
Diagenetic Facies Type: TRACHYANDESITE
Field Observations: May be an andesite
Optical Notes: *Feldspars *Yellow hued CPX

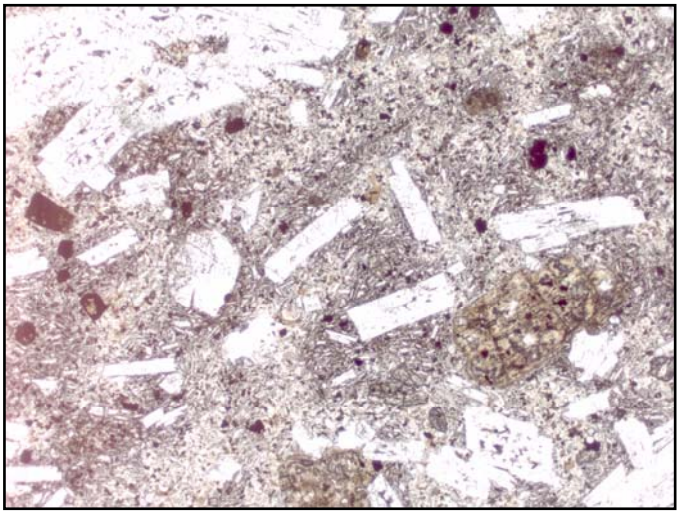

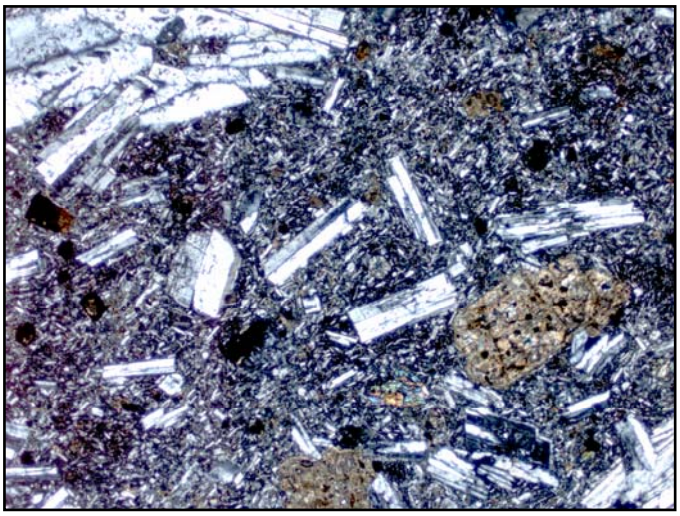

Thin Section Number: DV62
Diagenetic Facies Type: TRACHYTE
Field Observations: Andesite? Fault surface
Optical Notes: *Trickitic texture *Mostly all feldspars

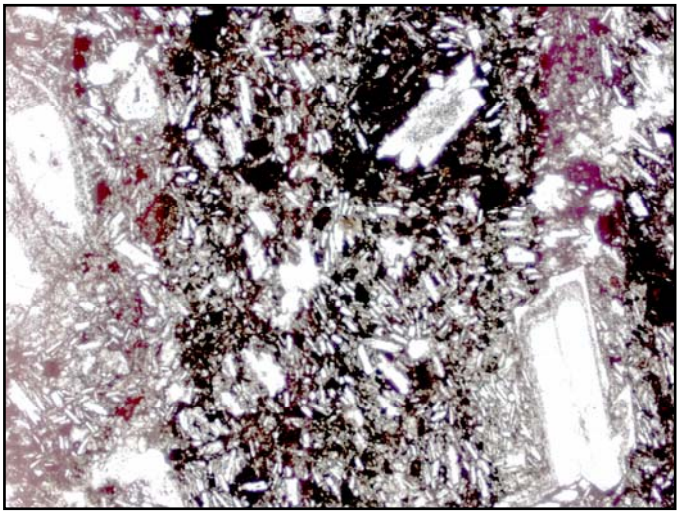

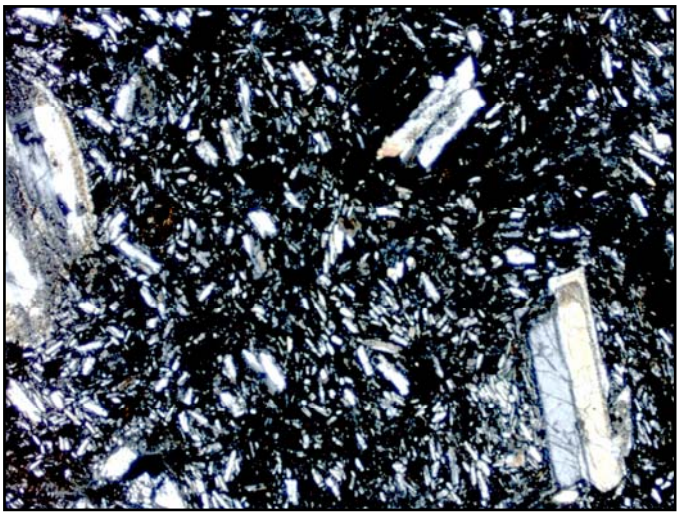

Thin Section Number: DV67
Diagenetic Facies Type: RHYOLITE
Field Observations: Felsic in composition. Aphanitic. White in color.
Optical Notes: *Very tuffaceous *Sanidine *Very small amounts of biotite and amphibole

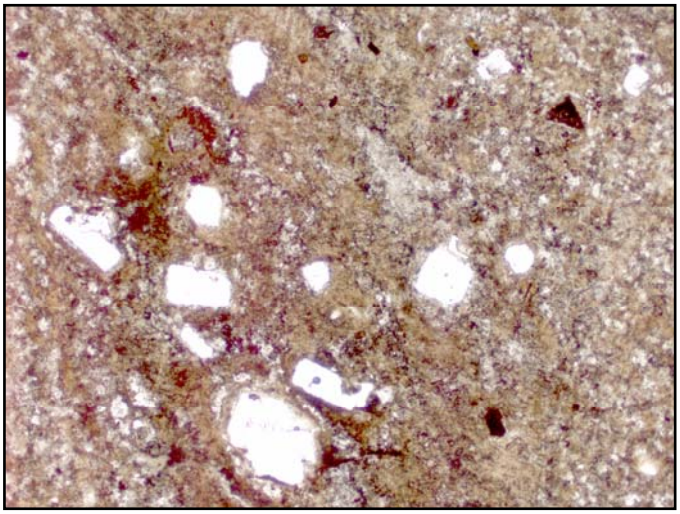

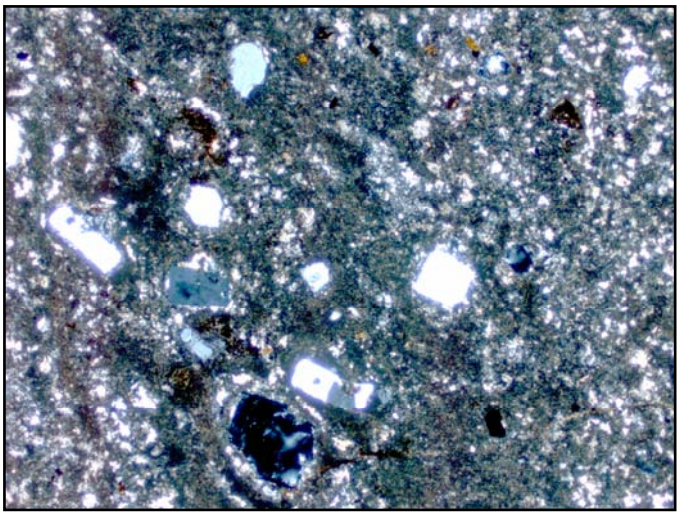

Thin Section Number: DV65
Diagenetic Facies Type: TRACHYANDESITE
Field Observations: Basalt?
Optical Notes: *Amphibole

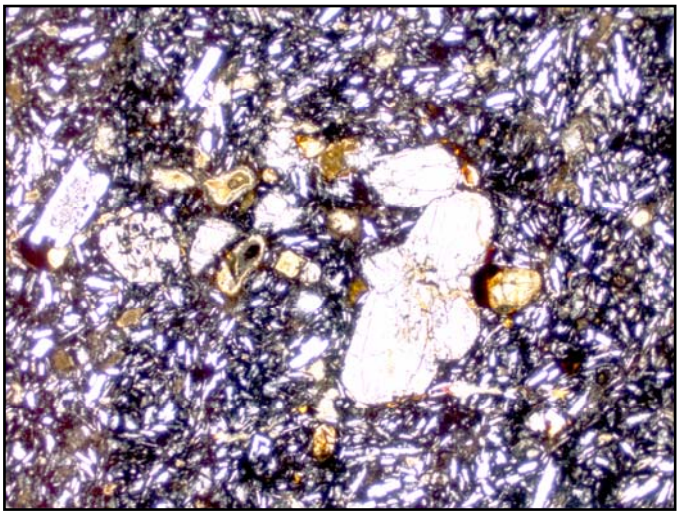

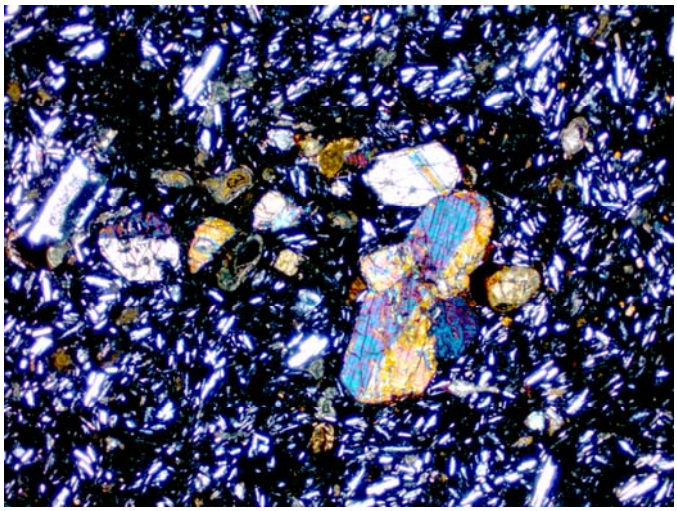

Thin Section Number: DV56
Diagenetic Facies Type: RHYOLITE
Field Observations: Fault surface.
Optical Notes: *Biotite and Sanidine *Glassy

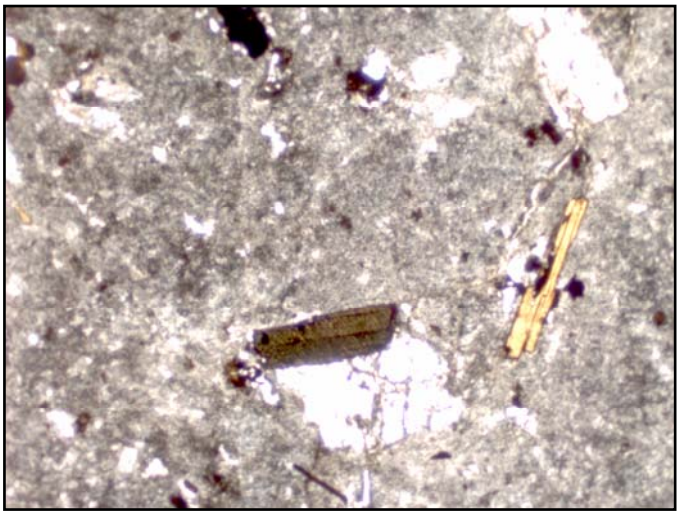

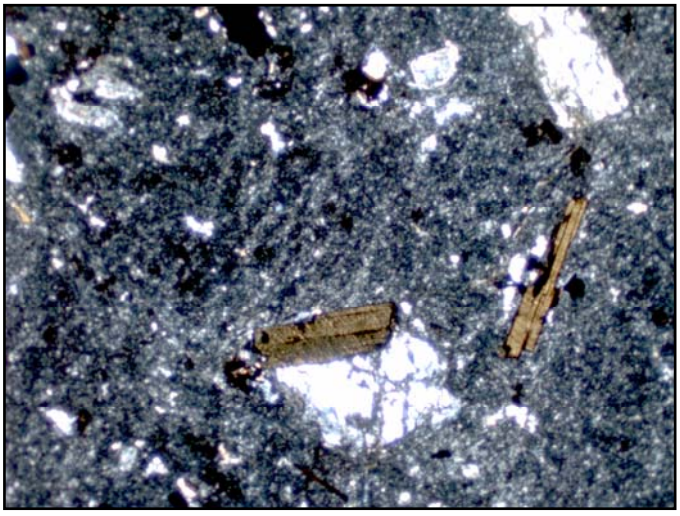

Thin Section Number: DV63
Diagenetic Facies Type: GRANITE
Field Observations: Coarse grained.
Optical Notes: Mica, Quartz, and Feldspars

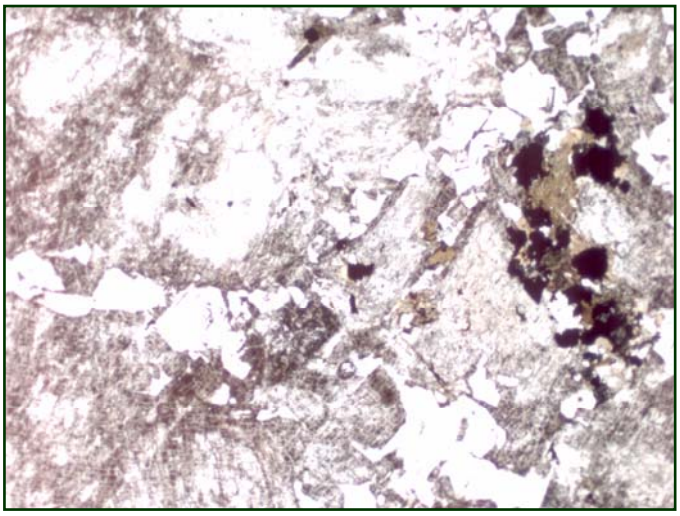

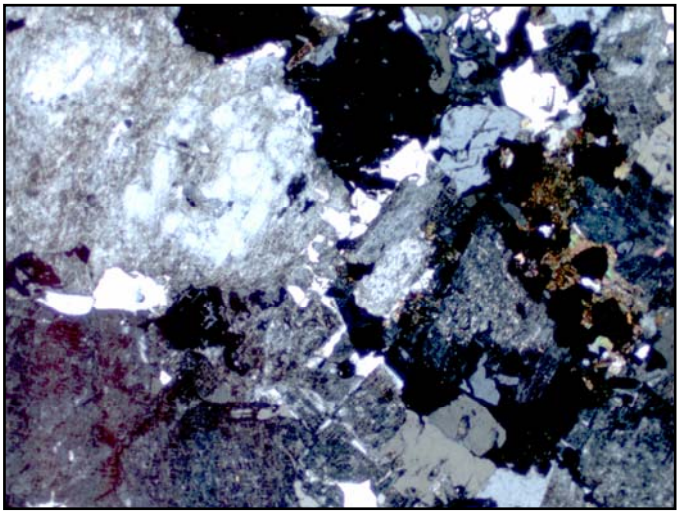

Thin Section Number: DV66
Diagenetic Facies Type: RHYOLITE
Field Observations: Andesite?
Optical Notes: *Flow rock *Very glassy matrix *Amphibole/Feldspars

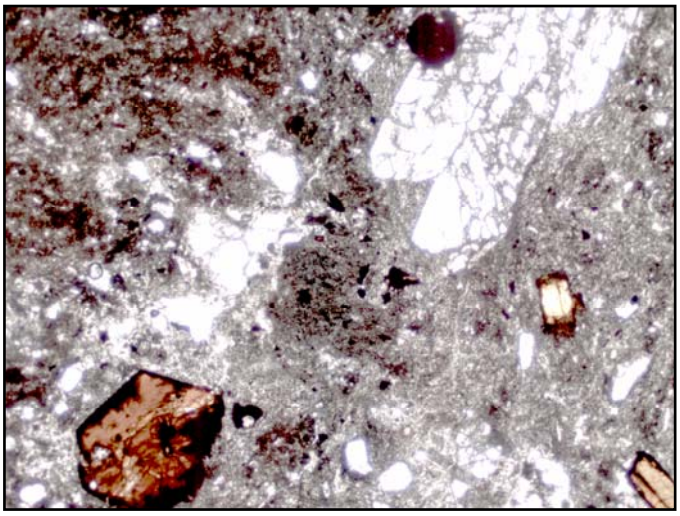

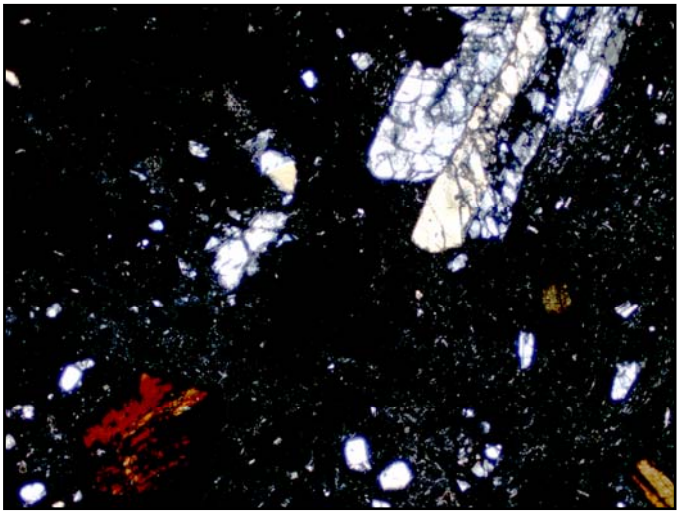

APPENDIX B: Microprobe Analyses

Sample DV60

Point	#1	#2	#3	#4	#5	#6	#7	#8
SiO2	55.264	71.981	71.525	71.379	65.259	65.839	72.051	0
TiO2	0.325	0.052	0.072	0	0	0	0.063	4.951
Al2O3	8.895	12.623	12.506	15.733	21.447	21.381	12.553	0.979
Cr2O3	0.218	0	0	0	0	0	0	0.2
FeO	4.489	0.709	0.789	0.271	0.16	0.239	0.786	83.989
MnO	0.098	0.125	0.071	0.01	0.053	0	0.068	3.054
MgO	11.137	0	0	0	0	0	0	0.552
CaO	13.801	0.379	0.378	0.038	1.871	1.834	0.392	0.036
Na2O	5.072	2.131	2.247	4.707	9.138	9.122	2.154	0
K2O	0.137	5.284	4.944	7.456	1.945	2.103	4.916	0.069
P2O5	0	0	0	0	0	0	0	0
F	0.012	0.086	0.019	0.036	0.076	0	0.019	0.041
Cl	0.005	0.063	0.043	0.003	0	0	0.036	0.04
SO2	0.012	0	0.028	0.002	0.06	0.012	0.042	0.092
ZrO2	0	0	0	0	0	0	0	0.324
La2O3	0	0	0	0	0	0	0	0.164
Ce2O3	0.013	0	0	0	0	0	0	0.369
Total	99.482	93.437	92.624	99.641	100.011	100.533	93.085	94.862
	CPX	Glass	Glass	Glass	Na-Plag	Na-Plag	Glass	Magnetite

Point	#9	#10	#11	#12	#13	#14
SiO2	3.395	73.521	48.348	70.821	65.3	71.437
TiO2	4.605	0.08	0.234	0.062	0	0.08
Al2O3	1.232	12.85	32.659	12.461	21.596	12.608
Cr2O3	0.167	0	0.006	0	0.02	0
FeO	74.711	0.67	3.295	0.677	0.221	0.798
MnO	2.774	0.059	0.023	0.11	0	0.139
MgO	0.741	0	1.099	0	0	0
CaO	0.08	0.299	0	0.299	1.934	0.357
Na2O	0	3.223	0.811	2.03	8.936	2.07
K2O	0.334	4.964	8.589	4.863	2.094	5.513
P2O5	0.014	0	0	0	0	0
F	0.045	0.042	0.047	0	0.023	0.019
Cl	0.038	0.05	0.005	0.061	0	0.055
SO2	0.1	0	0	0.028	0	0
ZrO2	0.24	0	0	0	0	0
La2O3	0.192	0	0	0	0	0
Ce2O3	0.296	0	0	0	0	0
Total	88.965	95.761	95.119	91.416	100.127	93.081
	Magnetite +Si	Glass	Nephiline	Glass	Na-Plag	Glass

Sample DV79

Point	#1	#2	#3	#4	#5	#6	#7	#8
SiO2	38.479	66.249	66.008	28.427	66.305	65.229	19.769	20.428
TiO2	3.123	0	0	33.113	0	0	18.67	0.083
Al2O3	11.941	18.866	19.113	1.496	19.038	18.692	2.66	2.898
Cr2O3	0.031	0.003	0	0.183	0	0.003	0.666	0.02
FeO	13.862	0.19	0.131	2.766	0.125	0.156	7.891	7.72
MnO	0.901	0	0	0.475	0	0	0.541	0.506
MgO	15.19	0	0	0	0	0	0.781	0.768
CaO	0.069	0.312	0.369	25.04	0.337	0.378	5.544	0.098
Na2O	0.504	5.284	5.315	0.075	5.335	5.204	0.071	0.055
K2O	9.323	8.793	8.985	0	9.054	8.996	0.039	0.027
P2O5	0.011	0	0.005	0.119	0	0	0.112	0
F	0.087	0	0	0.164	0	0	0.135	0.09
Cl	0.05	0	0	0.016	0	0	0.055	0.088
SO2	0.066	0.022	0.012	0.044	0.004	0.006	0.108	0.096
ZrO2	0.038	0	0	0.393	0	0	1.255	0.007
La2O3	0.102	0	0	0.439	0	0	9.104	9.986
Ce2O3	0	0	0	1.79	0	0	21.912	0
Total	93.782	99.724	99.941	94.544	100.202	98.668	89.317	42.872
	Biotite	AK Feldspar	AK Feldspar	Sphene	AK Felspar	AK Feldspar	Cheskavite	?

Point	#9	#10	#11	#12	#13	#14	#15	#16
SiO2	20.199	0.028	20.31	39.945	66.838	0.866	29.959	49.46
TiO2	18.702	5.214	18.904	2.365	0	5.189	32.645	1.893
Al2O3	2.887	0.771	2.719	12.043	17.596	0.964	1.589	12.51
Cr2O3	0.706	0.206	0.71	0.022	0.006	0.183	0.13	0.034
FeO	7.399	85.927	7.76	10.338	0.078	79.477	3.161	8.85
MnO	0.425	3.473	0.554	0.766	0	3.605	0.603	0.704
MgO	0.973	0.373	0.658	14.868	0	0.245	0.045	12.182
CaO	5.748	0.041	5.856	0.213	0.018	0.112	24.73	0.193
Na2O	0.058	0.038	0.057	0.093	1.039	0.024	0.082	0.603
K2O	0.04	0.035	0.054	7.983	14.939	0.089	0.046	9.073
P2O5	0.142	0.053	0.142	0.011	0.021	0.032	0.11	0
F	0.098	0.041	0.111	0.557	0	0.074	0.125	0.427
Cl	0.063	0.019	0.062	0.079	0	0.022	0.021	0.05
SO2	0.134	0.084	0.08	0.07	0	0.086	0.058	0.04
ZrO2	1.352	0.4	1.271	0.028	0.001	0.338	0.321	0.043
La2O3	9.904	0.206	10.718	0	0	0.24	0.418	0
Ce2O3	23.366	0.221	23.592	0	0	0.285	1.89	0
Total	92.197	97.13	93.56	89.386	100.541	91.833	95.935	96.066
	Cheskavite	Magnetite	Cheskavite	Biotite	Feldspar	Magnetite	Sphene	Biotite

Point	#17	#18	#19	#20	#21	#22	#23	#24
SiO2	0	20.109	0	39.893	55.679	65.432	0.109	0
TiO2	5.009	19.014	5.117	4.597	0.3	0	4.746	5.039
Al2O3	0.752	2.689	0.703	14.267	8.765	20.355	0.752	0.707
Cr2O3	0.18	0.69	0.199	0	0.202	0	0.132	0.175
FeO	83.647	7.952	86.062	11.2	4.514	0.188	82.396	86.301
MnO	3.235	0.485	3.269	0.045	0.063	0	3.662	3.309
MgO	0.386	0.943	0.411	11.683	10.719	0	0.335	0.302
CaO	0.091	5.488	0.05	10.175	13.729	2.081	0.069	0.053
Na2O	0.032	0.044	0.019	2.51	4.94	8.921	0	0
K2O	0.03	0.031	0.037	1.853	0.12	1.766	0.055	0.039
P2O5	0.082	0.179	0.082	0	0	0	0	0
F	0.016	0.062	0.069	0.069	0	0	0	0.044
Cl	0.026	0.062	0.027	0.011	0	0	0.012	0.014
SO2	0.11	0.112	0.068	0.036	0.004	0.008	0.048	0.064
ZrO2	0.34	1.349	0.336	0	0	0	0.261	0.34
La2O3	0.19	10.901	0.231	0	0	0	0.182	0.19
Ce2O3	0.272	22.932	0.312	0	0	0	0.262	0.276
Total	94.399	93.043	96.995	96.342	99.042	98.753	93.021	96.856
	Magnetite	Cheskavite	Magnetite		CPX	Feldspar	Magnetite	Magnetite

Point	#25	#26	#27	#28	#29	#30	#31	#32
SiO2	28.897	0	40.704	40.413	0	66.222	1.207	39.913
TiO2	32.553	4.579	2.504	3.998	4.537	0.002	4.841	2.645
Al2O3	1.495	0.648	11.828	12.863	0.69	19.015	0.748	12.036
Cr2O3	0.132	0.19	0.004	0	0.168	0	0.158	0.007
FeO	2.79	85.227	11.281	14.379	84.059	0.228	81.518	12.207
MnO	0.591	3.184	0.917	0.094	3.33	0	2.195	0.996
MgO	0	0.313	16.897	13.371	0.209	0	0.035	17.013
CaO	25.896	0.045	0.01	0.123	0.066	0.348	0.113	0.024
Na2O	0.031	0	0.307	0.096	0	5.132	0	0.431
K2O	0.036	0.049	8.665	7.164	0.035	8.495	0.099	9.009
P2O5	0	0	0	0	0	0	0	0
F	0.09	0.093	0.948	0.449	0.072	0	0.013	1.037
Cl	0.008	0.016	0.039	0.138	0.018	0	0.016	0.04
SO2	0.036	0.068	0.048	0.022	0.092	0	0.096	0.038
ZrO2	0.201	0.288	0	0.012	0.338	0	0.147	0
La2O3	0.379	0.133	0.082	0	0.198	0	0.216	0
Ce2O3	1.914	0.252	0	0	0.221	0	0.196	0
Total	95.051	95.086	94.241	93.127	94.034	99.445	91.598	95.402
	Sphene	Magnetite	Biotite	Biotite	Magnetite	AK Feldspar	Magnetite	Biotite

Point	#33	#34	#35	#36	#37	#38	#39	#40
SiO2	45.881	66.654	28.951	64.562	28.617	0.789	0	72.918
TiO2	0.857	0	30.286	0.002	30.792	0.047	4.702	0.083
Al2O3	14.044	19.038	1.496	18.441	1.476	0	0.688	14.677
Cr2O3	0	0	0.105	0	0.098	0.102	0.177	0
FeO	12.135	0.158	2.726	0.215	2.673	0.224	85.579	0.237
MnO	0.129	0	0.504	0	0.547	0.436	3.295	0.005
MgO	9.429	0	0	0	0	0	0.295	0
CaO	3.298	0.292	25.942	0.304	25.381	52.059	0.06	0.365
Na2O	0.52	5.279	0.018	5.161	0.035	0.156	0	4.123
K2O	3.882	7.502	0.019	8.031	0.013	0.007	0.061	6.573
P2O5	1.934	0	0	0	0	36.638	0	0
F	0.853	0	0.119	0	0.223	1.784	0.009	0
Cl	0.029	0	0.001	0	0.012	0.094	0.035	0
SO2	0.036	0	0.052	0.018	0.03	0.262	0.08	0
ZrO2	0.08	0	0.174	0	0.186	1.082	0.267	0
La2O3	0	0	0.409	0	0.358	0.344	0.165	0.053
Ce2O3	0	0	1.662	0	1.629	1.073	0.247	0
Total	93.113	98.927	92.466	96.735	92.072	95.102	95.663	99.039
	Biotite?	AK Feldspar	Sphene	AK-Spar	Sphene		Magnetite	Glass

Point	#41	#42	#43	#44
SiO2	74.131	0	27.712	45.691
TiO2	0.617	4.61	29	2.405
Al2O3	13.598	0.652	1.597	14.295
Cr2O3	0	0.175	0.12	0
FeO	0.54	85.523	3.196	10.72
MnO	0	3.255	0.5	0.611
MgO	0	0.274	0	11.993
CaO	0.139	0.064	22.837	0.141
Na2O	3.924	0	0.057	0.112
K2O	5.678	0.054	0.02	6.161
P2O5	0	0	0	0
F	0	0.031	0.161	0.682
Cl	0	0.021	0.007	0.026
SO2	0	0.052	0.026	0.006
ZrO2	0.031	0.254	0.238	0
La2O3	0	0.215	0.55	0
Ce2O3	0	0.26	1.757	0
Total	98.662	95.441	87.78	92.848
	Glass	Magnetite		Biotite

Sample DV74

Point	#1	#2	#3	#4	#5	#6	#7	#8
SiO2	39.611	73.356	0	62.581	43.774	0	29.062	63.254
TiO2	4.649	0.015	4.492	0	0	35.003	0.137	0
Al2O3	14.632	12.211	0.884	20.523	7.493	0.013	0	10.968
Cr2O3	0.004	0	0.145	0	0	0.149	0.206	0
FeO	11.172	0.207	74.454	0.094	0.32	44.219	0.293	0.695
MnO	0.067	0	2.855	0	0	4.193	0.09	0
MgO	12.22	0	0.458	0	0	1.162	0	0
CaO	10.186	0.157	0.071	1.703	0.215	0.021	0.046	0.101
Na2O	2.565	4.322	0	8.887	1.121	0	0.035	1.684
K2O	1.841	3.41	0.043	1.498	2.569	0.039	0.039	1.629
P2O5	0	0	0	0	0	0	0.066	0
F	0	0.006	0.078	0.012	0	0.094	0.146	0.036
Cl	0.015	0.016	0.015	0	0.154	0.012	0.007	0
SO2	0.046	0.02	0.114	0.024	0.05	0.088	0.08	0
ZrO2	0.072	0	0.367	0	0	0.305	57.784	0
La2O3	0	0	0.156	0	0	0.088	0.124	0
Ce2O3	0	0	0.169	0	0	0.353	0.244	0
Total	97.079	93.72	84.301	95.321	55.698	85.739	88.359	78.366
	Standard	Glass	Magnetite	Na-Plag	Bad Run	Ti-Magnetite	Zircon	Alkali Feldspar

Point	#9	#10	#11	#12	#13	#14	#15	#16
SiO2	54.911	55.057	44.668	34.618	42.993	35.067	0	62.433
TiO2	0.28	0.302	1.83	0	2.624	0	0.13	0.015
Al2O3	8.812	8.852	9.424	12.083	5.955	12.644	25.413	20.151
Cr2O3	0.17	0.187	0	0	0.032	0.015	37.383	0
FeO	4.433	4.501	5.29	9.679	6.421	10.988	16.485	0.374
MnO	0.058	0.072	0.062	0.919	0.08	1.273	0.249	0
MgO	11.426	11.348	13.271	23.356	11.32	23.87	14.49	0
CaO	13.737	14.227	19.714	0.287	20.687	0.271	0.056	0.187
Na2O	5.122	5.11	0.714	0.33	0.43	0.248	0	1.488
K2O	0.099	0.1	0	0.139	0.005	0.11	0.03	12.016
P2O5	0	0	0	0	0	0	0	0
F	0.024	0.041	0	0.046	0.024	0.035	0.355	0
Cl	0	0	0	0.012	0.009	0.029	0.015	0
SO2	0.036	0.024	0.044	0.048	0.016	0.014	0.084	0.056
ZrO2	0	0.063	0.047	0.011	0.015	0	0.185	0
La2O3	0	0	0	0	0	0	0	0.032
Ce2O3	0	0	0	0	0	0	0.045	0
Total	99.108	99.885	95.066	81.527	90.611	84.563	94.92	96.752
	Standard	CPX	CPX	Amphibole	CPX	Amphibole	Spinel	K-Spar

Point	#17	#18	#19	#20	#21	#22	#23	#24
SiO2	0	0	32.96	0	33.837	43.224	44.054	0
TiO2	0.075	0.067	0	0.095	0	3.173	3.561	0.178
Al2O3	34.002	34.624	12.276	35.355	11.754	7.493	7.688	32.423
Cr2O3	33.392	31.794	1.128	31.815	0.019	0.016	0.023	34.972
FeO	14.12	14.349	11.612	12.902	10.256	7.182	6.782	14.003
MnO	0.198	0.194	0.345	0.183	1.074	0.187	0.145	0.244
MgO	15.775	16.486	25.597	16.619	22.653	12.611	12.183	16.317
CaO	0.007	0	0.16	0.01	0.253	20.67	22.019	0.057
Na2O	0.007	0	0.086	0.015	0.213	0.412	0.485	0
K2O	0.008	0	0.031	0	0.119	0.008	0	0.017
P2O5	0	0	0	0	0	0	0	0
F	0.325	0.309	0.035	0.305	0.041	0	0	0.278
Cl	0.017	0.011	0.016	0.009	0.077	0	0	0.009
SO2	0.048	0.042	0.048	0.036	0.078	0.028	0.058	0.05
ZrO2	0.17	0.226	0	0.169	0	0.215	0.169	0.154
La2O3	0.009	0	0	0.057	0	0	0	0.057
Ce2O3	0.018	0	0	0	0	0	0	0
Total	98.171	98.102	84.294	97.57	80.374	95.219	97.167	98.759
	Spinel	Spinel	Amphibole	Spinel	Amphibole	CPX	CPX	Spinel

Point	#25	#26	#27	#28	#29	#30	#31	#32
SiO2	0	46.147	61.939	45.049	44.585	43.721	32.641	93.934
TiO2	0.0778	2.33	0	2.62	3.333	3.199	0	0
Al2O3	0	6.226	19.04	6.687	7.038	6.762	11.941	1.736
Cr2O3	0.1493	0.151	0	0.023	0.028	0.05	0	0
FeO	47.5579	6.028	0.224	6.107	6.411	6.331	15.506	0.149
MnO	0.0624	0.11	0	0.065	0.085	0.07	0.239	0
MgO	0	13.608	0	13.139	12.548	12.59	23.506	0
CaO	0.0365	21.595	0	22.432	22.357	23.869	0.076	0.083
Na2O	0.0319	0.511	1.1	0.427	0.427	0.434	0.09	0.058
K2O	0.0305	0	12.453	0.002	0.024	0.005	0.023	0.743
P2O5	0	0	0	0	0.05	0.564	0	0
F	0.2459	0.055	0.073	0.043	0.031	0.074	0.005	0
Cl	0.0131	0	0	0	0	0.003	0.014	0.031
SO2	52.5999	0.04	0.032	0.018	0.03	0.034	0.046	0.018
ZrO2	0.3443	0.112	0.011	0.176	0.149	0.188	0.039	0
La2O3	0.1734	0	0	0.021	0	0	0.011	0
Ce2O3	0.2487	0	0	0	0	0	0	0
Total	101.5716	96.912	94.871	96.808	97.096	97.892	84.137	96.752
	Pyrite?	CPX	K-Spar	CPX	CPX	CPX	Amphibole	Quartz

Point	#33	#34	#35	#36	#37	#38	#39	#40
SiO2	51.623	43.609	49.79	0	44.694	46.555	44.835	43.233
TiO2	0.04	3.188	0.38	0.048	3.261	2.182	2.986	3.216
Al2O3	3.541	7.624	4.468	39.701	6.919	5.984	6.611	6.904
Cr2O3	1.166	0.035	0.399	28.849	0.041	0.013	0.019	0.009
FeO	2.648	6.683	6.304	11.865	6.633	6.95	6.519	6.012
MnO	0.043	0.123	0.145	0.167	0.107	0.177	0.05	0.045
MgO	17.488	12.17	14.206	17.775	12.625	12.913	12.633	12.477
CaO	20.673	22.304	21.602	0.021	22.984	22.329	22.689	23.552
Na2O	0.547	0.402	0.549	0	0.429	0.59	0.414	0.414
K2O	0	0	0	0.007	0	0.001	0.016	0.005
P2O5	0	0	0	0	0	0	0	0
F	0	0.024	0.049	0.437	0.043	0.024	0.024	0.037
Cl	0.008	0	0	0.004	0	0	0	0
SO2	0.036	0.024	0.02	0.028	0.036	0.05	0.056	0.038
ZrO2	0.022	0.119	0.047	0.166	0.138	0.184	0.19	0.132
La2O3	0	0	0	0	0.021	0	0	0.083
Ce2O3	0	0	0	0	0	0	0	0
Total	97.834	96.305	97.959	99.068	97.93	97.952	97.042	96.157
	CPX	CPX	Pyroxene?/CPX	Spinel	CPX	CPX	CPX	CPX

Point	#41	#42
SiO2	33.426	69.734
TiO2	0	0
Al2O3	12.363	16.285
Cr2O3	0.548	0
FeO	9.665	0.225
MnO	0.872	0
MgO	24.271	0
CaO	0.376	0.171
Na2O	0.084	1.223
K2O	0.039	8.756
P2O5	0	0
F	0	0.079
Cl	0.14	0.009
SO2	0.014	0.034
ZrO2	0	0.047
La2O3	0.02	0
Ce2O3	0	0
Total	81.817	96.563
	Amphibole	K-Spar

Sample DV93

Point	1	2	3	4	5	6	7	8
SiO2	39.266988	55.003241	0.2614407	65.451892	72.9161	28.109689	35.413784	28.478443
TiO2	4.7154832	0.3125863	1.0593574	0	0.0535433	32.774527	4.0417713	33.360834
Al2O3	14.825945	8.9134798	0.070481	19.602589	12.073597	1.5717444	12.655206	1.4972953
Cr2O3	0	0.1568429	0	0	0	0.1192766	0	0.0999819
FeO	10.722277	4.3581326	17.246739	0.1551697	0.54155	2.5497495	17.923258	2.7581864
MnO	0.0550042	0	0.3917439	0	0	0.3913565	1.1433394	0.3344155
MgO	12.517087	11.49853	0	0	0	0	12.961431	0
CaO	10.275457	13.795708	0	0.2364651	0.3310511	22.515392	0.2212138	26.136106
Na2O	2.5624637	5.0541596	0	4.732807	2.3120135	0.0859996	0.3365845	0.0212977
K2O	2.0615164	0.112534	0	9.4432153	5.1510199	0.0156632	7.7014688	0.0080726
P2O5	0	0	0	0	0	0.0247585	0	0.0105453
total :	97.1315	99.284	19.6663	99.7239	93.5622	91.3764	95.0666	95.6435

Point	9	10	11	12	13	14	15	16
SiO2	65.110502	27.216558	28.509226	39.211408	34.719459	65.493364	44.965028	0
TiO2	0	27.184669	33.119639	3.450793	27.743788	0	19.810034	5.1363238
Al2O3	19.535887	1.8292928	1.4610156	13.235304	3.1990421	19.434417	5.5868918	0.659271
Cr2O3	0	0.0320117	0.0596383	0	0.0675316	0	0.0420976	0.1504113
FeO	0.1393439	2.4065456	2.6549972	13.637564	2.4672754	0.0958552	2.1928334	81.343403
MnO	0	0.3895488	0.3493932	0.5962667	0.3253772	0	0.267145	3.0359503
MgO	0	0	0	14.204896	0	0	0	0.206332
CaO	0.2817992	20.892179	26.167449	0.0843719	21.332647	0.2374445	16.606144	0.0499515
Na2O	4.8564146	0.193836	0.0405735	0.3375281	0.7370621	5.3377695	1.1210947	0.0060658
K2O	9.7686481	0.2225377	0.0055424	8.1371464	0.6501428	8.2036547	1.7472888	0.0762677
P2O5	0	0	0.0176519	0	0	0	0	0.0451613
total :	99.807	82.6732	95.2099	93.8707	93.9496	98.8872	94.0492	91.5067

Point	17	18	19	20	21	22	23	24
SiO2	74.9358	28.046413	1.4510709	41.978661	28.549842	40.15563	39.439715	39.983759
TiO2	0.0914073	32.383877	4.7765326	3.1608916	30.421289	2.9101887	3.3693937	3.4150974
Al2O3	12.562806	1.3948806	0.9621691	12.74704	1.4872806	13.296904	12.061693	13.026507
Cr2O3	0	0.1017359	0.1533348	0	0.0710398	0	0	0
FeO	0.2646634	2.9462943	77.477284	13.76507	2.9245499	12.785674	13.553674	13.945458
MnO	0	0.3212455	3.2766261	0.6557901	0.4697311	0.604272	0.64262	0.5842587
MgO	0	0	0.0031514	12.682783	0	13.069738	13.59751	14.183002
CaO	0.334689	25.071034	0.0766762	0.1697232	25.889007	0.294392	0.1162737	0.0986437
Na2O	3.5544242	0.0552662	0.0181974	0.3403588	0.0451565	0.2384534	0.266356	0.3386065
K2O	5.1742738	0.017109	0.0927743	7.3444686	0.0071087	7.1639805	8.0741322	7.4955581
P2O5	0	0.098117	0.0034387	0	0.129982	0.0316358	0	0
total :	96.9932	93.5652	89.0943	93.7058	92.8958	91.2966	91.9686	94.0514

Point	25	26	27	28	29	30	31	32
SiO2	20.005454	73.334021	39.844167	72.368208	25.463644	36.78576	13.853153	72.302153
TiO2	16.97624	0.0760616	3.3398698	0.0742267	32.743501	3.7670489	5.1483335	0.0405328
Al2O3	2.4638104	11.752937	13.026507	12.332846	1.323077	13.514394	1.8901369	12.410129
Cr2O3	0.6326339	0	0	0	0.1043671	0	0.1074367	0
FeO	8.2605347	0.696591	13.624826	0.6148889	2.4836158	14.69403	69.109572	0.6440958
MnO	0.6197661	0	0.6501089	0	0.336094	0.6925887	1.2233925	0
MgO	0.6007512	0	13.991266	0	0	13.922268	0	0
CaO	5.4927058	0.3847804	0.1089978	0.3208369	25.910275	0.2378643	0.1518134	0.3528786
Na2O	0.0226457	2.4598842	0.3386065	2.3842639	0.0292506	0.2989766	0.3566691	2.4686459
K2O	0.0601225	4.8118517	7.4170012	4.2372537	0.0134944	7.2504895	0.2751902	5.0264374
P2O5	0	0	0	0	0.0696906	0	0.0071066	0
total :	90.5493	93.6871	93.2809	92.5192	91.3082	92.0719	92.7676	93.4104

Point	33	34	35	36	37	38	39	40
SiO2	28.427993	0	63.577129	28.660789	64.578428	37.649818	20.021914	72.650384
TiO2	32.504975	3.8471137	0	31.82359	0	3.338035	18.143852	0.0422008
Al2O3	1.4483554	0.6481225	22.600203	1.4595039	19.167988	12.381975	2.7976974	12.147668
Cr2O3	0.1094831	0.1439798	0	0.0589075	0	0	0.5789886	0
FeO	2.6674777	80.795034	0.1959564	2.7253769	0.1217169	14.937721	7.338909	0.561107
MnO	0.3257646	3.4203344	0	0.3628214	0	0.5823219	0.4209245	0.0254362
MgO	0	1.1636859	0	0	0	14.803491	0.7030879	0
CaO	26.175424	0.0523301	3.2686749	25.437765	0.1428585	0.120891	5.9502447	0.3314709
Na2O	0.0413822	0.0161755	8.8526986	0.0516267	4.6259141	0.268378	0.0537834	2.545749
K2O	0.0145788	0.051809	1.1776307	0.0120486	9.9232317	8.0725659	0.0589177	4.402922
P2O5	0.0419519	0	0	0.0527264	0	0	0.0472245	0
total :	94.7846	91.0382	99.8146	93.9354	98.6079	92.9891	89.252	92.8582

Point	41	42	43	44	45	46	47	48
SiO2	72.572144	72.972536	71.94024	72.447517	65.585712	65.761645	72.361581	26.995306
TiO2	0.0422008	0.0497069	0.0578802	0.0358624	0	0	0.0450365	33.323638
Al2O3	12.315084	12.023334	11.992912	12.093248	19.523794	19.442542	11.959467	1.2684684
Cr2O3	0	0	0	0	0	0	0	0.0776175
FeO	0.7175633	0.6560616	0.6147602	0.6588922	0.1911958	0.1024171	0.8087867	2.5959401
MnO	0	0	0	0	0	0	0	0.4269931
MgO	0	0	0	0	0	0	0	0
CaO	0.3307713	0.3169192	0.3503601	0.3832413	0.2423417	0.2826387	0.3507798	26.140864
Na2O	2.3795461	2.3667405	2.3458472	2.2366628	4.7640796	5.3203809	2.1594249	0.0396299
K2O	4.6363035	4.9494468	4.2374947	4.6396771	9.1998334	8.1067839	4.1668898	0.0110847
P2O5	0	0	0	0	0	0	0	0.0871132
total :	93.2427	93.5029	91.6714	92.6705	99.5916	99.1074	91.9654	94.0399

Point	49	50	51	52	53	54	55	56
SiO2	71.26943	47.738908	39.701583	19.998186	0	19.962914	72.209804	70.928894
TiO2	0.0742267	0.5542819	2.979745	17.486486	4.9206493	18.104153	0.1461183	0.0283563
Al2O3	12.333413	16.485554	12.736836	2.496122	0.7569618	2.7493244	9.2755215	11.489153
Cr2O3	0	0	0	0.6602605	0.1583046	0.5778193	0	0
FeO	0.609099	6.2568384	12.749391	8.1097396	81.044643	7.6976264	2.4949383	0.5194196
MnO	0	0	0.645848	0.801306	2.8315566	0.4482975	0.040543	0
MgO	0	2.4797987	14.630497	0.6248011	0.2303819	0.7782232	0.2441485	0
CaO	0.5444293	1.2069513	0.215477	5.3162665	0.0554084	5.4946647	0.4502631	0.4425675
Na2O	2.3604051	0.2515285	0.3289012	0.0367992	0.01321	0.0319465	1.5727946	2.4656804
K2O	3.5509651	1.4611344	7.6288157	0.0989191	0.0595201	0.051809	2.4217698	3.6736199
P2O5	0	0	0	0.1054528	0	0.1162273	0	0
total :	90.8681	76.8102	92.7515	93.0599	90.8856	90.7251	89.1216	89.6865

Sample DV2000B

Point	#1	#2	#3	#4	#5	#6	#7	#8
SiO2	55.731	51.247	43.267	98.989	63.776	67.972	63.796	65.518
TiO2	0.322	0.053	2.474	0	0	0	0	0
Al2O3	8.485	30.544	9.98	0	18.77	13.232	18.796	17.101
Cr2O3	0.203	0	0.244	0	0	0	0	0
FeO	4.468	0.381	11.164	0	0.103	0.009	0.075	0.151
MnO	0.079	0.028	0.155	0	0.013	0	0.044	0.021
MgO	11.426	0.03	14.009	0	0	0.356	0	0
CaO	14.123	13.516	11.277	0	0	2.377	0.154	0.266
Na2O	5.021	3.68	1.944	0	0.356	1.952	2.959	1.298
K2O	0.147	0.142	0.881	0.008	15.811	1.395	11.86	12.934
P2O5	0	0	0	0	0	0	0	0
F	0	0	0.09	0	0.05	0	0.012	0.006
Cl	0	0.004	0.037	0	0.003	0	0	0.015
SO2	0.048	0.028	0.068	0.002	0.064	0.01	0.006	0.02
Total	100.056	99.657	95.594	99.004	98.948	87.306	97.706	97.333
Mineral	Standard	Standard	Amphibole	Quartz	K-Spar	Zeolite	K-Spar	K-Spar

Point	#9	#10	#11	#12	#13	#14	#15	#16
SiO2	64.251	62.091	92.46	64.273	67.417	70.256	67.501	42.281
TiO2	0	0	0	0.005	0.032	0	0	1.261
Al2O3	17.181	12.23	1.784	19.064	16.293	12.187	12.034	13.368
Cr2O3	0	0	0	0	0	0	0	0.038
FeO	0.214	0.495	0.044	0.107	0.978	0.477	0.419	21.398
MnO	0.018	0.015	0	0.031	0.003	0.041	0	0.404
MgO	0	0.196	0	0	0.096	0.441	0.3	3.306
CaO	0.197	0.526	0.628	0.192	0.812	2.213	2.443	0.19
Na2O	1.248	0.231	0.201	2.932	4.776	1.202	0.774	0.123
K2O	12.901	9.267	0.329	12.076	4.377	3.152	2.208	7.389
P2O5	0	0	0	0	0	0	0	0
F	0	0.025	0	0	0	0	0	0.051
Cl	0.01	0.047	0.002	0.007	0.005	0.002	0.017	0.055
SO2	0.006	0.082	0.06	0.034	0.004	0.04	0	0.054
Total	96.03	85.209	95.511	98.723	94.796	90.017	85.699	89.921
Mineral	K-Spar	K-Spar	Quartz	K-Spar	K-Spar/Glass	Matrix/Glass	Matrix/Glass	Biotite

Point	#17	#18	#19	#20	#21	#22	#23	#24
SiO2	53.189	42.105	0	64.562	68.13	69.112	39.301	29.458
TiO2	0	0	26.119	0	0	0	3.371	0.874
Al2O3	8.597	8.429	0.249	11.527	13.774	11.057	13.349	13.7
Cr2O3	0	0	0.183	0	0	0	0.001	0.317
FeO	0.937	0.05	68.2	0	0.071	0.024	15.857	14.239
MnO	0.021	0	0.585	0	0	0	0.387	0.807
MgO	0.541	0.099	0.259	0.153	0.327	0	9.564	1.094
CaO	0.067	1.443	0.042	2.278	2.685	2.278	0.204	11.098
Na2O	0.046	0.825	0	2.023	1.082	3.37	0.199	0.009
K2O	6.058	2.709	0.047	1.77	2.05	0.838	7.582	0.036
P2O5	0	0	0	0	0	0	0	0
F	0.006	0	0.049	0	0	0	0.208	0.105
Cl	0.146	0.169	0.03	0.034	0	0.011	0.057	0.041
SO2	0.036	0.046	0.078	0.054	0.042	0.042	0.052	0.07
Total	69.646	55.878	95.842	82.403	88.164	86.735	90.137	71.851
Mineral	Bad Surface	Bad	Magnetite	Glass?	Matrix/Glass	Matrix/Glass	Biotite	Bad

Point	#25	#26	#27	#28	#29	#30	#31	#32
SiO2	43.051	44.367	0.706	66.675	50.898	63.717	63.19	64.089
TiO2	2.267	1.256	4.078	0	0.045	0.037	0.028	0.033
Al2O3	11.628	14.084	1.321	0.461	30.718	19.051	18.96	18.756
Cr2O3	0	0.034	0.171	0.001	0	0	0	0
FeO	10.947	18.739	79.858	1.234	0.336	0.076	0.098	0.05
MnO	0.236	0.426	1.406	0.057	0.023	0.026	0	0
MgO	6.19	3.003	0.139	11.532	0.081	0	0	0
CaO	0.445	0.179	0.059	18.083	13.99	0.214	0.214	0.154
Na2O	0.577	0.199	0	0.005	3.592	2.932	2.855	2.872
K2O	7.15	7.252	0.054	0.06	0.096	11.589	11.9	12.339
P2O5	0	0	0	0	0	0	0	0
F	0.072	0.255	0.079	0.013	0.025	0	0	0
Cl	0.061	0.082	0.059	0.021	0.005	0.004	0	0.004
SO2	0.088	0.078	0.17	0.058	0.042	0.036	0.048	0.022
Total	82.715	89.955	88.101	98.205	99.931	98.139	97.787	98.637
Mineral	Altered Biotite	Altered Biotite	Magnetite	Not Good Mix	Standard	K-Spar	K-Spar	K-Spar

Point	#33	#34	#35	#36	#37	#38	#39	#40
SiO2	64.457	54.18	64.044	64.206	61.954	43.59	66.735	63.928
TiO2	0.027	0.022	0.033	0.033	0	1.376	0	0.023
Al2O3	19.019	0.049	19.019	18.764	23.089	13.32	16.757	19.117
Cr2O3	0.001	0.003	0	0	0	0.004	0	0
FeO	0.091	1.705	0.068	0.069	0.163	19.265	0	0.089
MnO	0.01	0.13	0.003	0.005	0	0.383	0.01	0.026
MgO	0	16.572	0	0	0	2.839	0	0
CaO	0.164	26.274	0.236	0.147	4.621	0.2	0	0.183
Na2O	2.953	0.047	2.986	2.859	7.972	0.213	0.024	2.929
K2O	12.357	0.001	12	12.077	1.235	7.588	15.458	12.32
P2O5	0	0	0	0	0	0	0	0
F	0	0	0	0	0	0	0.019	0
Cl	0.004	0.01	0	0.002	0.002	0.065	0.002	0.006
SO2	0.066	0.038	0.04	0.01	0.054	0.122	0.004	0.04
Total	99.529	99.176	98.902	98.47	99.093	89.271	99.077	98.952
Mineral	K-Spar	CPX?	K-Spar	K-Spar		Amphibole	K-Spar	K-Spar

Point	#41	#42
SiO2	63.408	64.711
TiO2	0.005	0.03
Al2O3	23.693	19.028
Cr2O3	0	0
FeO	0.076	0.072
MnO	0	0
MgO	0	0
CaO	4.316	0.169
Na2O	8.328	3.003
K2O	1.112	12.363
P2O5	0	0
F	0	0
Cl	0	0.005
SO2	0.04	0.064
Total	101.003	99.854
Mineral		K-Spar

Sample DV2000A

Point	#1	#2	#3	#4	#5	#6	#7	#8
Si	49.595	65.944	30.739	69.95	34.898	0	54.911	7.509
Ti	0.866	0	0.153	0	4.203	3.826	0.003	3.665
Al	8.508	17.101	0.053	11.095	14.377	1.255	28.007	1.385
Cr	0.167	0	0.216	0	0.056	0.189	0	0.17
Fe	6.552	0.023	0.14	0.037	18.932	81.366	0.45	74.064
Mn	0.167	0	0.148	0.013	0.55	1.382	0.003	1.101
Mg	16.201	0	0	0	10.66	0.293	0	0.265
Ca	16.422	0	0.008	3.699	0.066	0.045	10.024	0.196
Na	1.259	0.098	0.043	1.33	0.33	0	5.393	0.084
K	0	15.867	0.053	0.806	8.62	0.075	0.395	0.113
P	0	0	0.037	0	0	0	0	0
S	0.014	0.02	0.122	0.004	0.128	0.11	0.006	0.116
Zr	0	0	68.19	0	0.113	0.44	0	0.365
Total	99.75	99.053	99.904	86.935	92.933	88.98	99.192	89.032
Mineral		K-spar	Zircon	Zeolite		Magnetite		

Point	#9	#10	#11	#12	#13	#14	#15	#16
Si	40.283	63.445	71.311	66.833	46.93	0	36.558	34.462
Ti	4.337	0	0	0	1.711	0.152	3.439	4.042
Al	12.138	18.747	11.41	17.063	6.407	0.034	12.355	14.088
Cr	0.016	0	0	0	0.595	0.227	0.004	0.057
Fe	12.874	0.015	0.013	0.224	6.398	89.011	16.019	19.677
Mn	0.201	0.018	0	0	0.092	0.346	0.323	0.421
Mg	6.669	0	0	0	13.973	0	9.473	10.472
Ca	0.395	0	3.818	2.195	22.8	0.067	0.255	0.122
Na	0.178	0.359	1.624	4.21	0.309	0	0.782	0.496
K	7.064	16.45	0.737	5.554	0.014	0.052	6.703	8.858
P	0	0	0	0	0	0	0	0
S	0.15	0.024	0	0.018	0.046	0.082	0.112	0.162
Zr	0.023	0	0	0	0.101	0.455	0.032	0.072
Total	84.326	99.057	88.914	96.098	99.375	90.426	86.056	92.928
Mineral	Biotite	K-spar		K-Spar	CPX	Magnetite	Biotite	Biotite

Point	#17	#18	#19	#20	#21	#22	#23	#24
Si	57.587	63.346	64.185	39.677	61.86	63.614	62.899	68.69
Ti	0.017	0.02	0	3.446	0	0.038	0	0.015
Al	26.078	19.289	18.879	12.553	23.176	18.7	10.894	12.746
Cr	0	0	0	0.018	0	0	0	0
Fe	0.34	0.098	0.114	16.175	0.148	0.01	0.426	0.044
Mn	0	0	0	0.31	0	0.008	0.035	0
Mg	0	0	0	9.683	0	0.002	0.41	0.274
Ca	7.674	0.15	0.165	0.339	4.283	0.01	3.484	3.818
Na	6.277	2.89	3.328	0.288	8.101	1.36	2.658	0.681
K	0.914	12.06	11.617	7.412	1.131	15.256	0.907	0.713
P	0	0	0	0	0	0.037	0.057	0.032
S	0	0.022	0.048	0.064	0.028	0.02	0.03	0.018
Zr	0	0.02	0	0.069	0	0.074	0	0
Total	98.888	97.896	98.337	90.034	98.726	99.131	81.804	87.035
Mineral		Feldspar	Feldspar	Biotite		Feldspar		

Point	#25	#26	#27	#28	#29	#30	#31	#32
Si	0.165	32.363	35.401	67.995	38.556	8.75	0	60.356
Ti	0.072	1.905	3.903	0.002	4.16	3.478	3.765	0.04
Al	0	11.739	13.702	8.886	13.453	1.109	1.158	23.266
Cr	0.096	0	0.054	0	0	0.189	0.235	0
Fe	0.181	9.337	18.262	0.066	10.858	72.407	82.542	0.206
Mn	0.241	0.208	0.431	0.018	0.169	1.021	1.304	0.018
Mg	0.048	6.251	11.611	0.012	13.419	0.448	0.521	0
Ca	52.436	1.325	0.221	0.122	0.213	0.227	0.07	4.321
Na	0.113	0.545	0.43	0.252	0.555	0.058	0.005	8.076
K	0	5.955	8.693	8.449	7.536	0.043	0.02	1.053
P	37.917	0.158	0.03	0	0.011	0.099	0.044	0
S	0.268	0.076	0.182	0.054	0.084	0.098	0.084	0.006
Zr	1.383	0	0.181	0	0.101	0.404	0.488	0.007
Total	92.922	69.864	93.106	85.858	89.12	88.331	90.237	97.352
Mineral	Apatite		Biotite		Biotite		Magnetite	Plag

Point	#33	#34	#35	#36	#37	#38	#39	#40
Si	29.61	2.435	56.471	8.341	63.804	15.963	0	34.158
Ti	0.195	3.454	0.038	3.071	0.042	1.326	3.706	3.313
Al	0	1.037	26.395	1.444	19.497	5.092	1.09	12.021
Cr	0.228	0.189	0	0.193	0	0.191	0.189	0.05
Fe	1.052	80.153	0.404	67.813	0.286	4.249	80.233	14.636
Mn	0.22	1.245	0.037	1.3	0.013	0.229	1.366	0.398
Mg	0.033	0.531	0.035	0.579	0	2.32	0.481	9.348
Ca	0.229	0.133	8.164	0.509	1.23	1.131	0.069	0.271
Na	0.075	0.075	6.207	0.104	5.26	0.344	0.023	0.384
K	0	0.007	0.605	0.077	7.583	2.166	0.002	7.103
P	0.229	0.094	0.021	0.121	0.041	0.092	0.089	0.076
S	0.098	0.08	0	0.15	0.026	16.237	0.098	2.717
Zr	64.818	0.49	0	0.381	0.049	0.525	0.497	0.24
Total	96.791	89.923	98.381	84.084	97.832	49.868	87.844	84.72
Mineral	Zircon				Feldspar		Magnetite	

Point	#41	#42	#43	#44	#45	#46	#47	#48
Si	36.663	0	55.429	30.515	61.496	54.689	42.033	63.787
Ti	3.901	24.61	0.34	0.866	0	0.003	1.725	0
Al	12.835	0.106	8.512	14.275	23.448	0.176	11.412	18.548
Cr	0.038	0.19	0.199	0.383	0	0.035	0.091	0.009
Fe	17.994	65.546	4.447	15.039	0.21	1.494	14.962	0.14
Mn	0.467	0.669	0.094	1.16	0	0.133	0.307	0.022
Mg	10.401	0.353	11.615	1.025	0	17.881	12.064	0
Ca	0.19	0.077	13.891	12.08	4.553	25.687	11.172	0.137
Na	0.226	0	4.978	0.042	8.093	0.075	2.044	2.839
K	7.99	0.008	0.119	0.051	1.008	0.039	1.196	11.974
P	0.053	0.11	0	0.011	0	0	0	0
S	0.078	0.072	0.006	0.052	0	0	0.014	0
Zr	0.127	0.497	0.058	0.427	0	0.036	0.157	0
Total	90.969	92.239	99.694	75.926	98.811	100.253	97.18	97.461
Mineral	Biotite	Ti-Magneite	CPX				CPX	Feldspar

Point	#49	#50	#51	#52	#53	#54	#55	#56
Si	63.443	37.694	74.911	40.131	35.927	4.522	30.474	29.049
Ti	0.04	3.94	0	2.61	5.324	3.763	0.112	16.895
Al	18.73	13.394	11.747	12.06	17.543	1.162	0	3.008
Cr	0.031	0.001	0	0	0.025	0.152	0.194	0
Fe	0.175	17.378	0	13.087	13.071	75.843	0.773	20.043
Mn	0	11.61	0	7.77	0.035	0.371	0	1.64
Mg	0	0.435	0	0.214	0.132	0.998	0.124	0.692
Ca	0.14	0.199	3.705	0.316	23.152	0.155	0.041	0.362
Na	2.751	0.321	1.173	0.4	0.004	0.082	0.053	0.266
K	12.258	7.901	0.825	6.372	0	0.059	0.011	1.358
P	0	0.057	0.005	0.046	0.023	0.041	0.431	0.069
S	0	0.072	0	0.034	0.032	0.098	0.066	0.062
Zr	0.066	0.031	0	0	0.099	0.323	64.721	0
Total	97.637	93.037	92.369	83.045	95.369	87.573	97.003	73.446
Mineral	Feldspar	Biotite					Zircon	Low Total

Point	#57	#58	#59	#60	#61	#62	#63	#64
Si	2.997	69.777	21.369	24.133	69.769	4.698	5.201	71.705
Ti	7.001	0	0.349	0.691	0	3.713	3.358	0
Al	3.167	14.938	1.64	6.33	12.661	0.973	1.134	11.097
Cr	0.167	0	0.14	0.114	0	0.161	0.123	0
Fe	64.599	0.176	0.306	2.159	0	78.084	71.683	0
Mn	1.94	0	0.169	2.122	0.224	0.337	0.244	0
Mg	1.631	0	0.066	0.127	0	1.046	1.252	0
Ca	0.185	0.67	0.919	0.698	4.358	0.197	0.172	2.877
Na	0.117	3.859	0.132	0.256	0.701	0.07	0.061	0.887
K	0.027	6.825	0.23	1.177	0.581	0.063	0.128	0.578
P	0.048	0	0.133	0.108	0	0.066	0.053	0
S	0.036	0	17.316	13.784	0	0.066	0.12	0
Zr	0.263	0	0.294	0.23	0	0.131	0.226	0
Total	82.179	96.249	43.067	51.931	88.298	89.606	83.754	87.147
Mineral		Feldspar		Low Total				

APPENDIX C: INAA Normalization Factors

SpiderDiagram (Mantle Normalizing Diagram) Values:
(Sun and McDonough, 1989)

Cs-	0.0079	Rb-	0.635
Ba-	0.635	Th-	0.085
U-	0.021	Ta-	0.041
Nb-	0.713	K-	250
La-	0.687	Ce-	1.775
Pb-	0.071	Sr-	21.1
P-	95	Nd-	1.354
Sm-	0.444	Zr-	11.2
Hf-	0.309	Eu-	0.168
Ti-	1300	Tb-	0.108
Y-	4.55	Yb-	0.493
Lu-	0.074		

REE Normalizing Values:
(Nakamura, 1974)

La-	0.329	Ce-	.865
Pr-	.112	Nd-	.630
Pm-	-----	Sm-	.203
Eu-	.077	Gd-	.276
Tb-	.047	Dy-	.343
Ho-	.070	Er-	.225
Tm-	.030	Yb-	.220
Lu-	.0339		

APPENDIX D: ICPMS Analyses for Ibex Pass Units

Sample ID	DV 73	DV 67	DV 27	DV 65	DV 48	DV 34	DV 68	DV 90	DV 56
La ppm	58.10	50.68	87.37	45.97	86.14	64.37	50.22	78.38	93.12
Ce ppm	111.98	68.10	156.72	90.19	159.62	116.51	75.58	148.89	169.46
Pr ppm	13.01	5.43	17.22	10.69	18.37	12.91	6.93	16.93	18.15
Nd ppm	46.89	14.27	58.28	39.52	63.80	44.26	20.28	58.64	59.03
Sm ppm	7.87	1.83	8.62	6.96	9.88	6.96	2.90	9.47	8.52
Eu ppm	1.91	0.29	2.10	1.68	2.36	1.59	0.52	2.12	1.69
Gd ppm	5.42	1.32	5.67	5.30	6.57	4.74	2.11	6.73	5.31
Tb ppm	0.70	0.19	0.73	0.72	0.86	0.62	0.30	0.96	0.73
Dy ppm	3.62	1.11	3.74	3.88	4.38	3.14	1.71	5.15	3.90
Ho ppm	0.65	0.24	0.68	0.73	0.80	0.57	0.35	1.00	0.75
Er ppm	1.62	0.78	1.72	1.86	2.06	1.45	1.04	2.59	2.02
Tm ppm	0.23	0.14	0.25	0.26	0.29	0.21	0.17	0.37	0.30
Yb ppm	1.33	1.12	1.62	1.55	1.84	1.30	1.29	2.30	1.97
Lu ppm	0.21	0.20	0.26	0.25	0.30	0.21	0.22	0.36	0.31
Ba ppm	1679	235	1940	1348	1640	1558	510	1475	1540
Th ppm	11.95	37.37	17.01	10.04	16.31	17.41	30.81	19.95	20.01
Nb ppm	12.56	24.86	22.78	15.00	25.84	15.96	22.95	27.62	26.96
Y ppm	16.86	7.52	18.64	18.83	21.46	15.52	10.59	26.34	20.06
Hf ppm	5.71	3.81	8.11	6.08	8.04	5.17	3.89	9.23	9.50
Ta ppm	0.72	1.63	1.35	0.89	1.30	0.99	1.50	1.74	1.64
U ppm	2.74	6.80	4.66	2.49	4.59	4.23	8.44	3.94	5.73
Pb ppm	22.82	32.22	27.90	18.43	21.88	22.72	31.18	27.69	29.86
Rb ppm	101.4	222.5	154.3	80.0	77.2	99.2	187.4	109.6	150.4
Cs ppm	1.71	2.61	3.13	2.34	1.08	1.27	5.02	1.39	2.02
Sr ppm	1224	115	1224	1097	1149	871	240	1563	282
Sc ppm	8.5	1.5	4.0	11.9	6.5	6.2	2.3	6.1	2.8
Zr ppm	228	102	355	250	359	204	119	385	402

APPENDIX E: XRF analyses for units in Ibex Pass

Sample	DV73	DV67	DV27	DV65	DV48	DV34	DV68	DV90	DV56
	Unnormalized Major Elements (Weight %):								
SiO2	57.45	72.14	59.13	57.47	60.61	60.78	71.17	63.74	67.33
TiO2	0.742	0.154	0.672	0.946	0.769	0.558	0.234	0.590	0.300
Al2O3	16.14	12.89	17.89	16.72	16.42	15.50	12.61	15.58	15.60
FeO*	4.24	0.92	4.02	5.41	5.11	3.86	1.18	2.72	2.01
MnO	0.079	0.018	0.065	0.084	0.062	0.068	0.054	0.057	0.052
MgO	3.16	0.60	1.25	2.87	0.74	1.50	0.52	0.66	0.60
CaO	5.91	0.75	4.08	6.13	4.32	4.06	1.05	2.24	1.33
Na2O	3.53	2.89	4.18	3.73	4.16	2.46	4.30	4.12	4.25
K2O	2.83	5.48	3.71	2.97	3.61	4.01	3.60	5.04	5.87
P2O5	0.508	0.029	0.433	0.407	0.652	0.336	0.078	0.214	0.151
Sum	94.59	95.87	95.42	96.74	96.46	93.13	94.78	94.95	97.50
SO3 >/=	0.15	0.25	0.00	0.00	0.01	0.00	0.00	0.00	0.06
	Normalized Major Elements (Weight %):								
SiO2	60.73	75.25	61.97	59.41	62.84	65.26	75.08	67.12	69.06
TiO2	0.784	0.161	0.704	0.978	0.797	0.600	0.247	0.621	0.308
Al2O3	17.06	13.44	18.74	17.28	17.02	16.64	13.31	16.41	16.00
FeO*	4.48	0.96	4.21	5.59	5.30	4.14	1.24	2.86	2.06
MnO	0.083	0.019	0.068	0.087	0.064	0.073	0.057	0.060	0.053
MgO	3.34	0.62	1.31	2.96	0.77	1.61	0.55	0.70	0.61
CaO	6.25	0.79	4.28	6.34	4.48	4.36	1.10	2.36	1.37
Na2O	3.73	3.01	4.38	3.85	4.31	2.64	4.53	4.33	4.36
K2O	2.99	5.72	3.88	3.07	3.75	4.31	3.80	5.30	6.02
P2O5	0.537	0.030	0.454	0.421	0.676	0.361	0.083	0.226	0.155
Total	100.00	100.00	100.00	100.00	100.00	100.00	100.00	100.00	100.00

Sample	DV73	DV67	DV27	DV65	DV48	DV34	DV68	DV90	DV56
Unnormalized Trace Elements (ppm):									
Ni	27	0	0	43	5	17	0	0	0
Cr	42	2	3	49	8	32	8	2	1
Sc	10	2	4	12	6	6	2	7	2
V	90	12	56	118	88	62	17	25	13
Ba	1682	238	1954	1348	1637	1575	505	1487	1550
Rb	102	224	155	80	77	100	185	111	151
Sr	1225	116	1224	1081	1137	871	243	1572	284
Zr	233	102	363	253	362	240	118	390	408
Y	16	8	18	18	20	14	11	26	20
Nb	12.1	24	22.5	14.4	25.3	15.8	22	27.2	26.4
Ga	19	16	20	18	19	17	14	20	17
Cu	24	0	8	41	23	15	2	0	0
Zn	67	31	75	74	63	58	28	65	68
Pb	19	27	25	16	19	21	29	26	26
La	59	49	86	44	84	61	49	74	90
Ce	107	68	158	91	154	115	74	146	171
Th	9	35	14	7	13	14	28	17	17
Nd	46	14	58	39	63	43	21	59	58
U	4	7	5	2	5	4	9	5	6
sum tr.	3794	975	4247	3347	3807	3281	1366	4057	2907
in %	0.38	0.1	0.42	0.33	0.38	0.33	0.14	0.41	0.29
sum m+tr	61.11	75.35	62.39	59.74	63.22	65.59	75.22	67.53	69.35
M+Toxides	61.18	75.36	62.47	59.8	63.29	65.64	75.24	67.6	69.4

Normalized Trace Elements (ppm):									
Cr2O3	61.1	3.5	4.8	71.8	11.1	46.3	11.8	2.5	1.8
Sc2O3	14.9	3.2	5.7	18.3	9	9.5	3.7	10	3.5
V2O3	131.8	17.8	83	172.9	129.9	91.5	25	37.1	19.1
BaO	1877.7	265.8	2182	1504.6	1827.9	1758.5	563.9	1660.1	1730.1
Rb2O	112	244.4	169.6	87.5	84.2	109.1	202.6	121.2	165.4
SrO	1448.8	137.7	1447.9	1277.9	1344.7	1029.5	287.7	1859.1	335.3
ZrO2	315	138.2	489.8	341.6	488.4	324.6	159.7	526.3	551.1
Y2O3	20.6	10.4	22.5	23.1	25	18.3	14.4	32.8	25
Nb2O5	17.3	34.3	32.2	20.6	36.2	22.6	31.5	38.9	37.8
Ga2O3	25	20.8	26.6	24.7	25.4	22.9	19.2	26.6	22.2
CuO	30.4	0	9.4	51.2	28.5	18.9	2.1	0	0.4
ZnO	83.8	38.7	94.2	92.2	79.3	72.6	34.6	80.9	85.2
PbO	20	29.5	26.8	16.7	20.9	22.2	31.3	27.7	28.4
La2O3	69.7	57.2	100.5	52	98.5	71.4	57.3	87.3	105.3
CeO2	132	83.7	194	112.1	189.7	140.7	90.7	179.1	209.6
ThO2	9.8	38.1	15	7.9	14.3	15.7	31.1	19	19.1
Nd2O3	54.1	16.2	67.2	45	72.9	50.4	24.3	68.9	67.9
U2O3	4.6	7.8	5.7	2.6	5.1	4.3	9.8	5.1	6.1
Bi2O5	0	0	0	0	0	0	0	0	0
Cs2O	0	0	0	0	0	0	0	0	0
As2O5	0	0	0	0	0	0	0	0	0
W2O3	0	0	0	0	0	0	0	0	0
sum tr.	4463	1147.47	4976.8	3977.62	4497.43	3850.94	1600.84	4782.37	3413.16
in %	0.45	0.11	0.5	0.4	0.45	0.39	0.16	0.48	0.34
W2O3	0	0	0	0	0	0	0	0	0
sum tr.	4463	1147.47	4976.8	3977.62	4497.43	3850.94	1600.84	4782.37	3413.16
in %	0.45	0.11	0.5	0.4	0.45	0.39	0.16	0.48	0.34

CURRICULUM VITA

Sabrina Michelle Canalda was born on January 28, 1979 in Washington D.C. to parents John Canalda and Susan Sabourin. She went to Hanks High School in El Paso for two years and then graduated from Aldine High School in Houston, Texas in 1997. She received her associate's degree at El Paso Community College in December of 2004. In May of 2006 she completed her BS degree in Geology. She completed her undergraduate research under the advisory of Dr. Tom Gill. She started the Master Program in August 2006 under the advisory of Dr. Terry Pavlis. As a graduate student she received the AGI scholarship and participated in several organizations. She presented her research work in several symposia. She also has received several awards for oral presentations at the department's annual colloquium. Throughout her undergraduate and graduate studies she worked full time and raised her son Noah Chavira. On completion of her studies she hopes to further her education and obtain a job with the United States Geological Survey.